Characterizing Trojan Asteroids Throughout the Solar System

by

Larissa Markwardt

A dissertation submitted in partial fulfillment
of the requirements for the degree of
Doctor of Philosophy
(Astronomy and Astrophysics)
in The University of Michigan
2023

Doctoral Committee:

Associate Professor Emily Rauscher, Chair
Professor Fred Adams
Professor Gary Bernstein, University of Pennsylvania
Professor David Gerdes
Dr. Hsing-Wen Lin
Professor Renu Malhotra, University of Arizona
Professor John Monnier

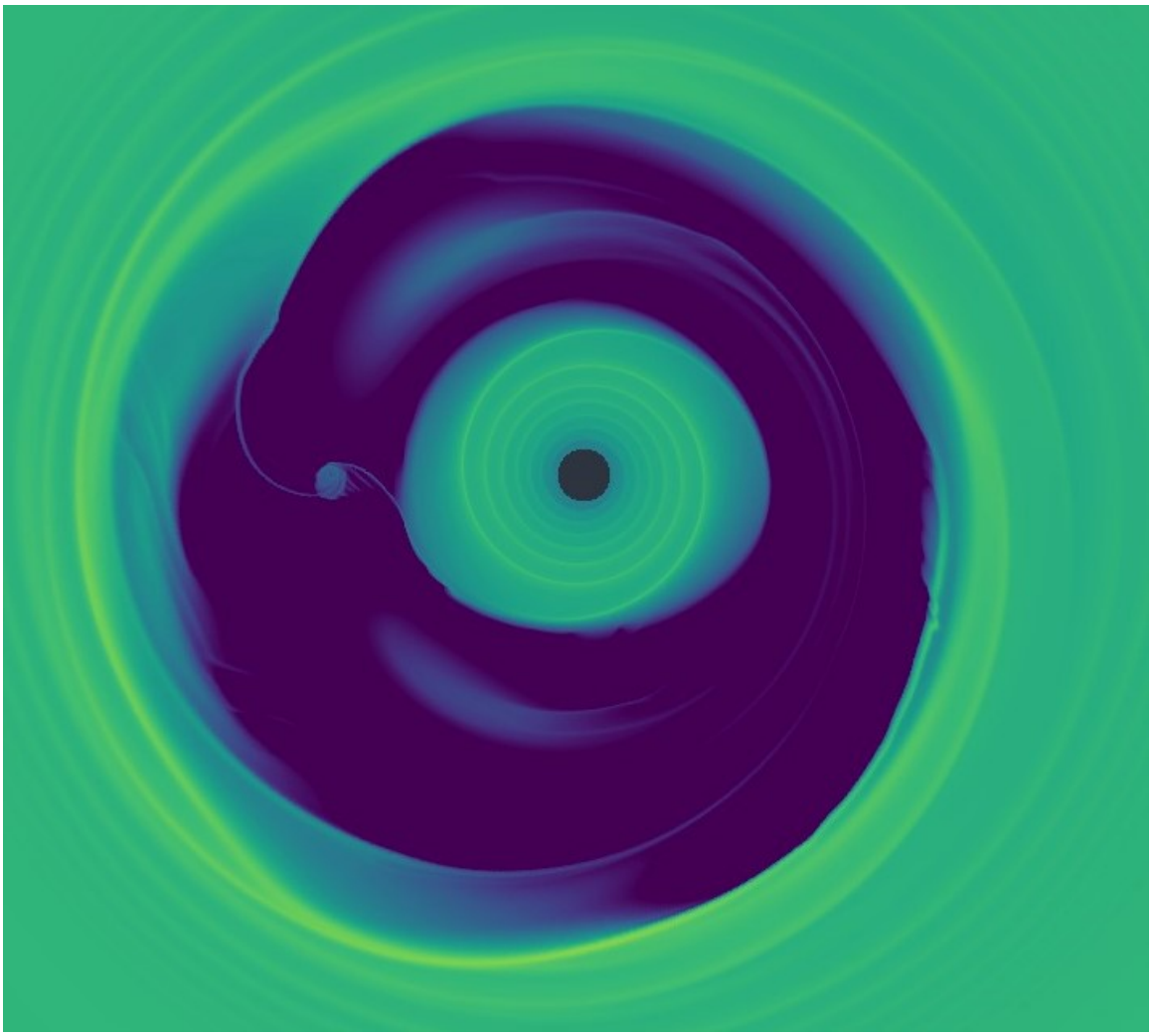

Trojans exist at all scales

Larissa Markwardt

lmmarkwa@umich.edu

ORCID iD: 0000-0002-2486-1118

© Larissa Markwardt 2023

This one's for me

ACKNOWLEDGEMENTS

I have so many people to thank that made completing this thesis possible. First I would like to thank my thesis committee, Emily Rauscher, Ed Lin, David Gerdes, Fred Adams, John Monnier, Gary Bernstien, and Renu Malhotra. All of you have contributed to my work and growth as a scientist and I appreciate the years of advice you all have given me.

I would also like to thank my family for all the love and support they have always given me. To my siblings, you always bring joy to my life and I'm proud to be your big sister. To my parents thank you for inspiring my love of science and encouraging me to follow my dreams. Kori, you are the love of my life and are always by my side cheering me on; there's no way I would be here without you.

Finally, the most vital support I have received in grad school came from all of fellow students that befriended me. Kevin and Nic, I couldn't have asked for a better pair of friends in my cohort and I hope we can continue playing board games together forever. Kamber, Aleksandra, Erin, Adi, and Renee, I'm so grateful that you all reached out and took me under your wings. You all are my inspiration, my guides, and my dear friends. I couldn't imagine going through grad school without you all behind me.

TABLE OF CONTENTS

DEDICATION ii

ACKNOWLEDGEMENTS iii

LIST OF FIGURES vii

LIST OF TABLES xiv

LIST OF APPENDICES xvi

ABSTRACT xvii

CHAPTER

I. Introduction 1

1.1 Observing Physical Properties of Small Bodies in the Solar System 1
1.1.1 Discovery 4
1.1.2 Orbital Characterization 6
1.1.3 Size Distribution 7
1.1.4 3-dimensional Shape 8
1.1.5 Surface Composition 9
1.1.6 Interior Structure 11
1.2 Trojans: 1 to 1 resonators 11
1.2.1 Jupiter Trojans 13
1.2.2 Mars Trojans 15
1.2.3 Neptune Trojans 16
1.2.4 Temporarily Captured Objects 18
1.2.5 Earth Trojans? 19
1.2.6 Other resonant populations 20
1.3 Structure of Thesis 22

II. Search for L5 Earth Trojans with DECam 24

2.1 Preface . . . 24
2.2 Introduction . . . 24
2.2.1 Significance of Earth Trojans . . . 25
2.2.2 An Unstable Earth Trojan: 2010 TK_7 . . . 26
2.2.3 Previous ET Searches . . . 27
2.3 DECam Survey . . . 28
2.4 Reduction Pipeline . . . 30
2.4.1 Source Extractor . . . 30
2.4.2 Bullseye . . . 30
2.4.3 Verification by Eye/Catalog Creation . . . 37
2.5 Detected Objects . . . 38
2.5.1 Previously Known Objects . . . 38
2.5.2 New Objects . . . 40
2.5.3 Aten & Apollo Asteroids . . . 42
2.6 Upper Limits on ET Population . . . 43
2.6.1 Synthetic ETs . . . 43
2.6.2 Injection of Synthetic ETs . . . 46
2.6.3 Upper Limit on ET Population . . . 51
2.7 Discussion . . . 57
2.7.1 Summary . . . 57
2.7.2 Comparison to Previous Surveys . . . 57
2.7.3 Missing Primordial ETs? . . . 60

III. Photometric Survey of Neptune's Trojan Asteroids I: The Color Distribution . . . 63

3.1 Preface . . . 63
3.2 Introduction . . . 63
3.3 Survey Design . . . 66
3.4 Photometric Reduction . . . 67
3.4.1 Calibration . . . 67
3.4.2 PSF Modeling . . . 68
3.4.3 Rotation Curve Correction . . . 70
3.4.4 Reddening Line . . . 70
3.5 Results . . . 72
3.5.1 Color-Color Plots . . . 72
3.5.2 Comparison to Other Populations . . . 80
3.5.3 Unique Targets . . . 83
3.6 Discussion . . . 84
3.6.1 Why were the ultra-red NTs rare before this work? . . . 84
3.6.2 Possible explanation of the NT's color-orbit-size correlation . . . 85
3.7 Conclusions . . . 87

IV. The First Near-IR Spectroscopy Survey of Neptune Trojans with JWST 89

4.1 Introduction 89
4.2 Survey Design 92
4.3 Data Analysis 93
4.4 Results 95
4.5 Discussion 96
4.6 Conclusions 100

V. Conclusions 101

5.1 Science Results 101
5.1.1 ET Size Distribution 101
5.1.2 NT Surface composition 102
5.2 Future Work 103
5.2.1 Earth Trojans 104
5.2.2 Neptune Trojans 104
5.2.3 Mars Trojans 105
5.2.4 Jupiter Trojans 106

APPENDICES 108
B.1 Calculating Upper Limits Under Different Assumptions of the ET Population 112

BIBLIOGRAPHY 115

LIST OF FIGURES

Figure

1.1 Distribution of small bodies in the inner Solar System based on distance from the Sun (in AU). Different sub-populations are colored and labeled in the plot. The Hilda and Trojan asteroids are clusters around 4 and 5.1 AU respectively and are in resonance with Jupiter. The Kirkwood gaps are also driven by Jupiter's resonances. 3

1.2 Various asteroid classification schemes based on optical reflectance spectra (*Tholen*, 1984; *Bus*, 1999; *DeMeo et al.*, 2009). The Bus-DeMeo scheme is the most contemporaneous with this work. Targets are classified by comparing spectral features such as slope and band position and shape (band centers, band depths, band widths, band area ratios) to these example spectra. 10

1.3 Semi-major axis (a) of outer Solar System objects vs inclination (i). Objects are color-coded based on their dynamical class. Resonant objects are shown as red circles and generally lie along lines of constant semi-major axis. The size of each circle corresponds to the diameter of the object. Pluto is by far the largest resonant TNO. 21

2.1 The area covered by our survey. The star marks the location of the L5 point. The relative density of synthetic ET objects (see Sec. 2.6.1) is shown in the background in blue. Each rectangle corresponds to a chip in one of the 8 DECam fields. In total, these fields cover ~ 24 sq. deg. near L5. 29

2.2 *Left*: The rate of motion on the sky for the "Strict" set of synthetic ETs (see Sec. 2.6.1). Other than at small geocentric ranges ($\lesssim$ 0.1 AU), the ETs have a well constrained speed of 1 deg./day. *Right*: Same as *Top* but for the "Jupiter Trojan" set of synthetic ETs (synthetic ETs generated based on observations of Jupiter Trojans; see Sec. 2.6.1). These objects also have a well constrained speed of $\sim$1 deg./day for geocentric ranges >0.5 AU. There is more dispersion in the speed, but this is expected as this set of ETs was generated based off of observations of Jupiter Trojans. 35

2.3 This figure shows the predicted rates of motion for 2010 TK_7 on each night in 2018 (taken from JPL HORIZONS: ssd.jpl.nasa.gov/?horizons). The dashed line shows the mean speed and the grey region depicts the standard deviation. The green region represents the speeds for which an object would be flagged as an ET by our pipeline. Nights on which we consider 2010 TK_7 to be observable are plotted in blue. The other colors represent nights on which observing 2010 TK_7 would be unfavorable according to the Solar Presence and Lunar Presence parameters from JPL HORIZONS. In particular, "C" is civil twilight/dawn, "N" is nautical twilight/dawn, "A" is astronomical twilight/dawn, and "m" is refracted upper-limb of Moon on or above apparent horizon. Although the standard deviation region extends beyond our assumptions for ET speed, the mean is well with our search space. In fact, most of the nights beyond our speed cuts are ones for which 2010 TK_7 is not observable. 36

2.4 *Left*: Recovery rates for previously known minor bodies as a function of predicted V band magnitude. The known minor bodies that coincided with our survey area are shown in pink, and those which were detected and linked by our pipeline are shown in yellow. The recovery rate in each bin, with Poisson errors, are shown as a blue dotted line. *Right*: This plot shows our recovery rates for previously known minor bodies as a function of predicted total sky motion. Colors are the same as *Top*. The overall recovery rate of $\sim$40% is shown as a black dotted line. The recovery rates across all of these speeds are generally consistent with this overall rate, but recovery rates are lower for slower speeds. 39

2.5 This figure shows the orbit of the Aten asteroid detected in our survey, 2006 JF_{42}. At the time of our observations, this asteroid was near the L5 point. With a distance to the Earth of 0.78 AU and a distance to the Sun of 0.99 AU, this object had a rate of motion of 1.17 deg./day, causing it to be misidentified as an ET candidate by our pipeline. This figure was produced using REBOUND (*Rein and Liu*, 2011). 44

2.6 *Left*: This figure compares the number of counts measured by SE for Solar-type stars in Field 0 to the number of counts for a fake source of the same V-band magnitude. In general, the points lie well along the one-to-one line and the radii of the fake and real sources are nearly the same. Not surprisingly, there is more dispersion from this line at the faint end, but the points still have the same number of counts within an order of magnitude. There is also a clear overabundance of fake counts for the brightest objects, which is likely due to the saturation limit. *Right*: Same as *Top* but for known Solar System objects in Field 0. These points fall well along the one-to-one line and the radii of the real sources as compared to the fake ones are still nearly the same. Based on this plot, we conclude that our fake sources are consistent with our observations of known Solar System objects in our survey. 47

2.7 This figure compares our theoretical H distribution of ETs (Eq. 2.5) to the distribution generated by random draws from Eq. 2.5 normalized by the total number of fake ETs (in the case of this figure, 10^3). The black dashed and dot-dashed lines represent the theoretical H distribution with $\alpha = 0.46$ and 0.54, respectively. The blue and red histograms represent the cumulative and non-cumulative H distributions, respectively, which were generated for the simulated ETs (see Sec. 2.6.2 for description). Due to the random nature of this method, these distributions are similar to those used for the sources that were actually injected into our images to asses our recovery rate, but they are not exactly the same. Most importantly, the simulated cumulative distribution lies well between the two theoretical distributions. We therefore conclude that the injected ETs have an H (and thus size) distribution consistent with what we would expect theoretically. 49

2.8 This figure demonstrates coverage by our survey of the synthetic ET population. The Lagrange points and the Sun are plotted as half filled circles for reference. The yellow shaded area represents the L5 cloud (the area with ecliptic longitude within 30 degrees of L5). Synthetic ETs (see Sec. 2.6.1) that were injected into our images are plotted as purple squares, while those that were not are blue circles. These injected points essentially depict the area covered by our survey. These objects make up 24% of the ETs in the L5 cloud. 52

2.9 This figure compares the injected ETs (blue) from the set of Synthetic ETs to those that were detected, linked, and flagged as ET candidates by our pipeline (red); in other words, this plot shows our recovery rates as a function of H. We have nearly 100% recovery rates for most of the bins at the bright end, and the rates begin to fall off at ∼H=19.7. This value is essentially our limiting magnitude in H (though this does not directly relate to our limiting magnitude in V-band). Overall, we recovered ∼50% of the injected ETs. 54

2.10 Upper limits on the ET population calculated from our survey area coverage (Fig. 2.8) and recovery rate (Fig. 2.9). The yellow triangle depicts the upper limit calculated for L4 ETs by *Cambioni et al.* (2018), while the pink triangle is the upper limit extrapolated from the *Whiteley and Tholen* (1998) results by *Cambioni et al.* (2018). The upper limits from this work have two distinct regimes: flat at the bright end and steeply increasing at the faint end. We get a sharp increase for the faintest magnitudes due to our limiting magnitude and relatively poor recovery rates for faint ETs. For the faintest bin, H=20.4, we calculate an upper limit of 97 ETs. This limit is clearly more stringent than that from the *Whiteley and Tholen* (1998) results (194) and somewhat higher than the *Cambioni et al.* (2018) limit (73) for L4. Our recovery rates are flat at the bright end because all of these bins had nearly 100% recovery rates leading to a constant upper limit (∼15) for those magnitudes. The dotted line represents the faintest magnitude (H=19.7) still within the flat regime. At this magnitude, we calculate an upper limit of 18. 56

2.11 This figure depicts the stricter upper limits calculated for bright ETs assuming the ET H distribution follows a power law (Eq. 2.5). Slopes of 0.46-0.54 are consistent with the H distributions for main belt asteroids. A slope of 0.7 was used in *Cambioni et al.* (2018) for similar extrapolations to compare their results to *Whiteley and Tholen* (1998). The dotted line represents the point used for extrapolation, H=19.7 (see Fig. 2.10). The grey region depicts where N(<H) < 1, meaning the upper limit is essentially 0 ETs. Note, α=0.46 gives the most conservative upper limits of the three power laws at the bright end, while α=0.7 is most conservative at the faint end. 58

2.12 Extrapolated upper limits (lines) based on the measured upper limit (circular points) for each survey. The results for this work are in blue, *Cambioni et al.* (2018) in yellow, and the upper limit calculated by *Cambioni et al.* (2018) based on the results in *Whiteley and Tholen* (1998) are in pink. The dotted line represents the point used for extrapolation for the results in this work, H=19.7. The grey region depicts where N(H) <1, meaning the upper limit is essentially 0 ETs. The slope of the power law we use is α=0.46 for H<20.39 and α=0.7 for H>20.39, which gave the most conservative upper limits in Fig. 2.11. Under these assumptions, the results from this work give the most stringent upper limit on the ET population to date (18 ETs with H=19.7 as compared to 32 and 81). For steeper power laws, the upper limits for this work are essentially consistent with O-R18. . . 61

3.1 PSF modeling and subtraction. **top-left:** A star with the PSF model contour. **bottom-left:** The image of NT. **middle:** The model of the star (top) and the NT (bottom). **right:** the images after subtraction of the model. 71

3.2 This figure shows our least-squares approach to fitting r'-band lightcurves and colors for an example NT target, 2013 VX30. Each observation is shown as a colored point (downward triangle for g', square for r', diamond for i', and sideways triangle for z'. We then used a constant, but free parameter, color term to convert each observation to an r'-band observations; these point are shown as black circles. The solid line is our least-squares fit to the r'-band (black) points. The dotted lines show our 1σ deviation from this fit. 73

3.3 Measured $g-r$ vs $r-i$ of the NT population. Blue points are colors of scattered TNOs and orange triangles are JTs, both taken from the literature (*Hainaut et al.*, 2012). Light blue x's are previously observed colors of NTs (*Sheppard and Trujillo*, 2006; *Sheppard*, 2012; *Parker et al.*, 2013; *Jewitt*, 2018; *Lin et al.*, 2019). Targets observed in this paper are shown as green squares. Objects that have multiple observations in this paper are connected by a dot-dashed line. NTs that have been previously observed in the literature are connected by a dashed line. The yellow line marks values where the PCA yields values equal to our cutoff of 1.75 (see Fig. 3.7 and Sec. 3.5.2). Objects in the yellow region are above this cutoff and considered ultra-red in this paper. The blue line marks values where the PCA yields values equal to our cutoff of -1.25 (see Fig. 3.7 and Sec. 3.5.2). Objects in the blue region are blue this cutoff and considered blue in this paper. The top and right inset plots show the kernel density estimation (KDE) of the g-r and r-i distributions respectively of the included sub-populations. 75

3.4 Measured $g-r$ vs $r-z$ of the NT population. Navy upward triangles, green downward triangles, and blue circles are measurements taken from the literature of TNOs (scattered, cold, and hot respectively) (*Schwamb et al.*, 2019). Teal plus signs are colors of NTs taken from the literature (*Lin et al.*, 2019). Targets observed in this paper are shown as orange squares. Solar color and the reddening line (see 3.4.4) are depicted as an yellow star and orange dotted line respectively. Objects that have observations taken in this paper and from the literature are connected with a dashed line. Objects that have multiple observations in this paper are connected by a dot-dashed line. The green ellipse demarcates the region of color-color space occupied only by cold TNOs. The top and right inset plots show the kernel density estimation (KDE) of the g-r and r-z distributions respectively of the included sub-populations. 76

3.5 The differences in observed color between NTs in this paper and the literature as compared to the average error on our observations. The differences in g-r, r-i, and r-z observations are shown as blue, orange, and green histograms respectively. The average g-r, r-i, and r-z errors are shown as blue dotted, green dot-dashed, and orange dashed lines respectively 77

3.6 NT colors as a function of orbital elements (inclination on the top row, eccentricity on the middle row, and absolute magnitude on the bottom row). Grey points are taken from the literature (*Sheppard and Trujillo*, 2006; *Sheppard*, 2012; *Parker et al.*, 2013; *Jewitt*, 2018; *Lin et al.*, 2019; *Schwamb et al.*, 2019). Colored squares were measured in this paper. Duplicate observations of the same object are connected by dashed lines. The inset plots contain histograms of the Cluster Indices and Pearson Correlation Coefficients of a random distribution colors and orbital elements (see Sec. 3.5.1). Each grey dashed line in the inset plots shows the corresponding value calculated for the observed distribution. 79

3.7 The results of running a Principal Component Analysis (PCA) with the g-r and r-i colors of certain Solar System populations. The green histogram corresponds to the JTs (taken from *Hainaut et al.* (2012)). The blue and orange histograms correspond to the red and ultra-red subpopulations of the scattered TNOs, taken from *Hainaut et al.* (2012); the classification of red vs ultra-red was determined by using a clustering algorithm (DBSCAN; *Pedregosa et al.* (2011)) which separated the TNOs into two sub-populations. 81

3.8 Cumulative distributions of the Principal Component (see Sec. 3.5.2) values of populations in the Solar System. The cut-off between red and ultra-red as defined by this PCA is shown as a black dashed line (see Fig. 3.7). The cut-off between red and blue objects is similarly shown as a dot-dashed line. The JT and scattered TNO results are shown as orange and navy histograms respectively. The NTs observations from previous literature are shown as a blue histogram. The NT observations from this work are shown as a green histogram. . 82

4.1 NIRSpec spectra of red NT targets. The flux has been renormalized in this plot to be equal to 1 at wavelength = 1 μm. Each target's spectrum is shown as a various shade of blue. 97

4.2 NIRSpec spectra of ultra-red NT and all the red NTs averaged together. The flux has been renormalized in this plot to be equal to 1 at wavelength = 1 μm. The H_2O:CO_2 (10:1) spectrum is from the Leiden Ice Database for Astrochemistry (https://icedb.strw.leidenuniv.nl/), meaning we are comparing to an experimental dataset. The tholin spectrum is a synthetic spectrum taken from *Fernández-Valenzuela et al.* (2021). 98

LIST OF TABLES

Table

1.1 Current census of Trojan asteroid populations throughout the solar system. Targets are sorted by their planet and which Lagrange point they stably orbit. If the object is temporarily captured (orbital lifetime less than the age of the Solar System), they are recorded in the final column. There is no specific count for transient JTs, but based on the size of the stable population there is likely to be many. . . . 12

2.1 Source Extractor Parameters. The filter called "all-ground" is a 3x3 convolution mask with FWHM = 2 pixels. 31

2.2 Bullseye Parameters. R is the stationary source radius (measured by SE). See Sec. 2.4.2 for discussion of these parameters. 32

2.3 New Objects. The individual observations for all of these objects have been submitted to the *Minor Planet Center*. Columns: (1) Our designation for this object. The first number is the field and the second number is the chip the object was found in. The third number is a unique id; (2) Inferred V-band magnitude for the object. See Sec. 2.6.1 for a description of how the V-band magnitudes were calculated; (3) Rate of sky motion measured for the object (deg./day). The rate of motion is averaged over all of the detections; (4) Position angle measured for the object (deg.). The P.A. is averaged over all of the detections; (5) Number of detections of the object. 41

2.4 Previously Known Objects Flagged as ETs. The individual observations for all of these objects have been submitted to the *Minor Planet Center*. Columns: (1) Object Designation; (2) Orbit type taken from *SkyBoT* (*Berthier et al.*, 2006); (3) Predicted V-band magnitude (taken from *SkyBoT*); (4) Rate of sky motion measured for the object (deg./day). The rate of motion is averaged over all of the detections; (5) Position angle measured for the object (deg.). The P.A. is averaged over all of the detections; (6) Number of detections of the object. 42

3.1 NT targets of this survey. Columns: (1) Object Designation, has previous color measurements taken from 1: *Sheppard* (2012), 2: *Parker et al.* (2013), 3: *Jewitt* (2018), 4: *Lin et al.* (2019); (2) Lagrange Point; (3) Eccentricity; (4) Inclination (°); (5) Absolute Magnitude; (6) Dates observed; (7) Measured ave. SDSS r-band magnitude; (8) Measured SDSS g-r (mag); (9) Measured SDSS r-i (mag); (10) Measured SDSS r-z (mag); (11) Color classification determined based on each targets g-r vs r-i colors. 67

3.2 The resulting p-values of the KS Test on each combination of subpopulations considered in this work. 81

4.1 NT Spectroscopic Survey Targets 94

A.1 First Half of Survey Pointings. Columns: (1) Name of the Field. There were 8 distinct fields in this survey, observed 8 times each; (2) RA of exposure center (hours); (3) Dec of exposure center (degrees); (4) Start time of exposure (UTC). Every exposure was taken on 2018-06-16. 110

A.2 Second Half of Survey Pointings. Columns: (1) Name of the Field. There were 8 distinct fields in this survey, observed 8 times each; (2) RA of exposure center (hours); (3) Dec of exposure center (degrees); (4) Start time of exposure (UTC). Every exposure was taken on 2018-06-16. 111

B.1 Values needed to calculate ET upper limits. Columns: (1) H bin; (2) Recovery rate of injected Earth Trojans (see Sec. 2.6.2, 2.6.3) such that 1 = 100% of objects were recovered. If this column contains a dashed line, there were no injected objects in that H bin.; (3) Calculated upper limit without extrapolation for the number of ETs in each H bin (see Sec. 2.6.3). If this column contains a dashed line, there were no injected objects in that H bin, so we could not calculate an upper limit. 114

LIST OF APPENDICES

Appendix

A. Search for L5 Earth Trojans with DECam: Survey Pointings 109

B. Search for L5 Earth Trojans with DECam: Calculating Upper Limits Under Different Assumptions of the ET Population 112

ABSTRACT

This thesis reports on new results on Trojan asteroids throughout the Solar System. Trojan asteroids, which librate around a planet's L4 or L5 point, are a group of small bodies defined by their unique orbital properties and long term stability. Many Trojan asteroid populations are expected to be stable on order the age of the Solar System. Therefore, Trojans are likely relatively pristine remnants of the primordial disk. Therefore, studying their composition can give us a window into the composition of our proto-planetary disk. Since the Lagrange points are dependent on the orbit of the planet, Trojan asteroids are also sensitive to the dynamical history of the Solar System. This effect is particularly relevant for constraining the migration of the giant planets. The sizes and shapes of these objects also tell us what small planetesimals look like and how they coalesced. In short, Trojans are a key population for understanding the formation and evolution of the Solar System.

We currently know the most about Jupiter Trojans (JTs), a population with over 12,000 members. We know that they have rather dark albedos compared to other objects beyond the asteroid belt, but they have similar shapes and sizes to Trans-Neptunian Objects (TNOs) suggesting a common origin. Mars Trojans (MTs) on the other hand are the only stable Trojan population in the inner Solar System, and mostly appear to be covered in olivine, rare in the Solar System. Neptune's Trojans (NTs) appear to have a strange color distribution compared to their presumed source population, TNOs. Finally, Earth Trojans (ETs) are expected to exist based on numerical simulations, and while upper limits have been placed from previous searches, but no stable ones have been found.

All of these previous results leave many open questions about these populations regarding their origin and evolution. I address some of these questions in this thesis. In Chapter II, I present a search for L5 ETs using one hour of time on DECam on the 4m Blanco telescope. We did not discover any new ETs, but did place the most stringent constraints on the population to date. Based on these upper limits I rule out any ETs larger than about one km in size, but there could still be hundreds of undiscovered smaller ETs. A deeper search of this region is necessary to probe the smallest end of the size distribution to test the dynamical stability of this population.

The NT population has been found to be surprisingly lacking in ultra-red members, unlike the nearby Kuiper Belt. In Chapter III, I identify three new ultra-red NTs, bringing the red to ultra-red ratio in line with the TNO ratio. I also find that there is a color-orbit-size correlation in the NT population, which has implications regarding the formation of this population.

In Chapter IV, I present the results of a spectroscopic survey of the NT population. Specifically, I compare the JWST NIRSpec spectra of red NTs to ultra-red NTs, in order to determine if these objects differ in their surface composition. I find that they do indeed have similar but unique surface reflectance properties, where the ultra-red object appears to be covered in Tholins, a reddening agent. This result supports the theory that the NT population evolved into two separate components.

CHAPTER I

Introduction

1.1 Observing Physical Properties of Small Bodies in the Solar System

While most of the mass in the Solar System is by far dominated by the Sun, planets, and their satellites, the Solar System is full of other small rocky and/or icy bodies and dust, all termed "small bodies". Despite their diminutive sizes, these objects are key to our understanding of the history and evolution of the Solar System as they are the remnants of our proto-planetary disk. In other words, they are *the* building blocks of planets that, for many reasons, remain unconsolidated today. Therefore, they now serve as an *observable* fossil-like record of the history of our Solar System itself.

Small bodies is a term that covers a wide variety of sub-populations in the Solar System that can easily be classified by their orbits (see Fig. 1.1). Major sub-populations include the Main Asteroid Belt (between the orbits of Mars and Jupiter), the Kuiper Belt (beyond the orbit of Neptune), and the Oort cloud (the most distant region of our Solar System and the source of many comets). While all small bodies are somewhat the same - they are small (maybe icy) rocks - each sub-population provides a different piece to understanding the puzzle of our Solar System due to their

specific locations in the Solar System. For example, the Main Asteroid Belt exists in a different (i.e. much hotter) environment compared to the Kuiper Belt and thus is comprised of completely different compositions than those distant objects. Comets allow us to bridge the gap between the two and demonstrate what happens when you bring an icy outer Solar System object near the Sun. This thesis will focus on Trojan asteroids specifically (see Sec. 1.2), which are unique in their relationship to their associated planet and their orbital stability and can be found throughout the Solar System. For a review of the study of other populations of small bodies see *Fernández* (2003); *Brown and Firth* (2016); *Hestroffer et al.* (2019); *Horner et al.* (2020).

The study of these Small Bodies is truly inter-disciplinary, lying at the intersection of astronomy, chemistry, geology, geography, and planetary science. In this thesis, I will focus on the study of small bodies from an astronomical perspective which relies primarily on remote sensing of these objects. However, this should not discount the important and fascinating role that space probes and sample return missions have had to play in this field, missions such as Rosetta, Hayabusa(-2), Osiris-REx, and most recently DART and Lucy. Each of these missions has/will revolutionize our understanding of these populations but are beyond the scope of this thesis. I will also not cover meteoroids that have been recovered from Earth's surface, which typically fall under the umbrella of geology. However, these objects are a key inventory of samples from small bodies in near-Earth orbits. Studying direct samples will allow us to study the makeup of small bodies far more in-depth than we ever could with remote sensing. However, Astronomy remains a key tool in the toolbox of planetary sciences that allows us to study the overall populations in their native environment with existing facilities. And there is much to be learned from astronomical observations. For one, Astronomy will always be driving the discovery of these objects and will be vital to their first basic physical characerizations. Remote sensing can tell us the size, shape, compostion, and even internal structure of these objects without ever

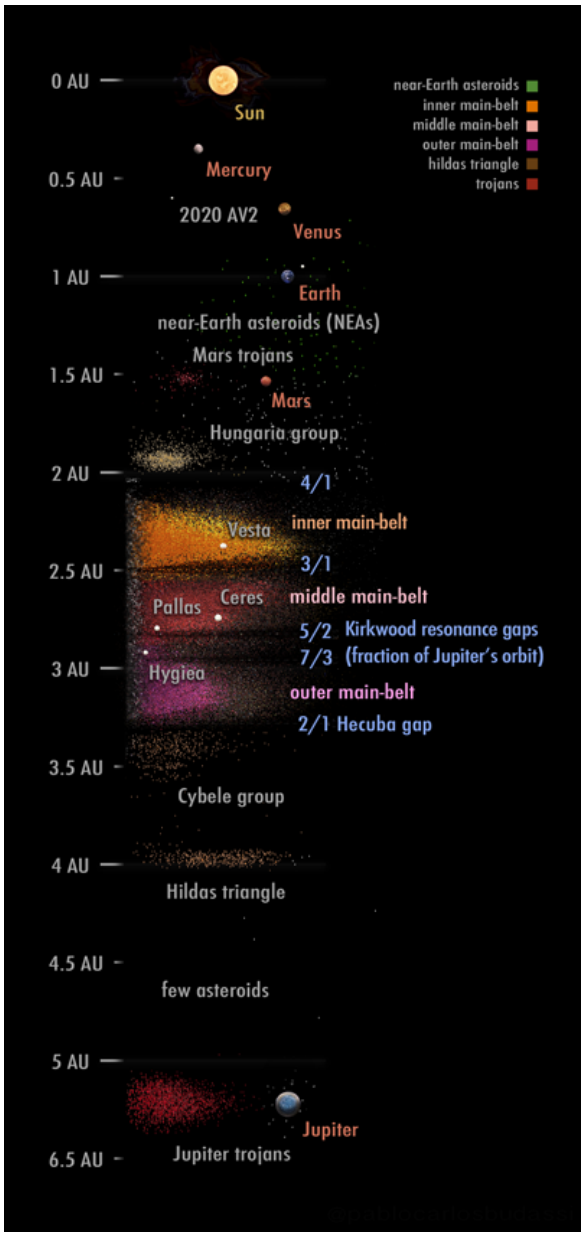

Figure 1.1: Distribution of small bodies in the inner Solar System based on distance from the Sun (in AU). Different sub-populations are colored and labeled in the plot. The Hilda and Trojan asteroids are clusters around 4 and 5.1 AU respectively and are in resonance with Jupiter. The Kirkwood gaps are also driven by Jupiter's resonances.

leaving our planet. Again, planetary science missions to these objects are still vital and provide far more data on *specific* targets than remote sensing ever could, but it is Astronomy that provides the foundation for these revolutionary missions.

1.1.1 Discovery

The very first step to studying small bodies is their discovery. Small bodies have arguably been studied since ancient times as the brightest comets could be observed with the naked eye. The first comet discovered by telescope was the great comet of 1680 by Gottfried Kirch (*Seargent*, 2008). Since then, the discovery of small bodies has exploded with over 1 million objects being recorded on the Minor Planet Center, a database of known small bodies[1]. However, these objects are now primarily discovered through large astronomical surveys that cover large portions of the sky such as the Dark Energy Survey (DES), OSSOS, and Pan-STARRS. Some of these surveys have been dedicated to the discovery of Solar System objects (such as OSSOS) while others have merely been serendipitiously fortuitous samples. However, dwarfing them all will be the Vera C. Rubin Observatory's Legacy Survey of Space and Time (LSST), covering about 20,000 square degrees of sky, taking more than five million exposures, and collecting over 50 petabytes of data over the course of the 10 year survey [2]. This field is about to become inundated with new small bodies which will revolutionize the field.

But how exactly are these objects discovered? Since these targets are within the Solar System and orbit relatively close to the Earth, they exhibit significant apparent motion across the sky, especially as compared to background stars and galaxies. Therefore, one simply needs to look for new moving targets to identify new small bodies in the Solar System. This basic method has been utilized since ancient times to distinguish "wandering" planets from distant stars. A more sophisticated

[1]https://www.minorplanetcenter.net/
[2]https://www.lsst.org/scientists/survey-design

method which allows for measuring subtle motions of faint objects using a telescope is the blink comparator, such as was utilized by Clyde Tombaugh to discover Pluto (*Schindler and Grundy*, 2018). Today, the same basic principle is applied, taking multiple images and looking for moving objects, but rather than being identified by hand, sophisticated numerical algorithms are being developed. For example, one method is to take the difference between two images of the same field; doing this will remove stationary stars but leave moving targets to be easily identified by some sort of source extraction software and pulled out of the data. Doing so generates "tracklets", multiple observations of the same moving target which can then be linked together to constrain the objects orbit (see Sec. 1.1.2). This method has been used in many papers and surveys for decades to look for moving objects.

However, this method is limited to the exposure depth of the individual images taken by a telescope. In most astronomical contexts, to increase the exposure depth one would take longer exposures. This method does not work for moving targets however as they will move significantly across the focal plane between exposures which causes them to become smeared and actually harder to detect. One solution to this problem is to use a Shift-and-Stack algorithm in which you shift each exposure by the rate of motion across the sky of the object and *then* stack your exposures to increase the depth. In this way, the background stars become smeared while the moving target is a point source that follows the typical $\sqrt{n}$ signal to nose ratio (SNR) law. The downside of this method is that you do not know the rate of motion for undiscovered objects *a priori*. Therefore, one may choose to brute force the problem by searching a grid of possible speeds and using a source extraction tool at each iteration to look for new point sources. This solution can be prohibitively computationally expensive, but if one can make assumptions about the targets that reduce the grid size this method becomes viable, acting as a powerful tool for pushing the detection limits of the survey. For examples of surveys that have utilized Shift-and-Stack see *Gladman and*

Kavelaars (1997); *Allen et al.* (2001); *Bernstein et al.* (2004); *Heinze et al.* (2015); *Rice and Laughlin* (2020). A more modern version of Shift-and-Stack is using a maximum likelihood estimate for the probability of the detection of a source within a series of images. This technique can search over 10^{10} possible asteroid trajectories in under a minute on a single GPU (*Whidden et al.*, 2019). Such fast methods will be necessary to deal with the influx of discoveries in an LSST-era.

1.1.2 Orbital Characterization

While a solar system object can be identified by its motion across the sky, further observations are required to actually constrain the target's orbit. Tight constrains on an object's orbit are needed in order to classify it, especially into a resonant population, where the orbital periods of the resonant objects are in a simple integer relations with the orbital period of a planet. The longer the observational arc, the tighter the constraints on the orbit. There are centuries-old solutions to fitting an orbit based on observed arcs, and predicting a position using the object's orbit is a solved problem (e.g. JPL HORIZONS[3]).

However, orbits are of interest beyond being able to locate and track the target. In particular, the dynamics of the Solar System are driven by the evolution of the constituent orbits. The orbits of small bodies retain memory of the evolution of the Solar System, in how their orbits are configured today. Therefore, numerical simulations, such as n-body simulations, are key to understanding how the orbits of Solar System Objects have changed over time. Such models have been used to suggest there may have been an additional ice giant (*Nesvorný*, 2011), a jumping Jupiter (*Nesvorný et al.*, 2013; *Roig and Nesvorný*, 2015; *Roig et al.*, 2016; *Gaspar et al.*, 2017; *DeSouza et al.*, 2021), or migratory giant planets (*Malhotra*, 1993, 1995). The orbits of small bodies are tied to these histories and serve a constraint on evolutionary

[3]https://ssd.jpl.nasa.gov/horizons/

models.

1.1.3 Size Distribution

One of the earliest physical measurements we can take of a small body is its size. In particular, the target's absolute magnitude (brightness at 1 AU away from the sun while full illuminated) is related to its size based on the following equation (*Bowell et al.*, 1989; *Harris and Harris*, 1997):

$$D = 10^{3.1236 - 0.5 log_{10}(a) - 0.2H} \tag{1.1}$$

where D is the diameter of the object in km, a is geometric albedo, and H is absolute magnitude. Note this expression assumes a spherical object with a uniform surface. The size of an object can tell us a lot about its history. For example, objects that experienced any collisions in their past will be smaller and more numerous pieces of the parent body. Therefore, a populous group of *small* bodies may be an indication of a history of collisions. However, large objects can also be broken up by the YORP effect, whereby asteroids are broken up due to their rotation (*Christou et al.*, 2020). Small bodies can also be disrupted by the Yarkovsky effect, in which objects are thermally accelerated off of their orbit (*Xu et al.*, 2020b; *Galushina and Letner*, 2020; *Xu et al.*, 2020a; *Fenucci and Novaković*, 2021). In this way, the size distribution of small bodies can tell us about their history and evolution. For example, we expect that some of the largest objects in the Solar System are some of the most primordial as they have not been modified by these phenomena (*Sugiura et al.*, 2018).

However, measuring size based on optical magnitude is limited due to the assumptions of the model. Size can also be measured using more accurate techniques such as thermal radiation through radio observations (*Delbo et al.*, 2015; *Gerdes et al.*, 2017; *Müller et al.*, 2018) or direct orthogonal radius through occultations (*Alvarez-Candal*

et al., 2014; *Schindler et al.*, 2017; *Strauss et al.*, 2021; *Leiva et al.*, 2020). These methods have not been utilized on a large selection of targets, meaning our understanding of the true size distribution, and thus our historical understanding of the Solar System, is limited.

1.1.4 3-dimensional Shape

Related to the size distribution, what are small bodies in the Solar System shaped like? Are they spherical or irregular? Smooth or rough? We have a variety of ways that we can measure the shape of these objects directly and indirectly. As with the size measurements, occultations can be used to measure the shape of the target, especially identifying any deviations from being spherical. Shape (and binarity) can also be inferred from variation in a target's lightcurve (*Cellino et al.*, 1989; *Ďurech et al.*, 2018; *Navarro-Meza et al.*, 2021). There have also been radar observations taken to address this question (*Ostro and Connelly*, 1986; *Greenberg and Margot*, 2015; *Shepard et al.*, 2017), though with the loss of Arecibo the future of this kind of research is not clear. Finally, shape of an object can be measured from direct images as is the case in space probe missions. These up close images have shown us in exquisite detail that at least some of these bodies are non-spherical, have surface geology, and are made of rubble. The shapes of these objects are modified though collisions, which were more common early in the Solar System. These interactions can be studied and tested through numerical simulations, such as smoothed-particle hydrodynamics (SPH) methods or n-body simulations with material strength. Such models are able to recreate the strange shapes observed in the Solar System (*Michel and Richardson*, 2013; *Jutzi and Asphaug*, 2015; *Jutzi and Benz*, 2017; *Schwartz et al.*, 2018)

1.1.5 Surface Composition

The composition of the surfaces of small bodies is of great interest since these objects are remnants of the building blocks of planets. In other words, the current composition of these objects provides a window into the composition of our primordial disk. The first-order measurement of surface composition is color. For objects in the outer solar system, these objects start out icy due to their distance from the sun, and those ices give it a blue color. Over time, this surface is exposed to solar irradiation, which darkens and reddens the surface over time. However, if the object experiences any collisions, this dark crust can be knocked off exposing the blue ice underneath (*Luu and Jewitt*, 1996). Therefore, color can be an indication as to the history of collisions and irradiation on the surface of outer Solar System objects. The story is similar for objects nearer the Sun in the inner Solar System; surfaces of these small bodies are dominated by space weathering (micrometeorite impacts and solar irradiation; *DellaGiustina et al.* (2020)). These objects however tend to be more grey in color from their rocky (rather than icy) surfaces. The surfaces still tend to redden over time, but composition is limited by what volatiles can exist at a nearer distance to the Sun.

Surface composition can be measured more precisely than color though through reflectance spectroscopy, where absorption of solar light scattered off of these rough bodies relates to the composition of its surface material. Spectroscopic analysis is certainly more accurate for samples actually taken from the surface of these objects (such as for the Hayabusa-2 and OSIRIS-REx missions), but reflectance spectroscopy can be conducted remotely through ground and space-based facilities. These observations have been made for the largest small bodies which are brighter and easier to study. For a review of spectroscopic observations of small bodies, see *Vernazza and Beck* (2016). In short, spectroscopy is used to classify objects based on their optical and near-IR spectra (see Fig. 1.2 for an example of asteroid classification schemes),

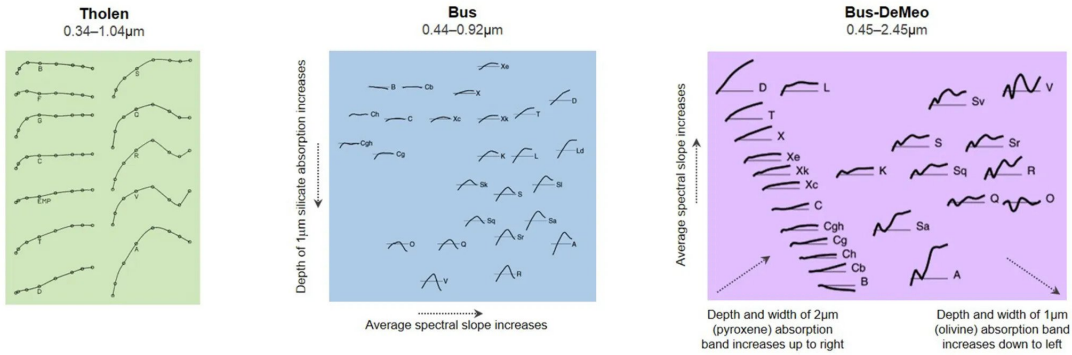

Figure 1.2: Various asteroid classification schemes based on optical reflectance spectra (*Tholen*, 1984; *Bus*, 1999; *DeMeo et al.*, 2009). The Bus-DeMeo scheme is the most contemporaneous with this work. Targets are classified by comparing spectral features such as slope and band position and shape (band centers, band depths, band widths, band area ratios) to these example spectra.

allowing us to track composition throughout the Main Asteroid Belt. Compositional measurements are harder to take for more distant objects, so a unified theory of outer solar System composition does not exist. However, we have learned that outer Solar System objects appear distinct from their main belt counterparts, though outer Solar System material has also been found closer to the Sun than expected (*Hasegawa et al.*, 2021), demonstrating that material has been transported to different locations throughout our Solar System.

Many volatiles have ice bands in the near-IR, making this region of light a particularly useful for constraining the surface composition of small bodies. Therefore, this field is about to be revolutionized by the newest, most powerful telescope at those wavelengths, JWST. JWST's spectral coverage makes it an ideal tool for studying these objects and its sensitivity will allow for the characterization of a population fainter than we have ever been able to study before. Data collection for this telescope is currently underway, so modern interpretation of the composition of these objects is upcoming in JWST observations (*Stansberry et al.*, 2017; *Guilbert-Lepoutre and*

Ferruit, 2017; *Rivkin et al.*, 2017; *Thomas and Rivkin*, 2017; *Parker*, 2017; *Hines et al.*, 2017; *Lunine*, 2017; *Trilling et al.*, 2021; *Markwardt et al.*, 2021; *Pinilla-Alonso et al.*, 2021; *Brown et al.*, 2021).

1.1.6 Interior Structure

Finally, we have perhaps the most difficult property of small bodies to measure from an astronomical context, the internal structure and mass of small bodies. If the small body is orbiting in a binary this issue becomes easier to solve as the orbits of the binary can be used to calculate the relative mass of the two objects. Mass has been measured for a select number of small bodies this way (*Brown and Schaller*, 2007; *Ragozzine and Brown*, 2009; *Grundy et al.*, 2019). However, density and internal strength of an object can also be measured through thermal observations (*Brown and Butler*, 2017). One of the most direct ways we've had to measure this property is through the DART mission which collided with an asteroid in a binary system to try to change its orbit. While the change in orbit can be easily measured using lightcurves from telescopic facilities, the internal structure can also be constrained by modeling the collision and energy imparted into the system. These results are also currently being studied with more detailed modeling of the system coming from observations taken by the followup mission LICIACube. Together these missions will revolutionize our understanding of the internal structure of small bodies in the Solar System.

1.2 Trojans: 1 to 1 resonators

Lagrange points, the first three of which were discovered around 1750 by Euler and the later two by Lagrange around 1760 (*Ross et al.*, 2011), are the natural gravitational outcome of a three-body problem. Points L_1, L_2, L_3 lie along a line from the planet to the Sun and are unstable equilibria points. The L_4 and L_5 points which lie 60° ahead of and behind the planet at the point of an equilateral triangle on the

Planet	L4	L5	Temporary Capture
Mercury	–	–	–
Venus	–	–	1
Earth	–	–	2
Mars	1	8	–
Jupiter	7964	4226	many
Saturn	–	–	1
Uranus	–	–	2
Neptune	27	3	1

Table 1.1: Current census of Trojan asteroid populations throughout the solar system. Targets are sorted by their planet and which Lagrange point they stably orbit. If the object is temporarily captured (orbital lifetime less than the age of the Solar System), they are recorded in the final column. There is no specific count for transient JTs, but based on the size of the stable population there is likely to be many.

other hand are stable equilibrium points which can support orbits along a large range of libration amplitudes extending far from the nominal Lagrange point. This region of space is known to harbor planetesimals with orbits that are stable on order the age of the Solar System (*Ćuk et al.*, 2012; *Malhotra and Jeongahn*, 2011; *Tabachnik and Evans*, 2003; *Marzari and Scholl*, 2013). Due to this long-term stability, objects that librate around a planet's L_4 and L_5 point (i.e. Trojan asteroids) are presumed to be remnants of the primordial solar system. In fact, the current studies of Trojan asteroids highlight these targets as the "fossils" of our Solar System (*Olkin et al.*, 2021) and their current day composition and physical characteristics can provide a window into the environment that our Solar System was born from. Small bodies have been known to exist at these unique gravitational points since 1906 when Max Wolf discovered the first Trojan companion of Jupiter (*Nicholson*, 1961). Since then, Jupiter Trojans (JTs) have been by far the most well studied Trojan population, with over 12,000 having been discovered to date. However, Trojan asteroids have been discovered around every other planet, excluding Mercury. A current census of Trojan asteroids across the Solar System is included in Table 1.1.

1.2.1 Jupiter Trojans

The first to be discovered and the largest Trojan population is Jupiter's Trojans (JTs). With over 12,000 having been discovered to date, our understanding of Trojan asteroids is dominated by this population which could be as abundant as the main asteroid belt itself (*Emery et al.*, 2015). However, despite being relatively closer to the main belt, observations indicate that JTs are actually from the Kuiper Belt, which was scattered during the period of planetary migration (*Tsiganis et al.*, 2005; *Morbidelli et al.*, 2005; *Nesvorný and Morbidelli*, 2012). This explanation is not sufficient to recreate one of the most robust observations of this population though, the L4 vs L5 asymmetry (nearly 2 to 1; see Table 1.1). The asymmetry in the L4/L5 population is robust (i.e. not due to observational biases) and has been repeatedly noted since *Shoemaker et al.* (1989). Instead, a "jumping Jupiter" model, in which Jupiter experiences a rapid outward jump in its orbit perhaps due to a 5th ice giant that was subsequently expelled from the Solar System, has been adopted as it is able to recreate the asymmetry (*Nesvorný et al.*, 2013). This model has also been invoked to explain other phenomena in the Solar System such as the moon-forming impact (*DeSouza et al.*, 2021) or Mercury's orbit (*Roig et al.*, 2016). Therefore, JTs represent a key constraint on migration models.

JTs have been observed to have rather dark albedos ($\sim$0.07), meaning little light is reflected back off their surface (*Fernández et al.*, 2003; *Grav et al.*, 2012), especially compared to Trans-Neptunian Objects (TNOs) which have a mean albedo $\sim$ 0.17 (*Johnston*, 2022). These surfaces have been highly irradiated (even more so than TNOs) creating a dark crust on their surface, likely leading to their dark albedos. However, high-albedo JTs have recently been observed which are potentially associated with impacts, indicating that the *interiors* of these objects may be icy and thus have a higher albedo (*Simpson et al.*, 2022). Unfortunately, these objects have been observed to have nearly featureless reflectance spectra defying a compositional

classification (*Fornasier et al.*, 2007; *Emery et al.*, 2011; *Brown*, 2016). However, based on photometric and spectroscopic evidence, there do appear to be two distinct color populations, the "red" and "less red" JTs (*Szabó et al.*, 2007; *Roig et al.*, 2008; *Wong et al.*, 2014; *Wong and Brown*, 2015). These colors correlate to object size, with fainter objects tending to be less red (*Pan et al.*, 2022). This trend may be another indication that less red objects are collisional fragments (which would tend to be smaller) (*Wong and Brown*, 2016), but with no detected spectral features, this idea is difficult to confirm (*Pan et al.*, 2022).

We know that this population is comprised primarily of small bodies, but the largest known JT is Hektor between 203 and 239.2 km in diameter. The JT size distribution is well modeled as a cumulative power law ($N(> D) = a_0 D^{-\alpha}$) of index of 2 (*Grav et al.*, 2011), with a steep cutoff around 80 km (*Shoemaker et al.*, 1989; *Grav et al.*, 2011; *Fraser et al.*, 2014). This size distribution has been found to be most consistent with that of the "hot" (i.e. dynamically excited) TNO population (*Fraser et al.*, 2014). This result suggests that JTs are less dynamically stable TNOs that were scattered inward towards the Sun during the period of planetary migration. These size distibutions are based on the entire JT population, but we also have constraints on the size and shape of specfic objects from recent occultation measurements (*Buie et al.*, 2015; *Berthier et al.*, 2020; *Mottola et al.*, 2020; *Hasegawa et al.*, 2021). Shape models have demonstrated that the objects are non-spherical in nature and can have topography on the surface at scales of tens of km. Such observations have also been used to identify JTs with satellites, demonstrating that JTs may form in binaries like other populations of small bodies in the Solar System (*Bernardinelli et al.*, 2020). The existence of ancient binaries has also been argued to be evidence of very early (<100Myr) planetary migration (*Nesvorný et al.*, 2018). In short, while JTs may not look like TNOs based on their color, they do have very similar shapes and sizes which perhaps points to a common, ancient origin.

1.2.2 Mars Trojans

The only stable trojan asteroids in the inner Solar System are Mars Trojans (MTs). This population exhibits asymmetry between the L4/L5 points that is superficially similar to that of JTs; however, this asymmetry is dominated by a collisional family (named after its largest member, Eureka) at the L5 point rather than being due to planetary migration (*Christou*, 2013). Spectral observations indicate that members of this family are covered in olivine (*Rivkin et al.*, 2007; *Lim et al.*, 2011; *Borisov et al.*, 2017; *Polishook et al.*, 2017). Olivine is not generally common in small bodies of the Solar System (*Sanchez et al.*, 2014; *DeMeo et al.*, 2019), but is present in the Martian mantle material suggesting that MTs are captured from some early collision on Mars rather than being captured from elsewhere in the Solar System (*Polishook et al.*, 2017). However, there is one L5 Trojan that is an outlier and likely not a part of the Eureka family, $1998VF_{31}$. In contrast, this MT is most similar to an S-type asteroid (*Rivkin et al.*, 2003, 2007; *Trilling et al.*, 2007) which has been directly measured through sample returns from the Hayabusa mission to have ordinary chondrites on their surface (*Nakamura et al.*, 2011).

The lone L4 MT, 1999 UJ_7, on the other hand, has a much different composition, having been identified as a featureless X-type (*Rivkin et al.*, 2003) or a C-complex type (*Borisov et al.*, 2018). The more recent observation of this object suggest that the surface could be covered in hydrated materials and, if 1999 UJ_7 is a primitive object, this result could be an indication that this object formed beyond the snow line, was subsequently scattered and captured into the MT region where it has been thermally altered over time (*Borisov et al.*, 2018). Thus while most of the L5 MTs are tied to the formation and collisional evolution of Mars, 1999 UJ_7 may inform our understanding of outer Solar System objects and how they evolve when transported into the inner Solar System.

1.2.3 Neptune Trojans

Neptune Trojans (NTs), are the second largest population of Trojans in the Solar System based on members that have been discovered; however, the population may be as big if not bigger than the JT population (*Lin et al.*, 2021). Like JTs, NTs also exhibit an asymmetry between their L4/L5 points, but this is likely an observational bias; the L5 point has overlapped with the galactic plane in recent years, meaning that the search fields have been dominated by background stars significantly increasing the difficulty in finding moving objects. Deeper surveys of the NT regions, particularly around L5 are clearly needed.

However, much has been learned from even the small population we have now. A size distribution based on the current population has been calculated and it measured that the population follows a steep cumulative power law index of 5 with a cutoff around 45 km; these results are consistent with other populations in the solar system leading to the conclusion that NTs and all other Solar System populations are lacking intermediate-sized planetesimals, 35 to 50 km in size (*Sheppard*, 2010). The cause of this paucity is not clear, but since it is seen everywhere in the Solar System there must be some mechanism driving the growth directly from small to large planetesimals.

The most intriguing property of this population is the color distribution. Similar to the JTs, NTs are not expected to have formed *in-situ*, but rather are planetesimals that were scattered and subsequently captured during the period of planetary migration (*Kortenkamp et al.*, 2004; *Tsiganis et al.*, 2005; *Nesvorný and Vokrouhlický*, 2009; *Lykawka et al.*, 2009; *Lykawka and Horner*, 2010). The most likely source of these scattered objects is the nearby Kuiper Belt. If that were the case, one would expect that these populations have similar surface compositions, which can be measured through their surface color distribution. It has been well-established that there is a bimodality of color in the Kuiper Belt, with the "red" population having g-r < 0.75 and the "ultra-red" population having g-r > 0.75 (*Sheppard*, 2010; *Schwarz*

et al., 2011; *Hainaut et al.*, 2012; *Peixinho et al.*, 2012; *Sheppard*, 2012; *Lacerda et al.*, 2014; *Peixinho et al.*, 2015; *Pike et al.*, 2017b; *Wong and Brown*, 2017b; *Schwamb et al.*, 2019). Conversely, NTs leaking out of the Lagrange cloud are also thought to be the source population for Centaurs, objects that orbit between Jupiter and Neptune (*Horner and Lykawka*, 2010). These objects are also red and ultra-red in color (*Peixinho et al.*, 2012, 2015).

Through 2018, no ultra-red NTs had been found, making their color distribution distinctly different than their expected origins or offshoots; this tension was termed the "Trojan Color Conundrum" (*Jewitt*, 2018). But *why* do these populations have different color distributions? Something must have happened to the surfaces of these objects to modify their composition. Looking to JTs, they also lack ultra-red members which is thought to be due to thermal resurfacing (*Luu and Jewitt*, 1996; *Jewitt*, 2002). However, the temperatures at the distance of Neptune are too cold for this to be the explanation in this case (*Jewitt*, 2018). Instead, NTs may be collisionally resurfaced, where collisions strip the ultra-red crust off of the surfaces of these bodies revealing a bluer surface underneath. One source of such collisions could be plutinos, 3:2 resonators with Neptune, which have significant orbital overlap with the NT population (*Almeida et al.*, 2009). Such collisions are expected to occur when plutinos have high libration amplitudes, high eccentricities, and low inclinations; therefore, we would expect the color distribution of NTs to be inclination-dependent as well, where high inclination NTs avoid these collisions and retain their ultra-red surfaces. Finally, this discrepancy could be due to a primordial boundary between red/ultra-red bodies that was subsequently mixed by Neptune's migration (*DeMeo and Carry*, 2014; *Neveu and Vernazza*, 2019). Based on the exact nature of the epochs of radial mixing, mass removal, and planet migration, the resulting NT population could be devoid of ultra-red members while the Centaur population is not (*Neveu and Vernazza*, 2019), but specific simulations of these two populations have not been conducted. This

hypothesis has been supported by the discovery of two TNO-like (red) objects all the way in the asteroid belt (*Hasegawa et al.*, 2021).

In 2019, the first ultra-red NT, 2013 VX_{30}, was discovered (*Lin et al.*, 2019), potentially resolving this conundrum. However, the red to ultra-red ratio now stands at 17:1 rather than in the range from 4:1 to 11:1 as observed for TNOs (*Schwamb et al.*, 2019). Of note, 2013 VX_{30} is a high inclination NT, supporting the hypothesis that high inclination objects are protected from Plutino collisions. However, colors have only been measured for 16 OF 31 NTs (*Sheppard and Trujillo*, 2006; *Sheppard*, 2012; *Parker et al.*, 2013; *Jewitt*, 2018), so the true color distribution is still not well determined. Solving this problem will lead to a better understanding of the formation and evolution of planetesimals in the outer Solar System.

1.2.4 Temporarily Captured Objects

Not all Trojan asteroids are stable on order the age of the Solar System. In fact, all planets, except Mercury (with no Trojan asteroids) and Mars, have temporarily captured co-orbitals (*Wiegert et al.*, 1998; *Karlsson*, 2004; *Mikkola et al.*, 2004; *Horner and Lykawka*, 2012; *Alexandersen et al.*, 2013; *Greenstreet et al.*, 2020). While these objects are common in the Solar System, they are more limited in the information they can provide regarding formation and evolution of the protoplanetry disk. These objects have lifetimes <1Myr, meaning they are not "primordial" like true Trojan asteroids. They can tell us how planetesimals are transported throughout the Solar System. However, determining where they originated in the disk is difficult to impossible in most cases, so the constraints they can provide are limited. The scattering population has also shown a deficit in intermediate sized objects, providing further evidence that there is a primordial origin for the paucity of intermediate sized planetesimals (*Alexandersen et al.*, 2013; *Shankman et al.*, 2013). Therefore, temporary captured co-orbitals are common and can tell us about the scattering population

in the Solar System, but they *cannot* tell us about our planetesimal disk and its evolution like true primordial Trojans can.

1.2.5 Earth Trojans?

Numerical simulations have shown that Earth Trojans (ETs) should have orbits which are stable on order the age of the Solar System (*Ćuk et al.*, 2012; *Malhotra and Jeongahn*, 2011; *Tabachnik and Evans*, 2003; *Marzari and Scholl*, 2013). However, only two temporarily captured ETs have been discovered to date (*Connors et al.*, 2011; *Hui et al.*, 2021). Estimated lifetimes of 2010 TK_7 vary from ∼7000 years (*Connors et al.*, 2011) to about ∼0.25 Myrs (*Dvorak et al.*, 2012); 2020 XL_5 is thought to have been implanted into its current orbit in the fifteenth century and has a 99.5% chance of leaving the L4 region within the next 10 kyr (*Hui et al.*, 2021). Therefore, a truly primordial ET population remains elusive. Also of note, these are both L4 ETs, leaving a complete paucity of L5 ETs. A search for these primordial objects is needed (*Malhotra*, 2019).

One must then ask, why have no stable ETs been discovered? One explanation is that the Yarkovsky effect could destabilize ETs that are less than 400m in size (*Zhou et al.*, 2018). However, upper limits from surveys of the ET region suggest that there may still be tens to hundreds of objects with radius >400m in size (*Markwardt et al.*, 2020, and references therein). These surveys also rule out any ETs $>\sim$ 1 km. Large objects are likely limited by the YORP effect like the Eureka family of MTs (*Christou*, 2019), but they may also be ground down by collisions depending on the density of the primordial population. But what about the missing hundreds of sub-km sized objects? One study showed that if Earth acquired the final 1% of its mass through on order of 10 collisions, then only 1% of the previously bound Trojan population would remain; such collisions could have happened during Earth's Late Veneer or the moon-forming impact (*Napier et al.*, 2022). Additionally, the largest

n-body simulation to date has found that portions of the ejection pattern of ETAs align well with changes in Earth's orbital elements that cause the Milankovitch cycles that have been indicated in the climate record of Earth (*Yeager and Golovich*, 2022). In short, there are many reasons that Earth's primordial Trojan population could have been destabilized explaining why only temporarily captured objects have been discovered to date.

1.2.6 Other resonant populations

While the 1:1 mean motion resonance is generally the strongest and most stable, objects have been found at higher order resonances, mostly of Neptune in the Kuiper Belt (see Fig. 1.3). Perhaps the most famous of these objects is Pluto which is the largest of a class of objects called Plutinos which are in a 3:2 resonance with Neptune. Plutinos remain the largest resonant Trans-Neptunian Object (TNO) population (*Gladman et al.*, 2012). The record for most distant resonance is two objects in the 9:1 resonance at ∼130 AU (*Volk et al.*, 2018). Resonant objects are expected to have a similar origin to Trojan asteroids in that they are also expected to be scattered objects captured into a resonance during planetary migration (*Gladman et al.*, 2012, and references therin). Since resonant objects make up a 75% of the mass of the main belt, a torus-shaped region of asteroids between Mars and Jupiter (*Gladman et al.*, 2012), they are a powerful tool for constraining planetary (especially Neptune's) migration. Models that recreated observed resonant populations have shown that Neptune's migration was likely slow and grainy (*Lawler et al.*, 2019). The leading n:1 resonances should also be more populated than their trailing ones (*Pike et al.*, 2017a), which has so far been observed to be true for Neptune Trojans (see Table 1.1). These resonances are well recreated from a migrating Neptune model, except for the 5:1 which is overpopulated compared to theory (*Pike et al.*, 2017a). However, a migratory model may not even be necessary to create the resonant population if

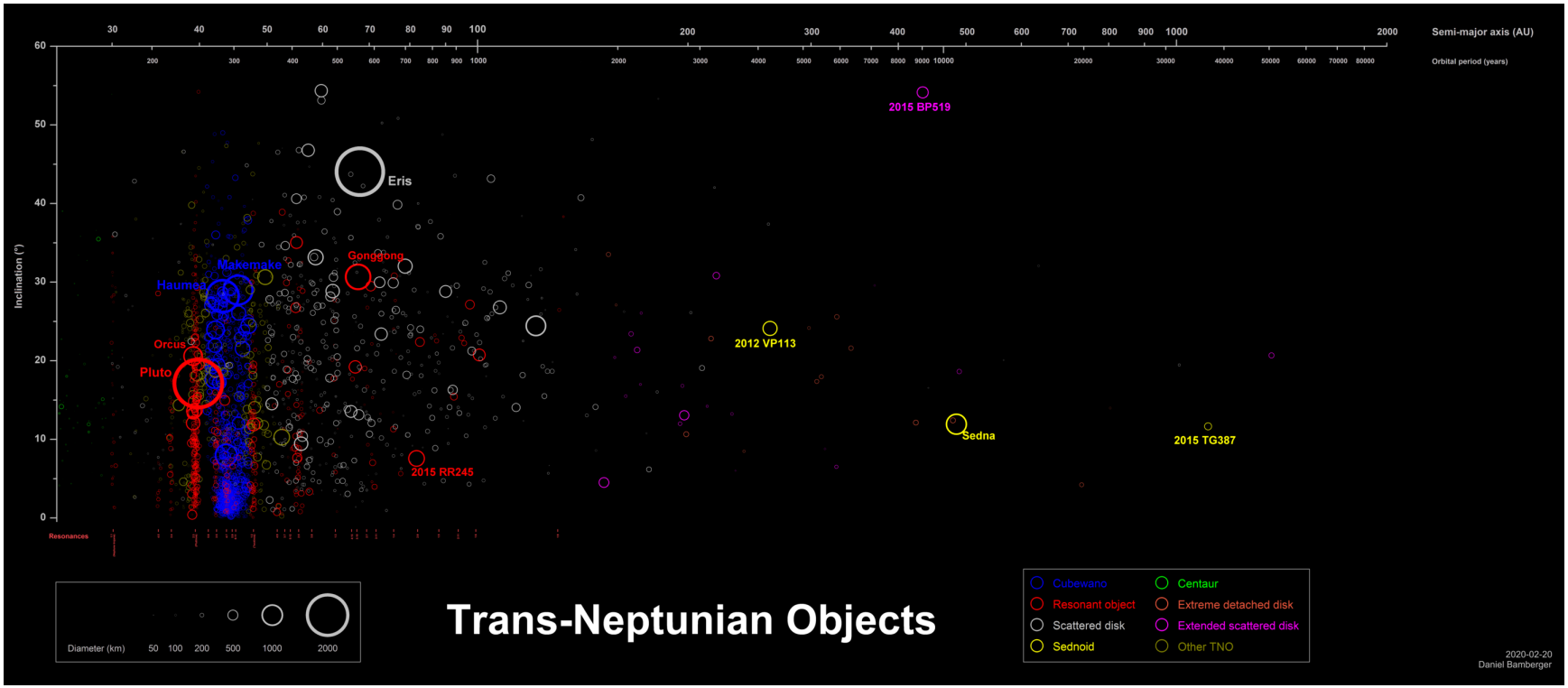

Figure 1.3: Semi-major axis (a) of outer Solar System objects vs inclination (i). Objects are color-coded based on their dynamical class. Resonant objects are shown as red circles and generally lie along lines of constant semi-major axis. The size of each circle corresponds to the diameter of the object. Pluto is by far the largest resonant TNO.

rogue 2 Earth-mass sized planet interacted gravitationally with the proto-Kuiper Belt (*Huang et al.*, 2022).

Jupiter's resonances also drive concentration or gaps in both the inner and outer Solar System. The most well studied set of objects, other than JTs, are Hildas, which lie in the 3:2 resonance. Hildas are thought to be a potential source for Jupiter Family Comets and are thus connected to the rest of the Solar System (*Di Sisto et al.*, 2005). Like JTs, Hildas are dark in albedo. Their high-albedo members have the same composition and must have a similar origin but somehow evolved to be brighter (*Marsset et al.*, 2014). Based on their colors and magnitudes, JTs and Hildas also come from the same source population (*Wong and Brown*, 2017a). In this way, Hildas and JTs are very similar and can both provide constraints on the evolutionary history of the protoplanetary disk.

1.3 Structure of Thesis

In Chapter II, I present the results of a contemporary search for L5 ETs with DECam on the Blanco 4m telescope. In this search, we found no new ET candidates (based on their rate of motion across the sky). We did identify 27 tracklets that did not correspond to a previous known Solar System object. Based on our non-detection of ETs, we place upper limits on the population of ∼60 - 85 ETs 390m in size and 97 which are 290 m in size.

In Chapter III, I measured the griz colors for 17 of 31 known NTs, including 11 targets with no previous color measurement. We confirm $2013VX_{30}$ is ultra-red in color along with four NTs identified as ultra-red for the first time in this survey. We also show that there is a color-orbit-size correlation in the NT population, though the explanation as to why is not clear.

In Chapter IV, I present preliminary results from our NIRSpec reflectence spectrum survey. We find that red NTs are covered in H_2O and CO_2 ice, while the

ultra-red NT is covered in tholins, known reddening agents. This result suggests that NTs have a similar composition that is irradiated over time (giving you ultra-reds). Reds are then created when collisions knock off the ultra-red crust and reveal the original ice underneath.

In Chapter V, I give concluding remarks and discuss the future of this field.

CHAPTER II

Search for L5 Earth Trojans with DECam

2.1 Preface

This chapter appears in the Monthly Notices of the Royal Astronomical Society, Volume 492, Issue 4, March 2020, Pages 6105–6119 (Markwardt et al. 2020). The paper is led by Markwardt and co-authored by D W Gerdes (who advised Markwardt during this paper), R Malhotra (who ran the dynamical simulations required to generate the synthetic ET population), J C Becker, S J Hamilton, and F C Adams (all of whom contributed to the manuscript itself), and is reproduced here with minor stylistic revisions.

2.2 Introduction

The population of Earth Trojans (ETs) represents an important (if perhaps not abundant) part of our Solar System because it can provide constraints on the Solar System's dynamical history. This paper reports the results from a new observational survey that searches for ETs near the L5 Lagrange point of the Earth-Sun system. The survey uses the DECam instrument on the Blanco 4 meter telescope. Although no new objects have been detected, this observational program provides the strongest constraints to date on the population of ETs.

2.2.1 Significance of Earth Trojans

Despite their relative proximity to Earth compared to other astronomical objects, the Earth Trojan population is poorly understood. ETs are asteroids that orbit near the Earth-Sun L4 or L5 Lagrange points (60° ahead or behind the Earth, respectively). Trojan asteroids have been discovered accompanying other planets, including Venus, Mars, Jupiter, Uranus, and Neptune (*de la Fuente Marcos and de la Fuente Marcos*, 2014; *Ivezić et al.*, 2001; *Morbidelli et al.*, 2005; *Yoshida and Terai*, 2017; *Almeida et al.*, 2009; *Lin et al.*, 2019; *de la Fuente Marcos and de la Fuente Marcos*, 2017). In contrast, only one ET has been found, 2010 TK_7, which was discovered serendipitously by WISE (*Connors et al.*, 2011).

Characterization of this population is important as ETs can give a unique insight into our Solar System. Numerical simulations have shown that ETs can have orbits near the L4 or L5 points that are stable on time scales of order the current age of the Earth (*Ćuk et al.*, 2012; *Malhotra and Jeongahn*, 2011; *Tabachnik and Evans*, 2003; *Marzari and Scholl*, 2013). As a result, the objects in this population could be undisturbed remnants from our primordial protoplanetary disk. In principle, the distribution of ETs can thus be used to constrain Solar System formation models. The chemical composition of these bodies could also provide insight into the properties of the primordial material from which our Solar System formed.

ETs have also been studied as potential lunar impactors. In particular, there appears to be an asymmetry of rayed lunar craters on the leading and trailing sides of the moon (*Morota and Furumoto*, 2003). Both *Gallant et al.* (2009) and *Ito and Malhotra* (2010) used numerical simulations to assess whether this asymmetry could be due to impacts of Near Earth Asteroids (NEAs). *Gallant et al.* (2009) concluded that, within the uncertainties of their simulations and of the observational data, the known population of NEAs were sufficient to account for the observed crater asymmetry, whereas *Ito and Malhotra* (2010) found that the known NEA population could

only account for $\sim 50\%$ of the asymmetry. An unobserved population of NEAs with very small velocities relative to the moon, like Earth co-orbitals, has been suggested and studied as a solution to this discrepancy (*Ito and Malhotra*, 2010; *JeongAhn and Malhotra*, 2010).

However, due to the lack of observational constraints on the ET population, the viability of ETs as this missing impactor population has been investigated only through theoretical models of the population, which may not represent the true distribution of co-orbitals. Detections of the ET populations in both the L4 and L5 Lagrange points — or robust upper limits — will provide important constraints on planet formation theories, which consider both the dynamical evolution and the physical properties of rocky Solar System objects.

2.2.2 An Unstable Earth Trojan: 2010 TK_7

ETs are a particularly difficult population to observe; the L4 and L5 points are always at low solar elongations as observed from the Earth ($\sim 60^\circ$ ahead or behind the Sun respectively), meaning they can only be observed around dawn or dusk when the sky is still relatively bright. Moreover, due to the geometries of their orbits, ETs are never observed at opposition, and their larger phase angles make them even fainter and harder to detect.

These challenges may be part of the reason that only one ET, 2010 TK_7, has been observed to date (*Connors et al.*, 2011). However, the orbit of this object is not consistent with primordial ETs, which are expected to be long-term stable librators near L4 or L5. In particular, 2010 TK_7 has a large amplitude tadpole orbit, librating between Earth and L3 (the Lagrange point behind the Sun), rather than remaining near L4 (*Connors et al.*, 2011; *Dvorak et al.*, 2012). We consider such orbits distinct from primordial ETs, though it is possible for these orbits to also be stable on the order of $\sim$Myrs (*Marzari and Scholl*, 2013; *Dvorak et al.*, 2012).

Numerical integrations indicate that 2010 TK_7 has a highly chaotic and short-lived orbit. Estimated lifetimes vary from ∼7000 years (*Connors et al.*, 2011) to about ∼0.25 Myrs (*Dvorak et al.*, 2012). Taking into account the Yarkovsky effect, *Zhou et al.* (2018) also concluded that 2010 TK_7 is too small to maintain a long-term stable orbit. As a result, this object is most likely an asteroid that was temporarily captured as an Earth co-orbital, rather than a primordial ET.

2.2.3 Previous ET Searches

There have been a few dedicated searches for ETs. The most recent searches were a ground-based survey for L5 ETs (*Whiteley and Tholen*, 1998, W&T98), an OSIRIS-REx search as the spacecraft flew past the L4 point on its way to the asteroid Bennu (*Cambioni et al.*, 2018, O-R18), and a search made by the Hayabusa2 spacecraft as it flew past the L5 point on its way to Ryugu (*Yoshikawa et al.*, 2018). None of these surveys found any other Earth Trojans.

An upper limit calculation from the Hayabusa results has not yet been published (*Yoshikawa et al.*, 2018). *Whiteley and Tholen* (1998) placed an upper limit on the ET population of ∼3 objects per square degree to R=22.8. *Cambioni et al.* (2018) placed on upper limit on the population of 73 ± 22 objects ∼210 m (S-type asteroids) to ∼470 m (C-type asteroids) in size. For comparison, they also applied their method to the *Whiteley and Tholen* (1998) survey and found an upper limit of 194 ± 116 objects at the OSIRIS-REx limiting magnitude (*Cambioni et al.*, 2018). These limits imply that there could still be tens to hundreds of undiscovered ETs. Moreover, the *Whiteley and Tholen* (1998) search at L5 only covered a 0.35 sq. deg. area near L5. From these relatively large upper limits and limited survey coverage, it is clear that the ET population is far from being completely, or even sufficiently, characterized.

In this paper we present the results of a new survey directed at the Sun-Earth L5 point with DECam on the Blanco 4m telescope. In Section 2.3, we provide a

description of the observations that make up our survey. In Section 2.4, we provide a description of the pipeline to reduce the data, extract moving objects, and create a catalog of ET candidates. In Section 2.5, we present all of the moving objects found by our survey. In Section 2.6, we present the upper limits on the ET population derived from the results of our survey. In Section 2.7, we discuss our findings and their implications.

2.3 DECam Survey

Our survey utilized the VR filter on the Dark Energy Camera (DECam, *Flaugher et al.*, 2015), which is a prime focus imager on the 4-meter Blanco telescope at the Cerro Tololo Inter-American Observatory. The VR filter is the widest filter on DECam, making it easier to detect faint ETs. The sky coverage for this survey is shown in Fig. 2.1. We observed shortly after sunset on the night of June 16, 2018, covering an area near Earth's L5.

DECam has 61 active CCD chips that cover 3 sq. deg. on the sky. As shown in Fig. 2.1, our survey consisted of 8 fields, covering an area of 24 sq. deg. ($\sim$ 70 times larger than Whiteley & Tholen, 1998). See Table A in the Appendix for complete list of exposures. Since stable ETs may have libration amplitudes of up to 30° but low inclinations, the fields were arranged to proceed eastward from the L5 point within roughly $\pm 2°$ of the ecliptic.

Two consecutive 15 second exposure were taken of each field, and this sequence was repeated 4 times at approximately 15-minute intervals. The two short exposures were used to identify objects that were transient over $\sim$ 30 seconds of readout time between exposures. Since ETs are expected to have a rate of motion across the sky of $\sim$ 1 deg/day (see Sec. 2.4.2.5), an exposure time of 15 seconds was chosen to avoid trailing of these objects in the individual images, which would make these objects harder to detect in the individual exposures. The subsequent visits were used to

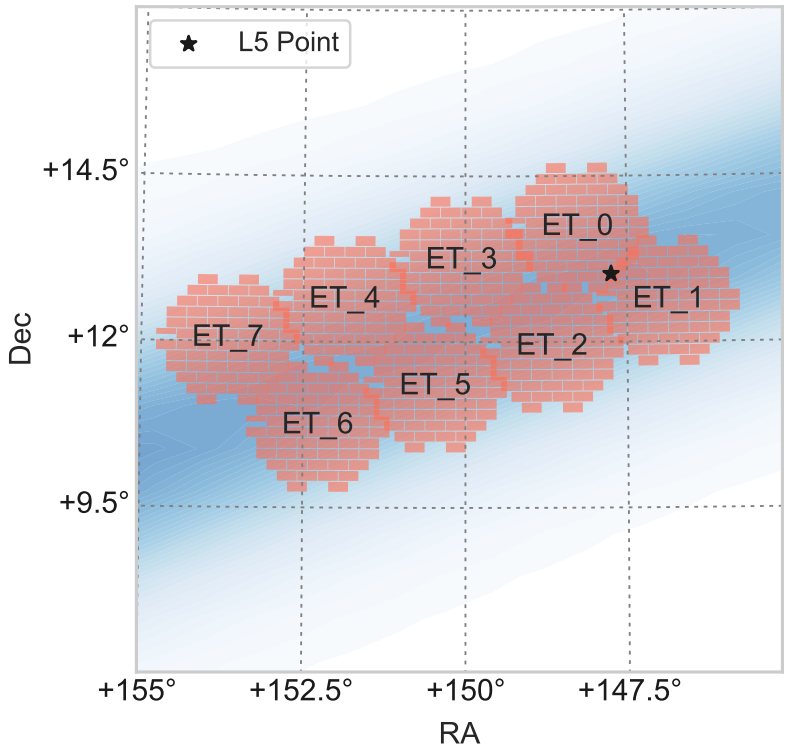

Figure 2.1: The area covered by our survey. The star marks the location of the L5 point. The relative density of synthetic ET objects (see Sec. 2.6.1) is shown in the background in blue. Each rectangle corresponds to a chip in one of the 8 DECam fields. In total, these fields cover $\sim$ 24 sq. deg. near L5.

track the motion of the object and identify a tracklet for a potential Solar System object.

This sampling strategy did *not* allow us to fit an orbit to detected Solar System objects, because the observational arcs are too short. Therefore, we were not able to dynamically classify any of the objects found in our survey (as was done in *Ivezić et al.*, 2001). Any new objects found in this survey would require additional followup to be classified as ETs, but they could be identified as ET candidates due to their characteristic rate of motion across the sky of $\sim$1 deg./day (see Sec. 2.4.2.5).

2.4 Reduction Pipeline

We reduced the survey data and extracted Solar System objects, in particular ETs, by the following steps:

1. DECam Community Pipeline (*Valdes et al.*, 2014): for basic data reduction
2. *Source Extractor* (*Bertin and Arnouts*, 1996): for source identification
3. *Bullseye*: a pipeline we developed for this project to link transient sources
4. Verification by eye/catalog creation: for removal of false positives

2.4.1 Source Extractor

We used Source Extractor (SE) to identify sources in each of the exposures. Table 2.1 shows the SE parameters used for this analysis. The DETECT_THRESH parameter was set to 1σ; it was set this low for completeness at very faint objects, as many anomalous sources could be identified/filtered out (see Sec. 2.4.2.2, 2.4.2.4).

In particular, after running SE, we remove any sources with a center pixel flagged as bad by the DECam Community Pipeline. This pipeline flags bad/compromised pixels (e.g. known detector defects), saturated pixels, bleed trails, and transient artifacts (*Valdes et al.*, 2014). We do not use the transient flags in order to ensure that we are not losing transient Solar System objects. This step removes hundreds of blatantly bad/compromised sources from each chip.

2.4.2 Bullseye

Once the SE catalogs for each exposure were created, we linked these sources together to identify transient Solar System objects, particularly ETs. Based on the cadence of our survey, the best possible detection of a Solar System object would be 8 individual detections (one for each exposure) in a nearly straight line, due to the short

Table 2.1: Source Extractor Parameters. The filter called "all-ground" is a 3x3 convolution mask with FWHM = 2 pixels.

Extraction Parameters	
DETECT_TYPE	CCD
DETECT_MINAREA	6
DETECT_THRESH	1.0
ANALYSIS_THRESH	1.0
FILTER	Y
FILTER_NAME	all-ground
DEBLEND_NTHRESH	32
DEBLEND_MINCONT	0.005
CLEAN	N
WEIGHTing Parameters	
WEIGHT_TYPE	MAP_VAR
Background Parameters	
BACK_TYPE	AUTO
BACK_VALUE	0.0
BACK_SIZE	256
BACK_FILTERSIZE	3

arc of these observations ($\sim$ 1 hour). We created *Bullseye* to identify sets of transient detections that fit to a line and have a speed consistent with nearby Solar System objects (see Table 2.2), and to flag those whose speed is consistent with ETs. This process is run for each survey field, chip by chip. We do not attempt to link objects that crossed chip boundaries; from our recovery rate of known Solar System objects, we determined that chip-crossing objects are a small fraction of the population and some may still have linkable observations in at least one of the chips. The steps in this pipeline are described in more detail in the following sections.

2.4.2.1 Identify Transient Sources

The pipeline starts by identifying sources from the SE catalogs that are transient between exposures. Using astropy's `match_to_catalog` (*Astropy Collaboration et al.*, 2013, 2018), we compare the catalog of the sources between each of the sets of two exposures. If the distance to the nearest source between the two catalogs is more

Table 2.2: Bullseye Parameters. R is the stationary source radius (measured by SE). See Sec. 2.4.2 for discussion of these parameters.

Transient Identification	
Transient metric	>0.25”
Stationary metric	<0.5”
Min. detections for stationary	3
Bright Stationary metric	<2”
Min. detections for bright stationary	7
Transient ring min. radius	R
Transient ring max. radius	3.5R
Transient ring min. density	0.035 sources/arcsec^2
Linking	
Min. detections for link	5
Min. speed	0.1 deg./day
Max. speed	2.0 deg./day
Cluster eps	0.05
Min samples for cluster	4
Flagging ET Candidates	
Min. speed	0.75 deg./day
Max. speed	1.25 deg./day

than the transient metric (i.e. there is no source at the same position in the next exposure, see Table 2.2), the source is considered to be transient. This comparison must actually be done both ways (i.e. compare the first catalog to the second and vice versa) because it is possible for a transient source to only show up in the second of the two catalogs due to differences in observing conditions between exposures. Only objects that are transient between the sets of two exposures will continue on to the next step.

2.4.2.2 Cut Stationary Sources

Stationary objects (sources with the same position in a set of two exposures) should not be included in the transient catalog after the previous step. However, stationary sources with inconsistent astrometry or faint stationary sources which were not detected in one of the two exposures in a set could have been erroneously

included in the transient catalog and needed to be removed. We use astropy's `search_around_sky` method (*Astropy Collaboration et al.*, 2013, 2018) to compare objects in the transient catalog from the previous step to an SE catalog which includes the source detections in all of the exposures for a field. If a transient object's position matches to too many objects in the full SE catalog within the search radius (see Table 2.2), it will be cut. In other words, this step removes objects which have the same position in 3 out of the 8 exposures. To avoid cutting true transients, we choose parameters for these cuts that are more lenient to avoid removing actual transients from our search. We also removed rings of scattered light around stationary sources that meet the "bright stationary" criteria in Table 2.2.

2.4.2.3 Connect Transients

After cuts to the transient catalog, we link these detections between exposures together to identify potential Solar System objects. Detections are linked if their motion between exposures is consistent with the motion of a Solar System object. In particular, we assumed a min and max speed typical of nearby Solar System objects, primarily main belt asteroids (see Table 2.2), but did not assume a direction of motion. There are classes of Solar System objects that would not make our speed cut, such as very nearby asteroids or distant, outer Solar System objects. However, neither of these populations are the focus of this search, and the expected ET speed of 1 deg./day is well within our search space.

With a min and max speed but no restriction on direction, the search space for another detection is an annulus. Therefore, for each transient detection (the "anchor" transient), we used `search_around_sky` to identify other transient objects that fall within that search annulus in each of the subsequent exposures. Anchor transients can come from any of the exposures to account for sources near our limiting magnitude that were not detected in the first exposure and objects near the edge of the chip. At

the end of this step, we have a list of transient sources that are linked to subsequent detections that would be consistent with the rate of motion of Solar System objects.

2.4.2.4 Fit Lines of Motion

If all of the detections connected to an anchor transient from the previous step were of the same Solar System object, we would expect them to have the same velocity at each observation. Here, we define the velocity as the object's rate of motion across the sky in deg./day (speed) and position angle (direction) as measured with respect to the anchor point. Therefore, all of these transient detections need to have similar velocities in order to identify them as the same object.

To group these detections by velocity, we used `DBSCAN` ("Density-Based Spatial Clustering of Applications with Noise") from the *scikit-learn* package.[1] This method is able to identify regions with a high density of points in Cartesian space; specifically, a cluster must have at least some minimum number of points within a certain distance (see "eps" parameter in Table 2.2). However, the velocities of our transient detections are in polar coordinates (a speed with an angular direction). Therefore, we converted the speed and position angle into a Cartesian space to then identify detections with clustered velocities. If this cluster contained at least 5 detections from different exposures of the linked object, we add it to our transient object catalog. Therefore, in the end we have a final set of detections that are linked together as a candidate tracklet.

2.4.2.5 Flag ETs

Due to the short arcs of our investigations, it was not possible to fit orbits to our detections, which would be required to definitively classify an object as an ET. However, due to their relatively consistent position with respect to the Earth and

[1] https://scikit-learn.org/stable/index.html

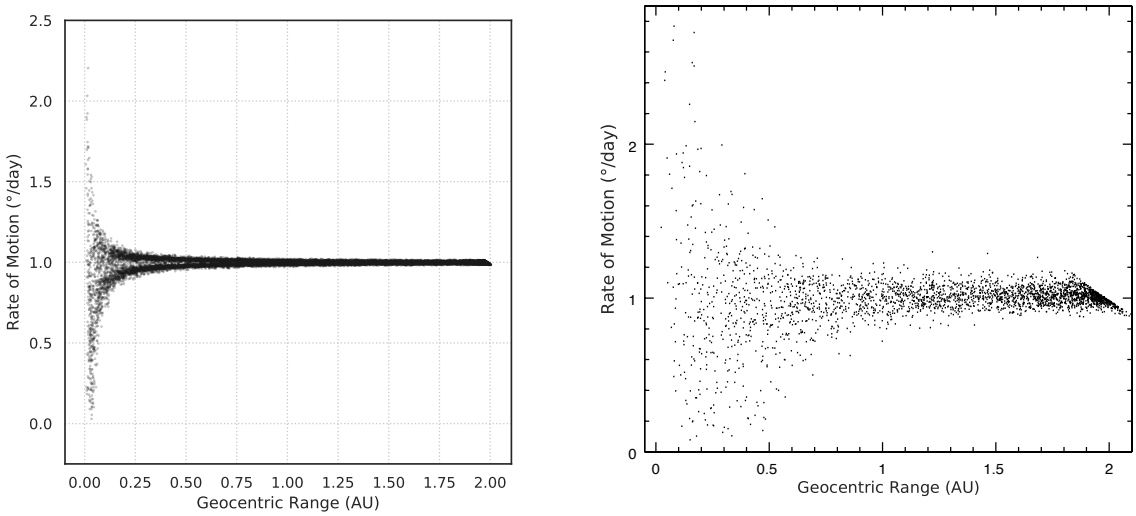

Figure 2.2: *Left*: The rate of motion on the sky for the "Strict" set of synthetic ETs (see Sec. 2.6.1). Other than at small geocentric ranges ($\lesssim$ 0.1 AU), the ETs have a well constrained speed of 1 deg./day. *Right*: Same as *Top* but for the "Jupiter Trojan" set of synthetic ETs (synthetic ETs generated based on observations of Jupiter Trojans; see Sec. 2.6.1). These objects also have a well constrained speed of $\sim$1 deg./day for geocentric ranges $>$0.5 AU. There is more dispersion in the speed, but this is expected as this set of ETs was generated based off of observations of Jupiter Trojans.

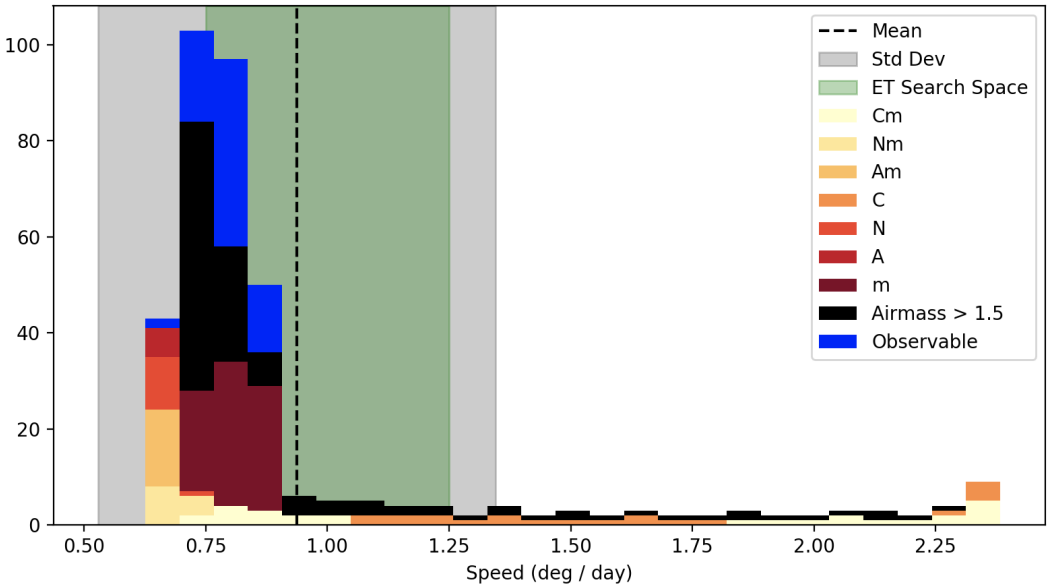

Figure 2.3: This figure shows the predicted rates of motion for 2010 TK_7 on each night in 2018 (taken from JPL HORIZONS: ssd.jpl.nasa.gov/?horizons). The dashed line shows the mean speed and the grey region depicts the standard deviation. The green region represents the speeds for which an object would be flagged as an ET by our pipeline. Nights on which we consider 2010 TK_7 to be observable are plotted in blue. The other colors represent nights on which observing 2010 TK_7 would be unfavorable according to the Solar Presence and Lunar Presence parameters from JPL HORIZONS. In particular, "C" is civil twilight/dawn, "N" is nautical twilight/dawn, "A" is astronomical twilight/dawn, and "m" is refracted upper-limb of Moon on or above apparent horizon. Although the standard deviation region extends beyond our assumptions for ET speed, the mean is well with our search space. In fact, most of the nights beyond our speed cuts are ones for which 2010 TK_7 is not observable.

Sun, simulated ETs (see Sec. 2.6.1) have a distinct rate of motion on the sky of 1 deg./day, except at small geocentric ranges (see Fig. 2.2). Therefore, any previously undiscovered object in our catalog that has a mean speed between 0.75 and 1.25 deg./day is considered an ET candidate in our survey.

However, the only known ET, 2010 TK_7, often has rates of motion that are not consistent with this assumption (see Fig. 2.3). While technically its mean rate of motion is nearly 1 deg./day, it is clear that this object most often moves at ~ 0.75 deg./day. Fortunately, this slower rate of motion often still falls within our speed assumption. Moreover, there are many evenings when 2010 TK_7 would not have actually been detectable due to high air mass, solar elongation, moon phase, etc. For a large portion of the evenings where 2010 TK_7 would have been detectable by our survey (if it had been directed towards L4), 2010 TK_7 would still have been flagged as an ET by our pipeline (if it had been detected). Regardless, 2010 TK_7 does not have an orbit that is representative of primordial ETs, and it should not be considered as a particularly strong or valid test for this pipeline. Thus, we consider our assumption of ET candidates having a speed between 0.75 to 1.25 deg./day to be reasonable since it is consistent with simulated ET populations and roughly valid for 2010 TK_7 (a notably atypical ET).

However, an object that has a 1 deg./day rate of motion is *not* guaranteed to be an ET. There are other populations of asteroids that can have similar rates of motion and could happen to overlap with the L5 point (see Sec. 2.5.3). Again, additional observations of a candidate would be required to actually constrain its orbit and classify it as an ET.

2.4.3 Verification by Eye/Catalog Creation

Despite the cuts on bad detections, transients, and links, false positives were still found by the *Bullseye* code. Therefore, linked objects were reviewed by hand in order

to remove obvious false positives from our catalog. Such objects included detections of stationary objects with very variable astrometry between exposures, detections in the scattered light rings around very bright objects, detections along diffraction spikes, and detections along detector defects. Out of the 7676 candidate objects identified by the pipeline, 6059 were determined to be false positives. However, many of these anomalous objects were linked to large rings of scattered light around very bright or detector defects making them easy to identify and remove from our catalog.

While reviewing the candidate objects, it was also convenient to look for objects that were identified by SE and correspond to previously known Solar System objects but were not linked by the pipeline (i.e. non-recovered objects). Many of these objects were observed to be in crowded field, confused with a bright star, or fell in a chip gap.

2.5 Detected Objects

2.5.1 Previously Known Objects

To determine which objects had been previously discovered, we compared our catalog to the SkyBoT database (*Berthier et al.*, 2006). In total, there were 4126 minor bodies coincident with our survey area, and we recovered detections of 1546 known Solar System objects ($\sim$40%). The majority of these objects were main belt asteroids. All of these detections have been submitted to the Minor Planet Center.[2]

Figure 2.4 shows our recovery of known objects as a function of their V-band magnitude as predicted by SkyBoT. As expected, our recovery rates drop off at fainter magnitudes. In particular, the recovery rates are $\gtrsim 50\%$ for $V \lesssim 22$, and they drop quickly to 0% beyond this point. This implies that overall limiting magnitude for our survey is roughly $V = 22$. However, reducing this limit to a single number obfuscates

[2] minorplanetcenter.net

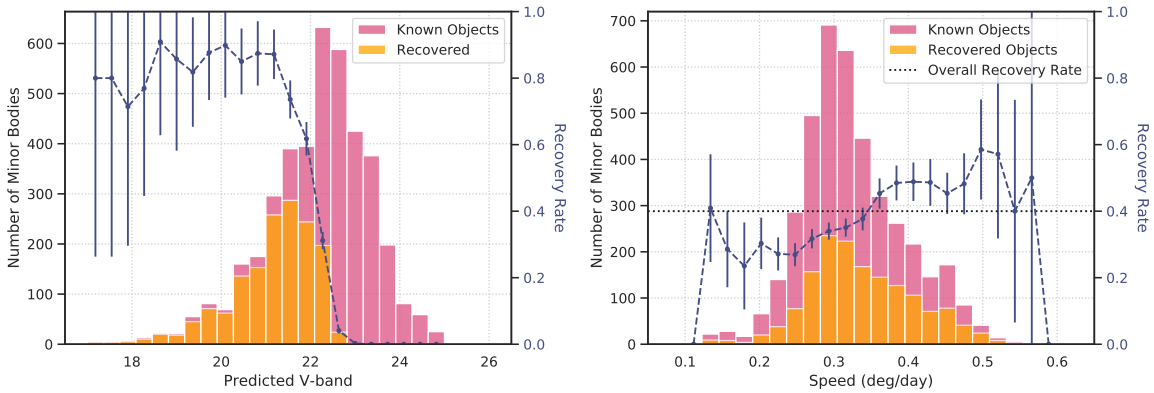

Figure 2.4: *Left*: Recovery rates for previously known minor bodies as a function of predicted V band magnitude. The known minor bodies that coincided with our survey area are shown in pink, and those which were detected and linked by our pipeline are shown in yellow. The recovery rate in each bin, with Poisson errors, are shown as a blue dotted line. *Right*: This plot shows our recovery rates for previously known minor bodies as a function of predicted total sky motion. Colors are the same as *Top*. The overall recovery rate of ∼40% is shown as a black dotted line. The recovery rates across all of these speeds are generally consistent with this overall rate, but recovery rates are lower for slower speeds.

the different detection thresholds in each image due to differences in chips, weather conditions, etc. This limiting magnitude also explains why the overall recovery rate for our survey was only 40% as a majority of the previously known objects were not detectable in our survey.

Fig. 2.4 also shows our recovery rates as a function of their rate of motion as predicted by SkyBoT. The recovery rates in each speed bin are roughly consistent with the overall recovery rate. Therefore, we conclude we are not especially more/less sensitive to detecting objects moving at a particular speed. However, these recovery rates are not entirely independent of speed; slow moving rates are somewhat lower than for fast moving objects. This discrepancy is likely due to the fact that slower moving objects are more likely to be flagged as stationary. Since ETs move at a speed of ~ 1 deg. / day, they were very unlikely to be flagged as stationary in our dataset and, as is shown in Fig. 2.4 we may even be more efficient such objects.

Moreover, due to the nature of our survey, it is likely that we observed these objects at much higher phase angles than their discovery. Therefore, we expect our recovery rate and limiting absolute magnitude of known asteroids to be lower than an identical survey of objects at lower phase angles.

2.5.2 New Objects

Table 2.3 lists all of the Solar System objects identified by our pipeline that did not match to positions of known asteroids (a total of 27 new objects). Most importantly, none of these objects have a rate of motion of ~ 1 deg./day. Rather, they are consistent with the rates we observed for main belt asteroids. Therefore, by our definition, we did not find any ET candidates in our survey. However, due to the short arcs of our dataset, we cannot determine the orbits of these new objects or their classification. These detections have been submitted to the Minor Planet Center (MPC) so that they may be linked to an orbit in the future.

Table 2.3: New Objects. The individual observations for all of these objects have been submitted to the *Minor Planet Center*. Columns: (1) Our designation for this object. The first number is the field and the second number is the chip the object was found in. The third number is a unique id; (2) Inferred V-band magnitude for the object. See Sec. 2.6.1 for a description of how the V-band magnitudes were calculated; (3) Rate of sky motion measured for the object (deg./day). The rate of motion is averaged over all of the detections; (4) Position angle measured for the object (deg.). The P.A. is averaged over all of the detections; (5) Number of detections of the object.

Designation	m_V	Rate of Motion	P.A.	Num.
1_55_5	23.1	0.29	129.3	6
2_37_0	22.5	0.37	115.3	6
2_51_2	22.6	0.40	99.9	7
2_54_9	22.8	0.37	113.3	5
3_21_2	23.0	0.49	110.9	6
3_34_3	23.5	1.76	264.3	5
4_15_13	22.6	0.15	122.3	7
4_36_0	22.8	0.32	113.1	8
4_39_6	23.4	0.27	99.7	5
4_45_0	22.9	0.49	107.9	7
4_56_5	23.3	0.14	129.1	5
5_16_2	22.8	0.46	107.5	7
5_32_1	23.2	0.32	102.5	6
6_24_5	23.3	0.36	115.7	6
6_34_0	22.9	0.32	121.5	8
6_58_2	22.4	0.36	153.8	7
7_3_6	23.3	0.42	107.9	5
7_4_3	23.1	0.30	89.1	6
7_15_1	23.0	0.32	130.9	6
7_18_3	22.8	0.16	90.2	8
7_19_2	22.9	0.36	105.3	7
7_19_3	22.8	0.49	106.3	6
7_20_3	23.2	0.38	113.9	6
7_27_2	22.6	0.33	109.5	8
7_33_5	23.2	0.39	114.3	5
7_37_0	22.1	0.26	104.0	8
7_50_1	22.6	0.33	129.3	7

Table 2.4: Previously Known Objects Flagged as ETs. The individual observations for all of these objects have been submitted to the *Minor Planet Center*. Columns: (1) Object Designation; (2) Orbit type taken from *SkyBoT* (*Berthier et al.*, 2006); (3) Predicted V-band magnitude (taken from *SkyBoT*); (4) Rate of sky motion measured for the object (deg./day). The rate of motion is averaged over all of the detections; (5) Position angle measured for the object (deg.). The P.A. is averaged over all of the detections; (6) Number of detections of the object.

Designation	Orbit Type	m_V	Rate of Motion	P.A.	Num. Detections
2003 HF2	NEA:Apollo	21.9	1.08	110.5	6
2006 JF42	NEA:Aten	21.0	1.17	124.1	7

2.5.3 Aten & Apollo Asteroids

While our pipeline did not flag any new objects as ET candidates, there were a few previously known objects that were flagged because they happened to have a rate of motion of $\sim$ 1 deg/day (see Table 2.4). One of these objects was an Apollo asteroid while the other was an Aten. We draw attention to these objects specifically because they provided a serendipitous test of our pipeline while also highlighting the limitations of our method.

First, Apollo and Aten asteroids both have Earth crossing orbits, with q >1 AU and q <1 AU respectively. If these asteroids were to cross the Earth's orbit at a point near the L4 or L5 points with a rate of motion of $\sim$ 1 deg./day they would be indistinguishable from ET candidates in our survey. Fig. 2.5 shows the orbit of the flagged Aten asteroid, which indeed crosses the Earth's orbit near the L5 point and has a rate of motion of 1.17 deg./day. The orbit for the flagged Apollo asteroid is similar. The fact that these distinct populations would be indistinguishable in our observations highlights the fact that our method can *not* definitively classify transient objects as ETs.

However, it is still significant that these objects were flagged. Since these asteroids behave exactly as we expect ETs would in our dataset and they were properly

detected and flagged, this implies that our pipeline was capable of finding ETs as well. Certainly, these objects are not a robust test of the capability of the pipeline, but they did allow for a test on real, known objects. The only known ET that we could have otherwise tested on (2010 TK_7) is at the L4 point, which is not within our survey area.

2.6 Upper Limits on ET Population

To calculate an upper limit on the ET population, we generated a population of simulated ETs, injected them into our data set, ran these images through the pipeline as described in Section 2.4, and then measured our recovery rate for these objects. We then used this recovery rate to place an upper limit on the ET population.

2.6.1 Synthetic ETs

To generate synthetic ET populations, we adopt the restricted three body model of Sun, Earth and a test particle. We generated two different synthetic ET sets: a "Strict" ET set and a "Jupiter Trojan" ET set. Both sets were used to predict the rate of motion for ETs (see Sec. 2.4.2.5), but only objects from the Strict set were injected into our images.

2.6.1.1 Strict ET Set

We generated a sample of $N = 10^6$ Earth-like test particle orbits, with heliocentric osculating orbital elements as follows: semi-major axes uniform random in the range $0.99 - 1.01$ AU, eccentricities uniform random in $0 - 0.1$, ecliptic inclinations uniform random in $0 - 0.1$ radians; the angular elements (longitude of ascending node, argument of perihelion and true anomaly) uniform random values in the range $0 - 2\pi$. We computed the position and velocity vectors, $\mathbf{r}$ and $\mathbf{v}$, in the barycentric frame, and

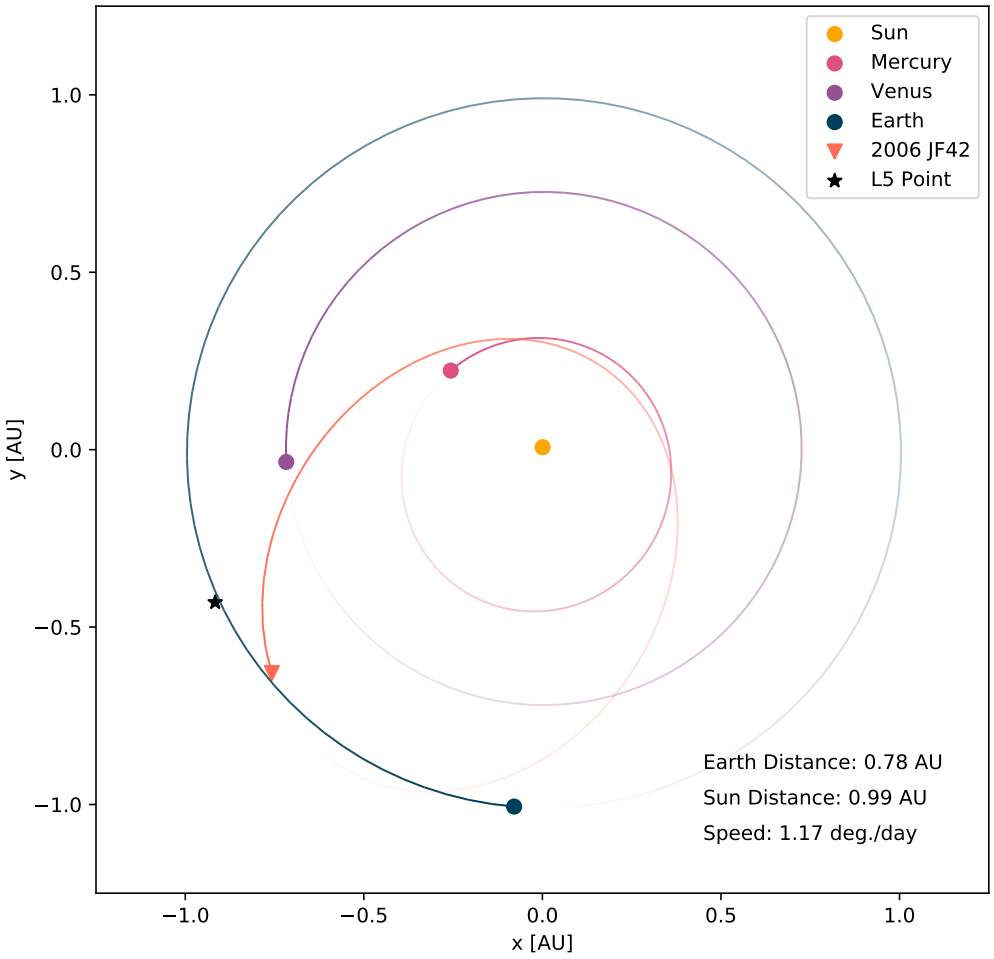

Figure 2.5: This figure shows the orbit of the Aten asteroid detected in our survey, 2006 JF_{42}. At the time of our observations, this asteroid was near the L5 point. With a distance to the Earth of 0.78 AU and a distance to the Sun of 0.99 AU, this object had a rate of motion of 1.17 deg./day, causing it to be misidentified as an ET candidate by our pipeline. This figure was produced using REBOUND (*Rein and Liu*, 2011).

the Jacobi integral for these particles,

$$C = 2(\frac{1-\mu)}{|\mathbf{r}-\mathbf{r}_\odot|} + \frac{\mu}{|\mathbf{r}-\mathbf{r}_\oplus|}) + 2\hat{\mathbf{n}}\cdot(\mathbf{r}\times\mathbf{v}) - v^2 \tag{2.1}$$

where μ is Earth's mass as a fraction of the total mass (Earth and Sun) and $\hat{\mathbf{n}}$ is the unit vector normal to the ecliptic. We then selected the subset of those particles having Jacobi integral in the range $3-\mu$ to $3+\mu$, in standard units for the restricted three body problem; this range of Jacobi integral covers the L4 and L5 libration zone. The synthetic L4 and L5 ETs were then selected as the subset having instantaneous positions within 30 degrees of heliocentric ecliptic longitude of the L4 point and L5 point, respectively. This produced a sample of 3797 L4 and 3726 L5 synthetic ETs.

2.6.1.2 Jupiter Trojan ET Set

We started with the full dataset of minor planet orbital data from the Minor Planet Center (on Nov 27, 2018). We selected the observationally complete set of Jupiter Trojans from this set, which we defined as those objects of absolute magnitude H $<$ 13.5 and semi-major axis in the range $5.0-5.4$ AU (2844 object in total). To generate ET orbits, we made three changes to the orbital data set of Jupiter Trojans. First, we rescaled the semi-major axes of the particles to Earth's,

$$a_{ET} = a_\oplus + (a - a_{Jupiter})(R_{H,\oplus}/R_{H,Jupiter}) \tag{2.2}$$

where $R_{H,\oplus}, R_{H,Jupiter}$ are the Hill radii of Earth and Jupiter, respectively. Second, we computed the orbital plane orientation of each Jupiter Trojan relative to Jupiter's osculating orbital plane and re-assigned it to be relative to Earth's osculating orbital plane. Third, we assigned the mean anomaly of ETs as follows:

$$M_{ET} = M + \lambda_\oplus - \lambda_{Jupiter} \tag{2.3}$$

where $\lambda_{\oplus}, \lambda_{Jupiter}$ are the mean longitudes of Earth and Jupiter at the epoch of the Minor Planet Center's data, and M is the mean anomaly of a Jupiter Trojan. These changes produce a population of synthetic ET orbits that has the same dispersion in semi-major axis, eccentricity and inclination as the Jupiter Trojans, but relative to Earth's orbit and scaled to the size of Earth's Trojan regions.

2.6.2 Injection of Synthetic ETs

To estimate our recovery rate for ETs, we drew from the Strict synthetic ET set and injected corresponding sources into our images.[1] To most accurately simulate the ET population in our images, the synthetic sources must be at realistic positions, follow a reasonable absolute magnitude (H) and physical size distribution, and have the correct amount of injected counts for the corresponding magnitude.

The synthetic sources were injected as Gaussian point sources into the image array count by count. Note, assuming an albedo of 0.15, we expect ETs to be less than about 1 km in size; such objects would not be resolved in our dataset, so we can safely model them as point sources. Each synthetic source is generated to have the same FWHM as derived by the DECam Community pipeline for each image. In particular, the width σ of a Gaussian distribution can be derived from the FWHM via the relation

$$FWHM = 2\sqrt{2\ln 2}\sigma \tag{2.4}$$

Each count was added at a random x, y shift from the center of the object generated from this distribution. This method worked well for many sources, but not all; very bright sources often had a much larger angular size than the inferred FWHM (see Fig. 2.6).

To calculate the sky positions of our synthetic ETs, we used the generated heliocentric osculating orbital elements (see Sec. 2.6.1) and *PyEphem*[3] to calculate the

[3]https://rhodesmill.org/pyephem/

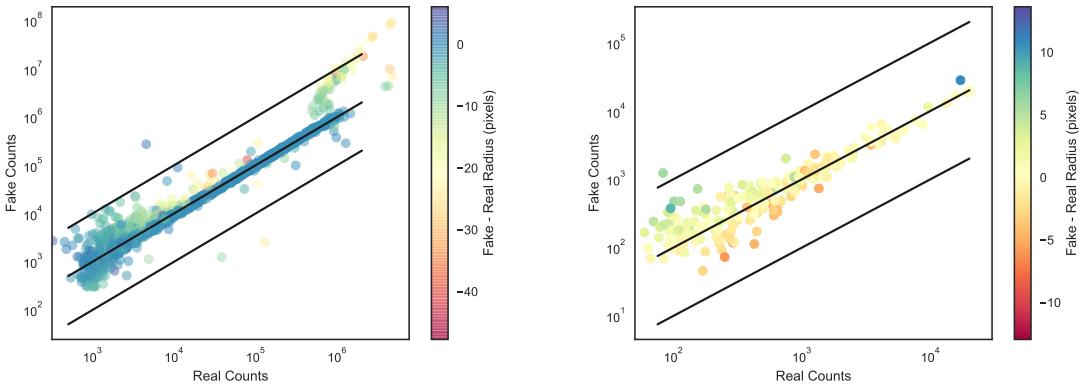

Figure 2.6: *Left*: This figure compares the number of counts measured by SE for Solar-type stars in Field 0 to the number of counts for a fake source of the same V-band magnitude. In general, the points lie well along the one-to-one line and the radii of the fake and real sources are nearly the same. Not surprisingly, there is more dispersion from this line at the faint end, but the points still have the same number of counts within an order of magnitude. There is also a clear overabundance of fake counts for the brightest objects, which is likely due to the saturation limit. *Right*: Same as *Top* but for known Solar System objects in Field 0. These points fall well along the one-to-one line and the radii of the real sources as compared to the fake ones are still nearly the same. Based on this plot, we conclude that our fake sources are consistent with our observations of known Solar System objects in our survey.

predicted RA, Dec at the time of each of our observations. Our observing location at Cerro Tololo Inter-American Observatory (longitude: -70.80°, latitude: -30.17°, elevation: 2207 m) was taken into account for these calculations.

For the H distribution, we use one similar to that of NEOs/asteroids:

$$N(< H) = A * 10^{\alpha H} \tag{2.5}$$

where H is the absolute magnitude, A is a normalization factor, and α is a slope parameter. We draw uniformly from a range of typical α = 0.46 - 0.54 (*Jedicke and Metcalfe*, 1998; *Bottke et al.*, 2000; *Harris and D'Abramo*, 2015; *JeongAhn and Malhotra*, 2015). We set A such that N(<H_{max}) is equal to the total number of synthetic ETs. Of course, this means that we need to pick an H_{max}; we defined our distribution to have H_{min} = 15 and H_{max} = 20.5. Our choice of H_{min} is somewhat arbitrary as very bright objects will be very rare in this distribution. Based on our recovery of previously known Solar System objects (see Sec. 2.5.1), we estimated our limiting magnitude to be $\sim$ 21.5 in V-band, but we still recovered known objects at V $\sim$ 22.5 (see Sec. 2.5.1). This magnitude corresponds to H $\sim$ 20.4. Therefore, we inject synthetic ETs up to H_{max} = 20.5.

To generate a magnitude for each specific object, we cannot use Eq. 2.5 directly as it is a cumulative distribution. Instead, we normalize Eq. 2.5 by A, such that N(<H_{max}) = 1 and then use this distribution as a probability distribution. Fig. 2.7 demonstrates that this method leads to magnitudes that are consistent with the theoretical distribution (i.e. the cumulative distribution of our randomly drawn magnitudes matches the theoretical distribution well). Therefore, we conclude that this method is sufficient to generate synthetic ETs with an accurate distribution.

Since each object's apparent magnitude is highly dependent on its location in its orbit, we use the functionality in *PyEphem* to calculate an apparent magnitude for

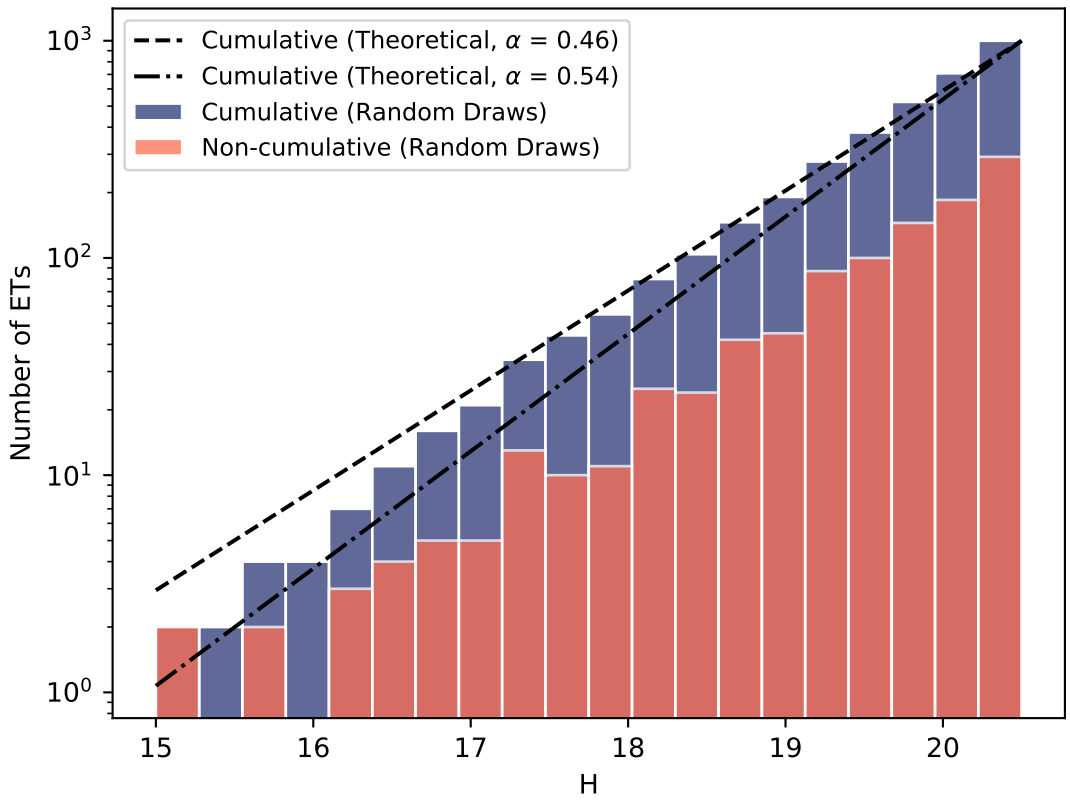

Figure 2.7: This figure compares our theoretical H distribution of ETs (Eq. 2.5) to the distribution generated by random draws from Eq. 2.5 normalized by the total number of fake ETs (in the case of this figure, 10^3). The black dashed and dot-dashed lines represent the theoretical H distribution with $\alpha = 0.46$ and 0.54, respectively. The blue and red histograms represent the cumulative and non-cumulative H distributions, respectively, which were generated for the simulated ETs (see Sec. 2.6.2 for description). Due to the random nature of this method, these distributions are similar to those used for the sources that were actually injected into our images to asses our recovery rate, but they are not exactly the same. Most importantly, the simulated cumulative distribution lies well between the two theoretical distributions. We therefore conclude that the injected ETs have an H (and thus size) distribution consistent with what we would expect theoretically.

the synthetic ETs at the time of each observation. To convert these magnitudes into counts, we assume a linear relationship between counts and the flux of the source. This function will be slightly different between each chip as they are not all identical. Therefore, chip by chip, we identify SDSS sources in each image using `astroquery`[4] and then fit a line to their counts as measured by SE (see Sec. 2.4.1) vs. the apparent V band magnitude . We calculated the V band magnitude from the SDSS g and r magnitudes using

$$V = g - 0.59 * (g - r) - 0.01 \tag{2.6}$$

(*Jester et al.*, 2005). We used V-band magnitudes in order to compare to the predicted V-band magnitudes from SkyBoT (*Berthier et al.*, 2006) for the known Solar System objects in our image.

One may expect that our fitted lines should have slopes of -0.4. However, we found that restricting our fit to have a slope of this value led to synthetic sources with counts that were systematically higher than the real sources. Since the light observed from asteroids in optical wavelengths is primarily reflected sunlight, we compared the fitted line to only SDSS sources with solar-like colors: g-r $= +0.44 \pm 0.02$. We found that these fits consistently overpredicted the number of counts for faint sources. We suspect that this discrepancy is due to a breakdown in the assumption that VR and V magnitudes should be comparable. In particular, the VR filter is essentially a very broad r filter ($\lambda \sim 475 - 750$ nm) that overlaps with the g band. Since solar-type objects are more red (g-r $= +0.44$), this implies that the the flux overlapping with the g-band would be lower than expected assuming the object had a flat spectrum over VR. Therefore, the overlap with the g-band would be overpredicted, leading to consistently higher flux counts overall for solar-type objects. Therefore, we instead fit a line to only the solar-type SDSS objects in our images without imposing a slope constraint.

[4]doi.org/10.5281/zenodo.1160627

Fig. 2.6 shows the final comparison between the real counts for SDSS sources and Solar System object sources versus the measured counts for their synthetic counterparts. In both cases, most of the sources follow the one-to-one line, and nearly all of the synthetic sources have a number of counts within an order of magnitude of the real counts. There is more deviation at the faint end, but this is expected since this regime is more dominated by noise. There is a noticeable systematic surplus of counts for synthetic SDSS objects at the bright end (Fig. 2.6). This discrepancy is likely due to the saturation limit; while real sources cannot have a number of counts exceeding this limit, there is no such restriction for the synthetic objects, allowing them to have increasingly more counts as compared to the real sources. Since we do not see this problem at the faint end or for the Solar System objects, we do not attempt to correct for it. Also, in most cases, the angular size of the synthetic sources is nearly the same as the real source. Since the synthetic objects have similar sizes and counts compared to the real sources, we conclude that our method is able to inject realistic synthetic objects into our data set.

2.6.3 Upper Limit on ET Population

To calculate an upper limit on the ET population, we injected the Strict set of synthetic ET objects (see Sec. 2.6.1) following the methods described in Sec. 2.6.2. Of course, only sources that fell within the survey area could actually be injected into our images; 886 of the 20,555 objects were injected into our images (see Fig. 2.8). This means that our survey covered 4.3% of this population. However, our survey only covered the L5 point, meaning we have no direct constraints on the L4 population. Therefore, we calculated our upper limits for the L5 population only. Since there were 3726 L5 ETs in the full synthetic set, our survey coverage of L5 ETs specifically is 24.0%. However, assuming that the L4 and L5 points are symmetric, our upper limit is applicable to the L4 population as well.

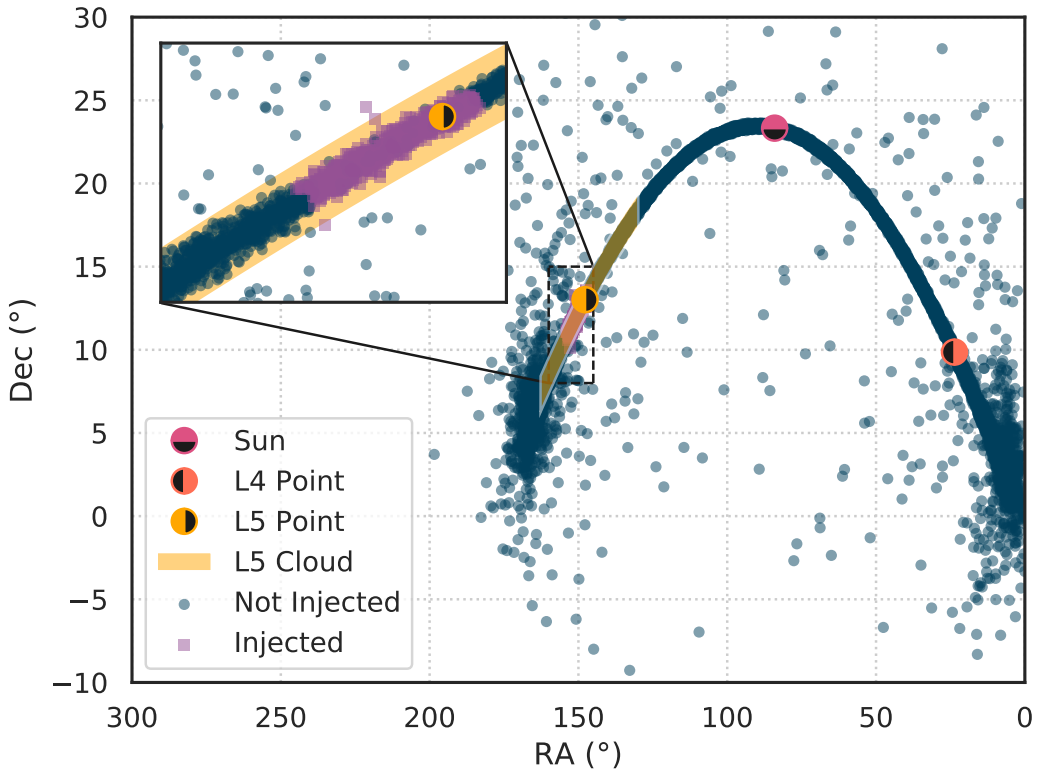

Figure 2.8: This figure demonstrates coverage by our survey of the synthetic ET population. The Lagrange points and the Sun are plotted as half filled circles for reference. The yellow shaded area represents the L5 cloud (the area with ecliptic longitude within 30 degrees of L5). Synthetic ETs (see Sec. 2.6.1) that were injected into our images are plotted as purple squares, while those that were not are blue circles. These injected points essentially depict the area covered by our survey. These objects make up 24% of the ETs in the L5 cloud.

We then ran these images with synthetic ETs through our pipeline (Sec. 2.4) and counted the number of injected ETs that were then detected, linked, and flagged as an ET candidate. Fig. 2.9 shows the recovery rate as a function of H. These plots are representative of the efficiency of our pipeline and our detection limit. Of note, there were 7 injected ET that were linked by the pipeline but were *not* flagged as ETs due to to having speeds inconsistent with our 1 deg./day assumption. These objects are a small fraction of the nearly 1000 synthetic ETs injected into our images and were expected for synthetic objects with a small geocentric range (see Fig. 2.2). These objects are not included in our recovery rate, as we would not have considered them to be an ET candidate.

Overall, we recovered about 50% of the injected ETs. As expected, our recovery rate is much higher for the brighter objects and becomes very low at the faint end (12.8% at H=20.4). In Fig. 2.9, our limiting absolute magnitude appears to be H$\sim$20; however, H does not correspond directly to the V-band magnitudes of the injected ETs.

From these recovery rates we can calculate an upper limit on the ET population adopting a Frequentist approach. Since we did not detect any ET candidates in our survey, by Poisson statistics, detecting 3 objects is within 3σ of our result. Therefore we calculate our limit as

$$U(H) = \frac{3}{R(H) * C} \tag{2.7}$$

where U(H) is our calculated upper limit, R(H) is the recovery rate as a function of H (see Fig. 2.9) and C is the coverage of the L5 cloud for our survey (see Fig. 2.8). Again, R(H) accounts for the performance of our pipeline and our limiting magnitude while C accounts for the limited area of our survey.

Fig. 2.10 shows our calculated upper limits as a function of H and of size (assuming an albedo of 0.15). We also plot previously measured/estimated upper limits on the ET population at H=20.5. There are two distinct regimes in this recovery rate:

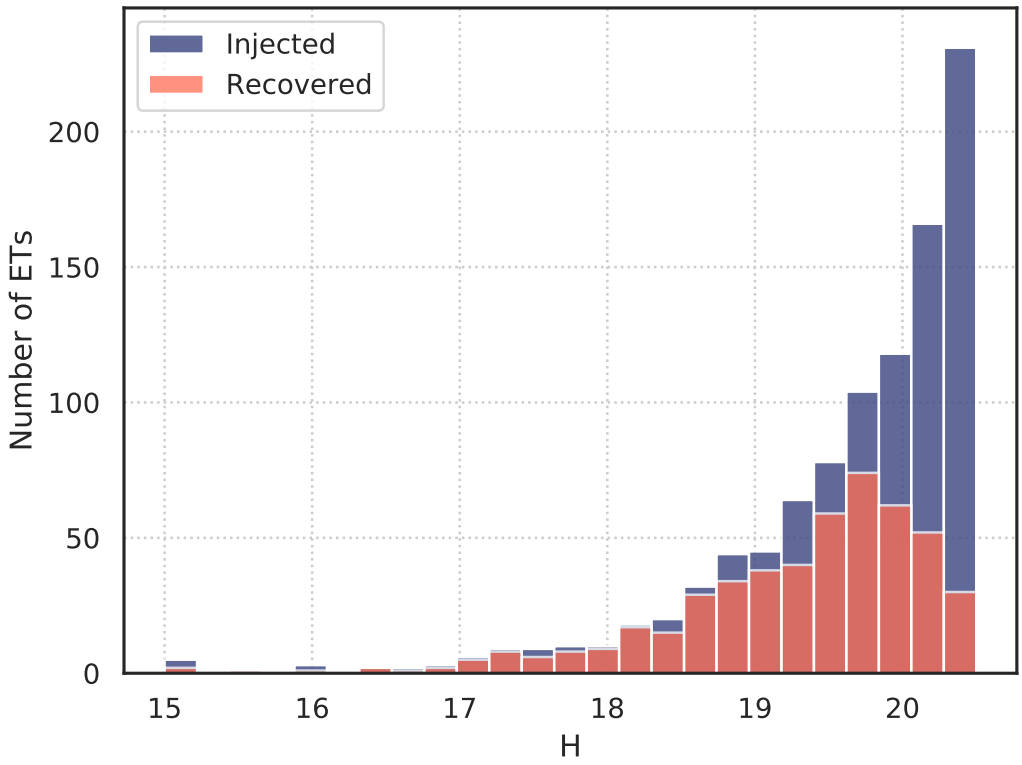

Figure 2.9: This figure compares the injected ETs (blue) from the set of Synthetic ETs to those that were detected, linked, and flagged as ET candidates by our pipeline (red); in other words, this plot shows our recovery rates as a function of H. We have nearly 100% recovery rates for most of the bins at the bright end, and the rates begin to fall off at ∼H=19.7. This value is essentially our limiting magnitude in H (though this does not directly relate to our limiting magnitude in V-band). Overall, we recovered ∼50% of the injected ETs.

flat at the bright end and sharp growth at the faint end. The upper limit becomes significantly higher at the faint end due to our limiting magnitude. In other words, the recovery rate becomes so low for the faintest objects that we only have relatively poor constraints on the population. Regardless, our calculated upper limit for the faintest H bin, H = 20.4 (∼300 m), is 97. The bright end is essentially flat because the recovery rate was nearly 100% for these bins; since C is the same for all bins and the recovery rate nearly the same, the calculated upper limit is constant (∼15).

If we assume that the underlying H distribution of the ET population follows a power law of index similar to that of the reported distributions for NEOs and main belt asteroids, we can calculate even more stringent (but model-dependent) upper limits for magnitudes in the flat regime. However, the true ET population may not follow such a distribution. If the ET population is primarily comprised of temporarily captured asteroids or NEOs, this assumption is likely reasonable. However, if the ET population is more similar to the ancient asteroid belt, it could be much shallower (*Tsirvoulis et al.*, 2018) or depend on its collisional history (*Bottke et al.*, 2005). There is also evidence for differences in albedo and size distributions amongst NEO sub-groups themselves (*Mainzer et al.*, 2012). With our current sparse observational constraints, it is not possible to take these complexities into account; we instead assume the population follows a single power law of index in the range 0.46-0.7.

Following this assumption, we calculate a cumulative H distribution as a power law normalized to our calculated upper limit for the faintest H bin still in the flat regime (corresponding to the dotted line in Fig. 2.10). We assume $\alpha = 0.46$ and 0.54 as before (see Sec. 2.6.2) and 0.7 for comparison to *Cambioni et al.* (2018) (see Sec. 2.7.2). Fig. 2.11 upper limits calculated by extrapolation Eq. 2.5 assuming each of these power laws. It is clear that with this method we obtain much more stringent constraints on bright ETs than in Fig. 2.10; we even obtain an upper limit of < 1 ET at H $\lesssim$ 15.5, 16.3, 17.2 for α=0.46, 0.54, 0.7 respectively. We also calculate an upper

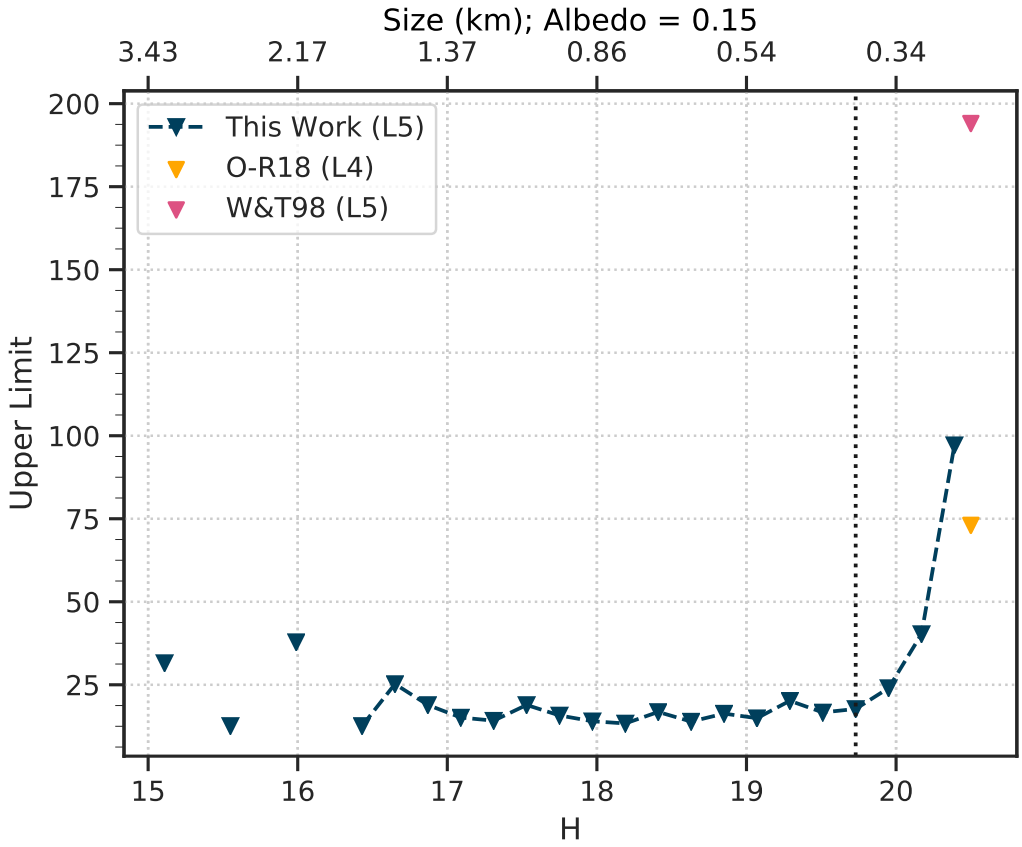

Figure 2.10: Upper limits on the ET population calculated from our survey area coverage (Fig. 2.8) and recovery rate (Fig. 2.9). The yellow triangle depicts the upper limit calculated for L4 ETs by *Cambioni et al.* (2018), while the pink triangle is the upper limit extrapolated from the *Whiteley and Tholen* (1998) results by *Cambioni et al.* (2018). The upper limits from this work have two distinct regimes: flat at the bright end and steeply increasing at the faint end. We get a sharp increase for the faintest magnitudes due to our limiting magnitude and relatively poor recovery rates for faint ETs. For the faintest bin, H=20.4, we calculate an upper limit of 97 ETs. This limit is clearly more stringent than that from the *Whiteley and Tholen* (1998) results (194) and somewhat higher than the *Cambioni et al.* (2018) limit (73) for L4. Our recovery rates are flat at the bright end because all of these bins had nearly 100% recovery rates leading to a constant upper limit (∼15) for those magnitudes. The dotted line represents the faintest magnitude (H=19.7) still within the flat regime. At this magnitude, we calculate an upper limit of 18.

limit of $\sim 60-85$ (depending on the power law assumed) ETs with H < 19.7 (d$\sim$390 m assuming an albedo of 0.15). Note that α=0.46 gives the most conservative upper limits for bright/large objects, whereas α=0.7 gives the most conservative limits at the faint end.

2.7 Discussion

2.7.1 Summary

In this work, we present the results of our search for L5 ETs using the VR filter on DECam. In total, our survey covered 24 sq. deg. near the Earth-Sun L5 point. Our survey only consisted of $\sim$ 1 hour of observations, so the arcs for any observed Solar System objects were not long enough to fit an orbit or dynamically classify these objects. However, ETs are expected to have a distinctive rate of motion on the sky of 1 deg./day (Fig. 2.2). Therefore, we developed the *Bullseye* code to link together transient objects in our exposures and flag any tracklets with a similar speed as an ET candidate.

With this survey, we found 27 tracklets that do not correspond to any previously known Solar System objects (see Table 2.3). However, none of these objects were flagged as ET candidates. Based on this non-detection, we place upper limits (see Figs. 2.10, 2.11) on the ET population of $\sim 60-85$ ETs with H$<$19.7 (corresponding to a size of $\sim$ 390 m assuming an albedo of 0.15) and 97 ETs with H=20.4 ($\sim$290 m).

2.7.2 Comparison to Previous Surveys

There have been three previous dedicated searches for ETs (*Whiteley and Tholen*, 1998; *Cambioni et al.*, 2018; *Yoshikawa et al.*, 2018). No ETs were found and no upper limits have been published in the Hayabusa2 search, so we can only compare to W&T98 and O-R18. W&T98 was similar to our search in that it was ground-

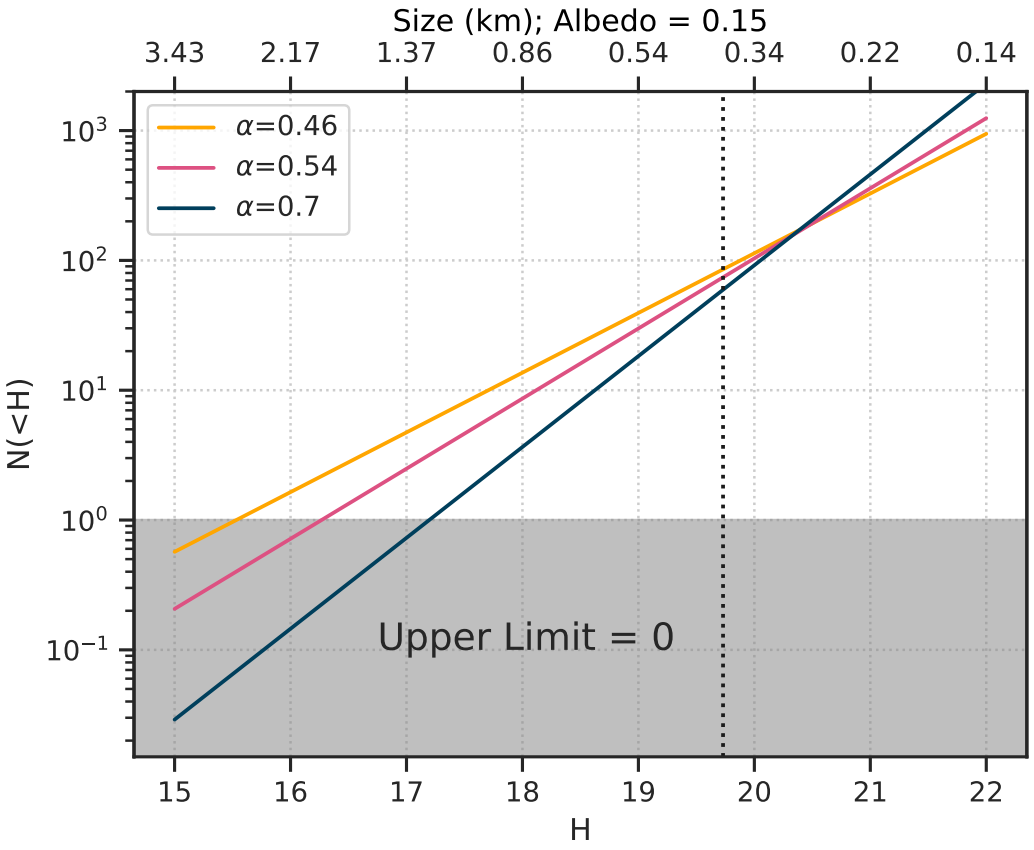

Figure 2.11: This figure depicts the stricter upper limits calculated for bright ETs assuming the ET H distribution follows a power law (Eq. 2.5). Slopes of 0.46-0.54 are consistent with the H distributions for main belt asteroids. A slope of 0.7 was used in *Cambioni et al.* (2018) for similar extrapolations to compare their results to *Whiteley and Tholen* (1998). The dotted line represents the point used for extrapolation, H=19.7 (see Fig. 2.10). The grey region depicts where N(<H) < 1, meaning the upper limit is essentially 0 ETs. Note, α=0.46 gives the most conservative upper limits of the three power laws at the bright end, while α=0.7 is most conservative at the faint end.

based and covered L5, but it covered a much smaller area (∼0.35 sq. deg.). The O-R18 search was quite different in that is was conducted as the probe flew through the Lagrange point and it covered L4 rather than L5. However, we are still able to make comparisons to their results as we would expect the populations at the two Lagrange points to be symmetric.

We first compared our faintest upper limit (at H=20.4) to the upper limits for W&T98 and O-R18 as calculated in *Cambioni et al.* (2018) (see Fig. 2.10). Our upper limit of 97 ETs is slightly higher than the O-R18 result of 73 ETs at L4, but clearly more stringent than the upper limit calculated based on the W&T98 search (194 ETs).

However, in comparing to this single magnitude, we are comparing to our most poorly constrained upper limit. Therefore, we follow a process similar to that used in *Cambioni et al.* (2018) in which we extrapolate these other upper limits to a brighter H for which our survey has better constrained upper limits by assuming a power law distribution (see Sec. 2.6.3). This method requires assuming a slope parameter; we use α=0.46 for H<20.39 and α=0.7 for H>20.39 as these values give the most conservative upper limits in Fig. 2.11.

Fig. 2.12 shows the extrapolated upper limits using this model; for each survey, the circular point is the upper limit at the magnitude that we extrapolated from (coming from this work and *Cambioni et al.* (2018)). Again, our upper limits are clearly more stringent than the W&T98 limits. Under these assumptions, our upper limits are also slightly more stringent than those from O-R18; if we used a power law with α=0.7 only instead, our results are essentially consistent with the O-R18 results. At H=19.7, the point of extrapolation used for this work, we calculate an upper limit of 18, 32, and 81 ETs for this work, O-R18, and W&T98 respectively. In short, although our survey does not have as faint of a limiting magnitude as the previous surveys, we are able to place more stringent limits on the L5 population at

brighter magnitudes than *Whiteley and Tholen* (1998) and limits that are consistent to slightly more stringent than the OSIRIS-REx L4 search (*Cambioni et al.*, 2018).

2.7.3 Missing Primordial ETs?

After this work, the existence/characterization of primordial ETs is still an open question. Even though it is almost certainly not primordial, 2010 TK_7 remains the only known ET. All of the current upper limits on the ET population, including from this work, suggest that there could still be tens to hundreds (depending on size) of ETs outside of the survey area of four independent searches. Deeper and broader coverage of both Lagrange clouds is necessary to say definitively whether or not other ETs exist.

However, a dearth of additional ETs would not be entirely surprising, especially for very faint/small objects. Numerical simulations have suggested that primordial ETs with H >20.5 (assuming an albedo of 0.1) are likely to be destabilized due to the Yarkovsky effect within 4.5Gyr (*Zhou et al.*, 2018). These results combined with previous non-detections of ETs lead *Zhou et al.* (2018) to conclude that it is very unlikely that primordial ETs of absolute magnitude H $\leq$ 20.5 (or their equivalent size limit) exist at the Lagrange points today, which could explain the current paucity of ETs. This work, as well as previous surveys, are sensitive to objects primarily above this limit; thus, deeper searches would allow us to test this theoretical limit.

It is important to note that it is also possible for asteroids to be temporarily trapped in an ET-like orbit, like 2010 TK_7. *Morais and Morbidelli* (2002) found that such objects are likely quite rare though; through their simulations they calculated an upper limit of 0.65$\pm$0.12 and 16.3$\pm$3.0 captured Earth co-orbitals for H<18 and H<22 respectively. Based on these results, it seems possible that 2010 TK_7 truly is the only Earth co-orbital. However, it is also possible that the Yarkovsky effect (not included in those simulations) could in fact improve the capture efficiency for

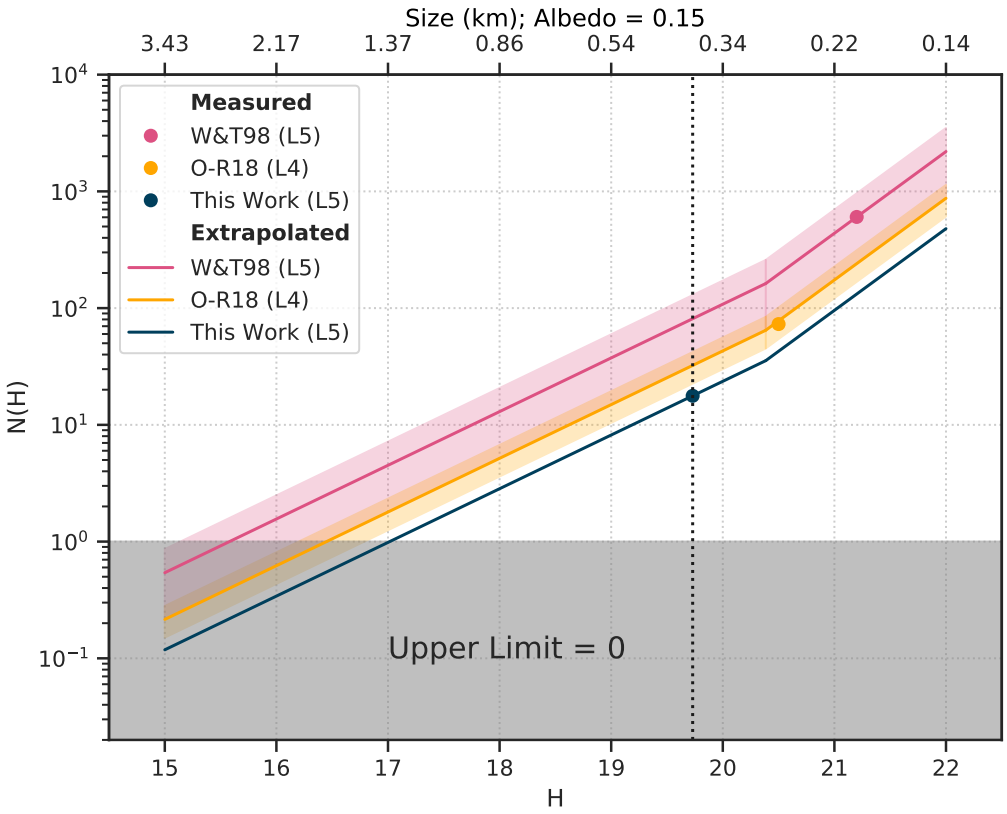

Figure 2.12: Extrapolated upper limits (lines) based on the measured upper limit (circular points) for each survey. The results for this work are in blue, *Cambioni et al.* (2018) in yellow, and the upper limit calculated by *Cambioni et al.* (2018) based on the results in *Whiteley and Tholen* (1998) are in pink. The dotted line represents the point used for extrapolation for the results in this work, H=19.7. The grey region depicts where N(H) <1, meaning the upper limit is essentially 0 ETs. The slope of the power law we use is α=0.46 for H<20.39 and α=0.7 for H>20.39, which gave the most conservative upper limits in Fig. 2.11. Under these assumptions, the results from this work give the most stringent upper limit on the ET population to date (18 ETs with H=19.7 as compared to 32 and 81). For steeper power laws, the upper limits for this work are essentially consistent with O-R18.

transient co-orbital ETs (*Malhotra*, 2019).

Ultimately, in the absence of stronger observational constraints, there is still little we can definitely say about the present-day population of ETs. Broader and deeper searches are still needed in order to further constrain this population.

CHAPTER III

Photometric Survey of Neptune's Trojan Asteroids I: The Color Distribution

3.1 Preface

This chapter has been submitted to the Planetary Science Journal (Markwardt et al. 2023). The paper led by Markwardt and is co-authored by H W Lin (who advised Markwardt during this paper and assisted with telescope observations), D W Gerdes, and F C Adams (both of whom contributed to the manuscript itself), and is reproduced here with minor stylistic revisions.

3.2 Introduction

Trojan asteroids are planetary companions that reside in the asymmetric 1:1 mean-motion resonance of planets; these asteroids librate at the planet-Sun L4 and L5 Lagrange points, meaning that they have the same orbit as the planet but librate about a point 60° ahead of (L4) or behind (L5) the planet. Numerical simulations show that orbits of Trojan asteroids can be quite stable, on order the age of the Solar System (*Ćuk et al.*, 2012; *Gomes and Nesvorný*, 2016a; *Lykawka et al.*, 2011). Therefore, the stable members of these populations are likely relatively undisturbed remnants of our

primordial planetary disk. The physical properties of these populations can thus give us a window into the early Solar System.

However, Neptune's Trojan asteroids are not thought to have formed *in-situ*. Rather, this population likely grew through capture of planetesimals during the epoch of planetary migration. According to the Nice model, the outer planets migrated from the location of their formation to their present day locations (*Tsiganis et al.*, 2005). Assuming Neptune migrated significantly in its early evolution, the Lagrange points must have also migrated with it (*Kortenkamp et al.*, 2004) Therefore, the NT population can be used to constrain migratory models (*Gomes and Nesvorný*, 2016a; *Nesvorný et al.*, 2013, 2018; *Pike et al.*, 2017a). Such migration would have occurred in the first several hundred Myr in the history of the Solar System, so while these objects may not have formed *in-situ*, they still are remnants of the very early Solar System.

Such models show that the Jupiter Trojan populations do not survive planetary migration, indicating they must have originated from elsewhere in the Solar System (*Roig and Nesvorný*, 2015). Since the dynamics of planetary migration likely dispersed any primordial NTs as well, from where did the current population of NTs originate? The most likely source is the nearby Kuiper Belt. If that were the case, one would expect these two populations to be similar in size and color (surface composition). Regarding the color of the KBOs, the bimodality of red ($g - i < 1.2$) vs. ultra-red ($g - i > 1.2$) members has been well established (*Sheppard*, 2010; *Schwarz et al.*, 2011; *Hainaut et al.*, 2012; *Peixinho et al.*, 2012; *Sheppard*, 2012; *Lacerda et al.*, 2014; *Peixinho et al.*, 2015; *Pike et al.*, 2017b; *Wong and Brown*, 2017b; *Schwamb et al.*, 2019). Similarly, the centaur population, small bodies which orbit between Jupiter and Neptune, are thought to be fed by planetesimals escaping the NT region (*Horner and Lykawka*, 2010). These objects are also red/ultra-red in color (*Peixinho et al.*, 2012, 2015).

Through 2018, no ultra-red NTs had been found, making their color distribution distinctly different than their expected origins or offshoots. Termed the "Trojan Color Conundrum", this tension is not easy to resolve (*Jewitt*, 2018). One explanation is that some sort of resurfacing has happened to the NT population specifically that affected neither the centaurs or KBOs. Jupiter's Trojan population is also devoid of ultra-red members which is thought to be due to thermal resurfacing (*Luu and Jewitt*, 1996; *Jewitt*, 2002). However, the temperatures at the distance of Neptune are to cold for such a scenario to be valid (*Jewitt*, 2018). Another potential explanation is collisional resurfacing, which could strip the ultra-red crust off of the surfaces of these bodies revealing a bluer surface underneath. One source of such collisions could be Plutinos, 3:2 resonators with Neptune, which have significant orbital overlap with the NT population (*Almeida et al.*, 2009). Such collisions are expected to occur when Plutinos have high libration amplitudes, high eccentricities, and low inclinations; therefore, we would expect the color distribution of NTs to be inclination-dependent as well, where high inclination NTs avoid these collisions and retain their ultra-red surfaces. Finally, this discrepancy could be due to a primordial boundary between red/ultra-red bodies that was subsequently mixed by Neptune's migration (*DeMeo and Carry*, 2014; *Neveu and Vernazza*, 2019). Based on the exact nature of the epochs of radial mixing, mass removal, and planet migration, the resulting NT population could be devoid of ultra-red members while the Centaur population is not (*Neveu and Vernazza*, 2019), but specific simulations of these two populations have not been conducted. This hypothesis has been supported by the discovery of two TNO-like (red) objects all the way in the asteroid belt (*Hasegawa et al.*, 2021).

In 2019, the first ultra-red NT, 2013 VX_{30}, was discovered (*Lin et al.*, 2019), potentially resolving this conundrum. However, the red to ultra-red ratio now stands at 17:1 rather than in the range from 4:1 to 11:1 as observed for KBOs (*Schwamb et al.*, 2019). Colors have been measured for 16 OF 31 NTs (*Sheppard and Trujillo*,

2006; *Sheppard*, 2012; *Parker et al.*, 2013; *Jewitt*, 2018), but there has been no optical photometric survey of the entire NT population. Thus, the true color distribution is still unclear.

The structure of this paper is as follows: Section 2 describes the design of our photometric survey. Section 3 outlines our data reduction process. Section 4 presents the results of our survey. Section 5 discuss the meaning of our results. Section 6 is conclusions drawn from these results.

3.3 Survey Design

The goal of this paper is to measure the optical colors of currently known NTs in order to better understand the physical characteristics of their surfaces. The targets are listed in Table 3.1. We attempted to maximize the number of targets without previous color observations while still including some that do for comparison purposes. All of our targets, except 2015 VU_{207}, were already known to be stable for ∼Gyr (*Lin et al.*, 2021, 2022). Following the methods of *Lin et al.* (2022), we find that 2015 VU_{207} is also stable for the length of our simulations.

We used the IMACS f/4 instrument on the 6.5m Baade telescope at Las Campanas Observatory on 4 unique nights to observe this population. IMACS was most suitable for this task with its optical wavelength coverage (∼400 - 900 nm) and large FOV to account for the positional uncertainty of the targets. The Sloan $g'r'i'z'$ filters were used for our photometric measurements. In order to account for any variation due to a target's rotational period, we observed each target in the following sequence: r'-g'-r'-i'-r'-z'-r'. We chose r' to be the "bounding" observations since this filter reaches the highest SNR in the shortest amount of time. The fast readout mode with 2x2 binning was used.

Table 3.1: NT targets of this survey. Columns: (1) Object Designation, has previous color measurements taken from 1: *Sheppard* (2012), 2: *Parker et al.* (2013), 3: *Jewitt* (2018), 4: *Lin et al.* (2019); (2) Lagrange Point; (3) Eccentricity; (4) Inclination (°); (5) Absolute Magnitude; (6) Dates observed; (7) Measured ave. SDSS r-band magnitude; (8) Measured SDSS g-r (mag); (9) Measured SDSS r-i (mag); (10) Measured SDSS r-z (mag); (11) Color classification determined based on each targets g-r vs r-i colors.

Name	L4/L5	e	i	Date Observed	Ave. r	$g-r$	$r-i$	$r-z$	Color Class.
2006 RJ_{103}[1]	L4	0.03	8.1	113021	22.03	0.54 ± 0.017	0.19 ± 0.015	—	red
				120222	21.89	—	—	0.23 ± 0.014	
2007 VL_{305}[1,2]	L4	0.07	28.1	113021	22.61	0.66 ± 0.013	0.16 ± 0.010	—	red
				120222	22.61	—	—	0.30 ± 0.120	
2008 LC_{18}	L5	0.08	27.5	073021	23.15	0.93 ± 0.051	0.28 ± 0.046	0.12 ± 0.038	ultra-red
2010 TS_{191}[3]	L4	0.05	6.6	113021	23.38	0.62 ± 0.016	0.23 ± 0.016	—	red
2011 HM_{102}[2]	L5	0.08	29.3	073021	22.44	0.56 ± 0.010	0.23 ± 0.009	0.19 ± 0.009	red
2011 SO_{277}[3]	L4	0.01	9.6	113021	22.38	0.64 ± 0.018	—	—	red
				120222	22.57	—	0.47 ± 0.012	0.76 ± 0.023	red
2012 UD_{185}	L4	0.04	28.3	113021	22.29	0.66 ± 0.013	0.25 ± 0.017	0.02 ± 0.022	red
2012 UV_{177}	L4	0.07	20.8	113021	23.90	0.79 ± 0.020	0.33 ± 0.019	—	ultra-red
2013 RL_{124}	L4	0.03	10.1	113021	23.49	0.56 ± 0.013	0.51 ± 0.014	—	red
2013 TZ_{187}	L4	0.07	13.1	113021	23.25	1.1 ± 0.024	0.33 ± 0.021	—	ultra-red
2013 VX_{30}[4]	L4	0.09	31.2	113021	22.58	1.1 ± 0.020	0.39 ± 0.014	0.88 ± 0.012	ultra-red
				091122	23.00	0.64 ± 0.025	0.50 ± 0.014	0.82 ± 0.012	red
2014 RO_{74}	L4	0.05	29.5	120222	23.34	0.64 ± 0.035	0.33 ± 0.023	1.12 ± 0.025	red
2014 SC_{374}	L4	0.10	33.7	113021	23.47	0.38 ± 0.017	0.40 ± 0.016	0.70 ± 0.022	red
2014 YB_{92}	L4	0.10	30.8	091222	23.68	-0.08 ± 0.022	0.28 ± 0.013	0.43 ± 0.011	indeterminate
				120222	23.53	0.18 ± 0.025	0.24 ± 0.020	0.77 ± 0.022	indeterminate
2015 VU_{207}	L4	0.03	38.9	080922	22.24	0.43 ± 0.011	0.17 ± 0.010	0.30 ± 0.009	red
				091122	22.08	0.49 ± 0.012	0.07 ± 0.014	0.26 ± 0.008	red
2015 VV_{165}	L4	0.09	16.8	113021	23.28	0.91 ± 0.020	0.21 ± 0.015	—	ultra-red
2015 VW_{165}	L4	0.05	5.0	113021	22.83	0.54± 0.014	0.61 ± 0.012	—	red
				120222	22.94	—	—	0.67 ± 0.033	

3.4 Photometric Reduction

3.4.1 Calibration

To calibrate the photometry of our IMACS observations, we cross-matched the in-frame background stars against PS1 sources (*Magnier et al.*, 2013). We first converted the PS1 griz photometry to the SDSS system using the transformation equations in *Tonry et al.* (2012), and then selected the sources with $g-r$ between 0.25 and 2.0 as the reference sources. By solving the equation below using the apparent magnitude of the reference sources, we determined the photometric zeropoint of each frame:

$$m_{sdss} = m_{ins} + 2.5\log_{10}(\tau_{exp}) + m_0, \tag{3.1}$$

where m_{sdss} is the apparent magnitude of a specific band of the cross-matched reference sources, m_{ins} is the instrumental magnitude of that specific band measured from the IMACS image, τ_{exp} is the exposure time, and m_0 is the photometric zeropoint of that frame.

After we determined the zeropoints of each frame, we used every cross-matched star in every frame to evaluate the linear color conversions between the IMACS and SDSS photmetric system by solving the following equation:

$$m_M = m_{sdss} + a\ (g-r)_{sdss} + b, \tag{3.2}$$

where m_M and m_{sdss} are the IMACS and SDSS magnitude, respectively, and a, b are the coefficients of the linear conversion. The results are:

$$\begin{aligned} g_M &= g_{sdss} - 0.078(g-r)_{sdss} + 0.069 \\ r_M &= r_{sdss} - 0.024(g-r)_{sdss} + 0.024 \\ i_M &= i_{sdss} - 0.092(g-r)_{sdss} + 0.128 \\ z_M &= z_{sdss} - 0.026(g-r)_{sdss} + 0.031 \end{aligned} \tag{3.3}$$

With the photometric zeropoints and the color conversion equations, we are able to measure the griz colors of targets in SDSS photmetry system.

3.4.2 PSF Modeling

To accurately measure the flux and apparent magnitude of NTs, we select stars around the target NT to model the local PSF. Several popular analytical functions are considerate to modeling the PSF, such as Moffat (*Moffat*, 1969) and the sum of 2D Gaussians (*Bendinelli et al.*, 1990). Both functions can adequately model the "wing" of PSF. However, considering our PSF can be asymmetric (not round, see Figure 3.1), we model the PSF by using the superposition of n asymmetric 2D Gaussians. The

flux of the PSF at any point in the (x', y') orthogonal coordinate system is:

$$PSF(x', y') = b(x', y') + \sum_{i=1}^{n} \mathrm{A_i} \left(\mathtt{exp}\big[-(\frac{x'^2}{2\sigma_{x'i}^2} + \frac{y'^2}{2\sigma_{y'i}^2}) \big] \right), \tag{3.4}$$

where $b(x', y')$ is the background flux at that point, n is a small number, A_i is the amplitude of individual Gaussian, $\sigma_{x'i}$ and $\sigma_{y'i}$ are the widths on x' and y' axes of individual Gaussian, respectively. This equation can be rotated to the image reference frame (x, y) with a position angle θ and translating the centroid to (x_0, y_0) such that

$$\begin{pmatrix} x' \\ y' \end{pmatrix} = \begin{bmatrix} \cos\theta & -\sin\theta \\ \sin\theta & \cos\theta \end{bmatrix} \begin{pmatrix} x - x_0 \\ y - y_0 \end{pmatrix}.$$

Therefore, the Gaussian functions share the same center, position angle, and ellipticity but have unequal contribution and different width. To properly choose 'n', the number of how many Gaussians we should use, we calculate Bayesian information criterion (BIC) for each n we use. The BIC is defined as:

$$\mathrm{BIC} = -2\ln(\hat{\mathcal{L}}) + k\ln(\mathrm{m}), \tag{3.5}$$

where $\hat{\mathcal{L}}$ is the maximum likelihood of the model, k is the number of parameters estimated by the model, and m is number of data we use to fit the model. The models with lower BIC values are generally preferred, and it penalizes the model with larger k automatically. Since the multiple Gaussian PSF model can be linearized by taking logarithm and assuming that the errors are normal distributed, the $\hat{\mathcal{L}}$ is equivalent to the least squares estimation, thus BIC can be written as a function of error variance $\hat{\sigma_e^2}$:

$$\mathrm{BIC} = m\ln(\hat{\sigma_e^2}) + k\ln(\mathrm{m}), \tag{3.6}$$

In other words, the model with lower residual and less parameter is preferred. We find that the model with n = 1, a single 2D Gaussian, always has highest BIC. On the other hand, the models with n = 2 and n = 3 generally have similar BICs, therefore we conclude that using any model with n > 3 is redundant.

Finally, we use the PSF model with n = 2 or 3, depend on which one has lower BIC. Once all of the parameters are measured via modeling the stars, the target NT can be modeled by refitting the center and amplitude of the PSF. The flux is the sum of the final model. Figure 3.1 demonstrates that both the star and the NT can be properly subtracted by the PSF model.

3.4.3 Rotation Curve Correction

The observed magnitudes, and the resulting colors we are trying to measure, are subject to rotational variations on the surface of these objects. To approximately account for this, we use a model that exhibits a linear variation in source brightness (its r'-band magnitudes) and constant $g' - r'$, $r' - i'$, $r' - z'$ colors (to convert each measurement to and r'-band magnitude). This model was then fit using a least-squares approach (see Fig. 3.2). The resulting colors converted to SDSS magnitudes (*griz*; see Eq. 3.3), which are reported in Table 3.1.

3.4.4 Reddening Line

Taken from *Hainaut and Delsanti* (2002), the reddening, or the spectral index, can be expressed as the percent of reddening per 100 nm:

$$S(\lambda_1, \lambda_2) = 100 * \frac{R(\lambda_2) - R(\lambda_1)}{(\lambda_2 - \lambda_1)/100} \tag{3.7}$$

where $R(\lambda)$ is taken from *Jewitt and Meech* (1986):

$$R(\lambda) = 10^{-0.4(m(\lambda) - m_\odot(\lambda))} \tag{3.8}$$

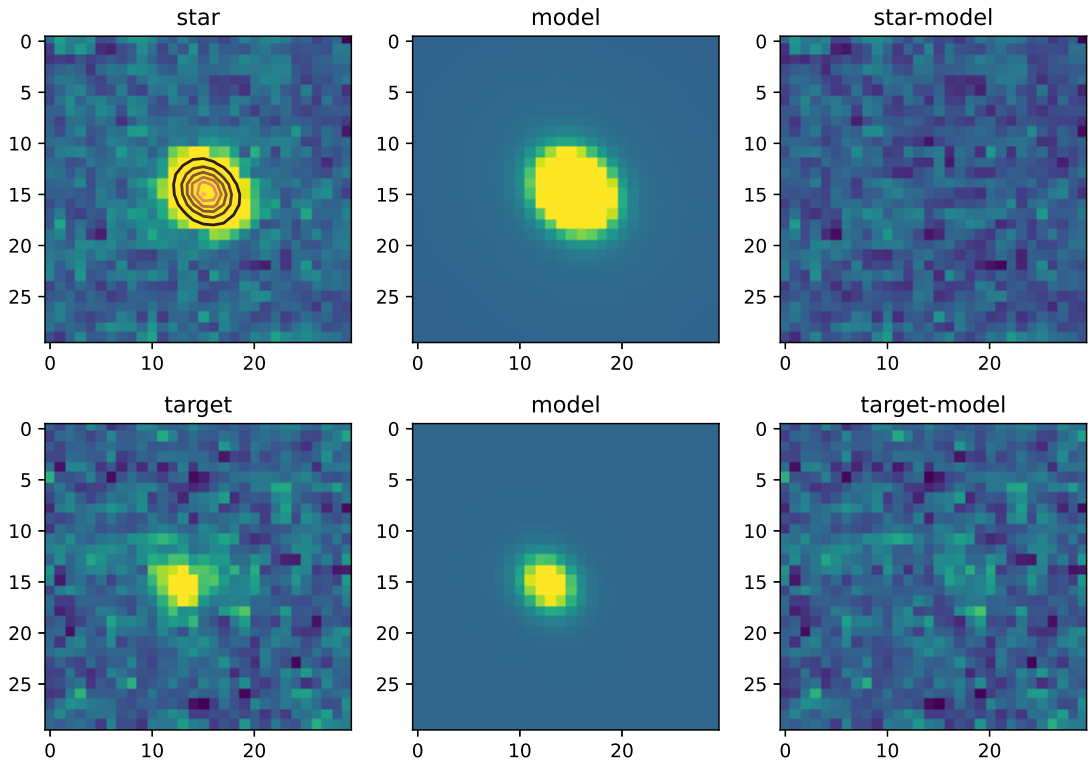

Figure 3.1: PSF modeling and subtraction. **top-left:** A star with the PSF model contour. **bottom-left:** The image of NT. **middle:** The model of the star (top) and the NT (bottom). **right:** the images after subtraction of the model.

such that $m(\lambda)$ and $m_{\odot}(\lambda)$ are the magnitude of the object and the Sun, respectively, at a particular wavelength, λ. Setting the reddening line to pass through the color of the Sun (i.e. for $S(\lambda_1, \lambda_2) = 0$, $m(\lambda_1) - m(\lambda_2) = m_{\odot}(\lambda_1) - m_{\odot}(\lambda_2)$), we can derive the following equation, assuming $m(\lambda_1) = m_{\odot}(\lambda_1)$:

$$m(\lambda_2) = -2.5log[1 - 10^{-4}S(\lambda_1, \lambda_2)(\lambda_1 - \lambda_2)] + m_{\odot}(\lambda_2) \tag{3.9}$$

Assuming $S(\lambda_1, \lambda_2)$ varies from -10% to 80%, we can plot the reddening line for $g - r$ vs $r - i$ and $g - r$ vs $r - z$ in Fig. 3.3 and Fig. 3.4 respectively. Note that our targets generally fall along the reddening line, as has been observed for small bodies in the outer Solar System previously (*Hainaut and Delsanti*, 2002). Objects that fall above/below the reddening line must exhibit emission/absorption lines at those particular wavelengths causing them to deviate from a flat spectral index.

3.5 Results

3.5.1 Color-Color Plots

In Fig. 3.3, we show the $g - r$ and $r - i$ colors measured for our NT targets. Our targets also exhibit bi-modality in this color space; while most targets fall within the "red" zone (principal component <1.75; see Sec. 3.5.2), there are four NTs in the "ultra-red" zone (principal component >1.75). Of these objects, two have no previous color measurements and are identified as ultra-red for the first time in this paper. This brings the red to ultra-red ratio for our sample to 3.75:1, or 7.75:1 for the entire known population. This ratio is much more consistent with the dynamically excited KBO ratio of between 4-11 : 1 (*Schwamb et al.*, 2019). However, comparing these ratios is not sufficient to determine if the NT and KBO population come from

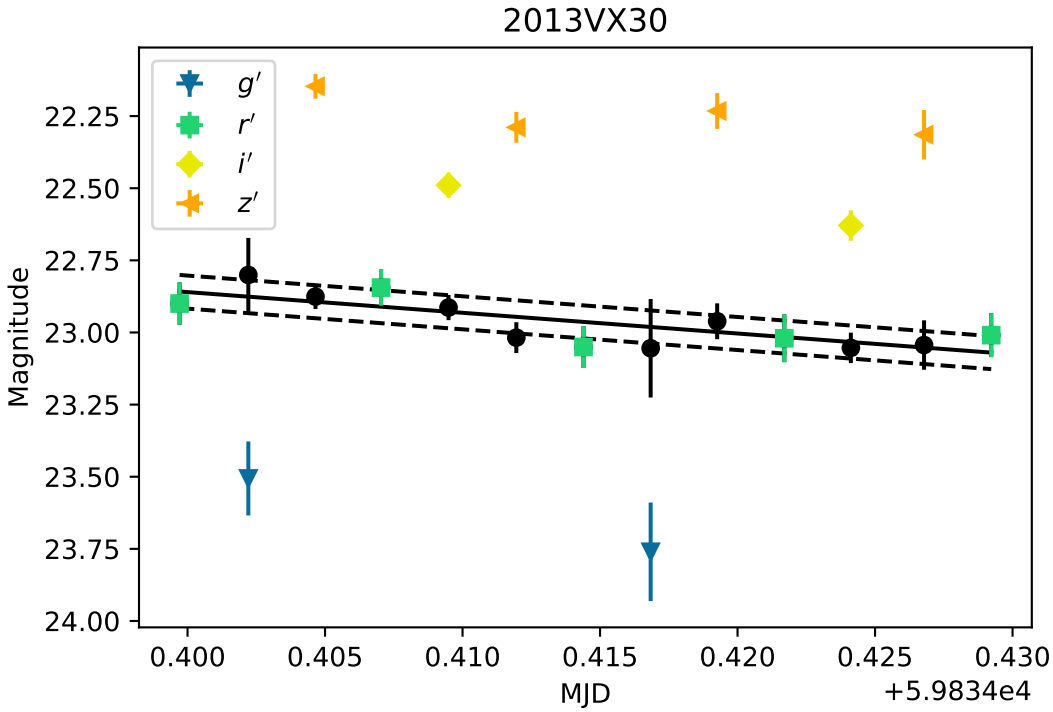

Figure 3.2: This figure shows our least-squares approach to fitting r'-band lightcurves and colors for an example NT target, 2013 VX30. Each observation is shown as a colored point (downward triangle for g', square for r', diamond for i', and sideways triangle for z'. We then used a constant, but free parameter, color term to convert each observation to an r'-band observations; these point are shown as black circles. The solid line is our least-squares fit to the r'-band (black) points. The dotted lines show our 1σ deviation from this fit.

the same source distribution (see Sec. 3.5.2).

In Fig. 3.4, we show the $g-r$ and $r-z$ colors measured for our NT targets. All of our targets are consistent with the scattered/hot TNO populations. This result is expected as NTs are thought to have originated from scattered/unstable TNOs. The physical cause of this z-band colorization of the cold TNO population is not currently clear, but must be due to some absorption feature around $900\mu m$ based on the displacement off of the reddening line. Spectroscopic information, such as will be taken with JWST (*Markwardt et al.*, 2021), will shed further light on chemical links between these populations.

For those targets that have previous measurements (five in our sample), we compare the difference between our measurements and those from the literature to our computed errors (shown in Fig. 3.5). We find that the observed differences in g-r are mostly within our observational errors, meaning our observations are roughly consistent with previous literature. However, previous observations are slightly systematically larger in r-i than our measurements. In most cases, this does not change the color classification of our objects, but our observations may be slightly more likely to be classified as ultra-red based on r-i. Similarly, our r-z measurements are slightly larger than previous observations. In every case, this did not change the color classification, but our objects may be slightly more likely to fall outside the cold TNO color region.

In Fig. 3.6, we plot each color measurement for our targets as a function of inclination, eccentricity, and absolute magnitude (H). It has been suggested that the red/ultra-red bimodality should depend on the target's inclination as objects with a high inclination are less likely to collide with the plutino population, allowing them to retain their ultra-red crust (*Lin et al.*, 2019). We find that all of our targets with $g-r > 0.7$ have inclinations above $\sim 10^{\circ}$. We do not however observe a similar relationship for the $r-i$ or $r-z$ colors. Therefore, if Plutino collisions are resurfacing objects at

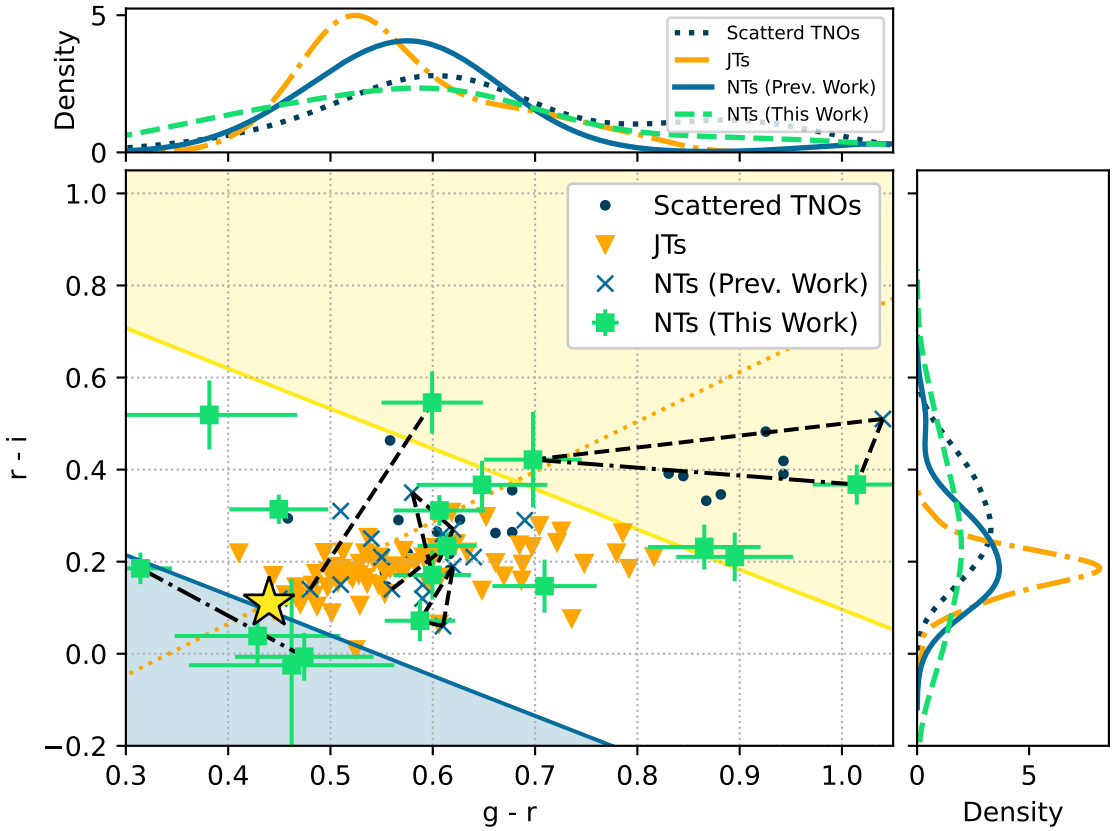

Figure 3.3: Measured $g - r$ vs $r - i$ of the NT population. Blue points are colors of scattered TNOs and orange triangles are JTs, both taken from the literature (*Hainaut et al.*, 2012). Light blue x's are previously observed colors of NTs (*Sheppard and Trujillo*, 2006; *Sheppard*, 2012; *Parker et al.*, 2013; *Jewitt*, 2018; *Lin et al.*, 2019). Targets observed in this paper are shown as green squares. Objects that have multiple observations in this paper are connected by a dot-dashed line. NTs that have been previously observed in the literature are connected by a dashed line. The yellow line marks values where the PCA yields values equal to our cutoff of 1.75 (see Fig. 3.7 and Sec. 3.5.2). Objects in the yellow region are above this cutoff and considered ultra-red in this paper. The blue line marks values where the PCA yields values equal to our cutoff of -1.25 (see Fig. 3.7 and Sec. 3.5.2). Objects in the blue region are blue this cutoff and considered blue in this paper. The top and right inset plots show the kernel density estimation (KDE) of the g-r and r-i distributions respectively of the included sub-populations.

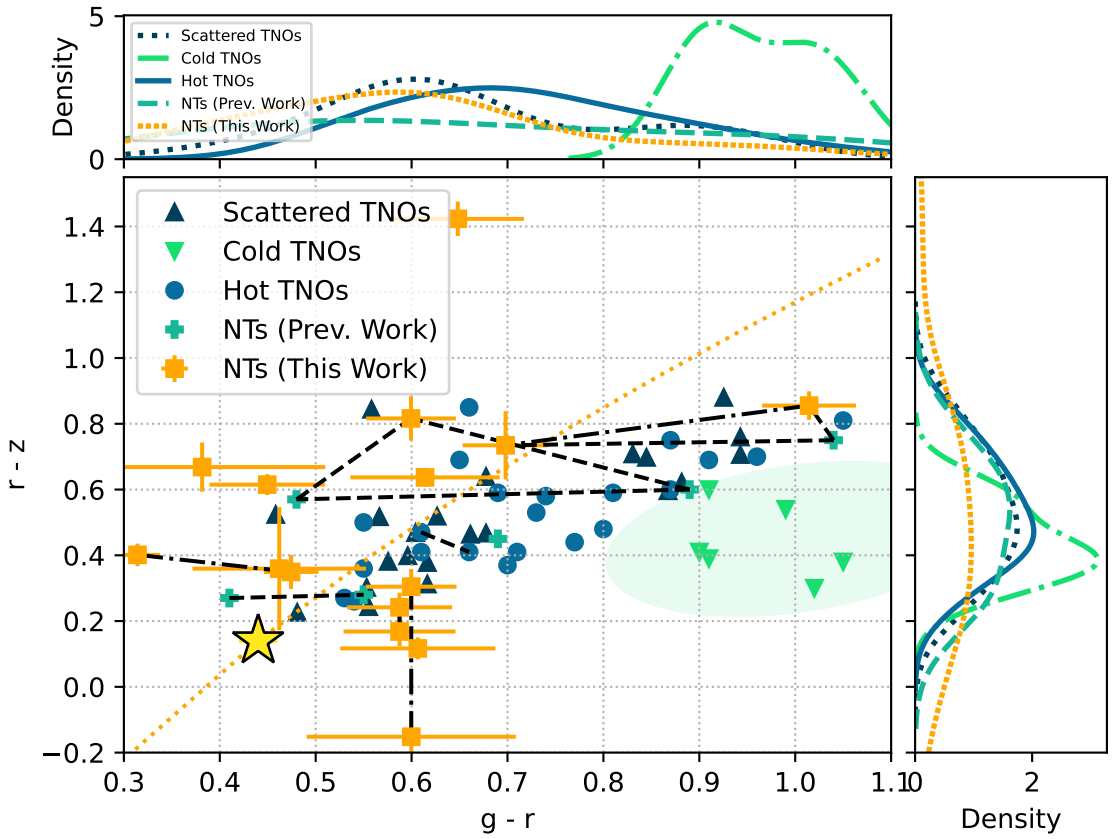

Figure 3.4: Measured $g - r$ vs $r - z$ of the NT population. Navy upward triangles, green downward triangles, and blue circles are measurements taken from the literature of TNOs (scattered, cold, and hot respectively) (*Schwamb et al.*, 2019). Teal plus signs are colors of NTs taken from the literature (*Lin et al.*, 2019). Targets observed in this paper are shown as orange squares. Solar color and the reddening line (see 3.4.4) are depicted as an yellow star and orange dotted line respectively. Objects that have observations taken in this paper and from the literature are connected with a dashed line. Objects that have multiple observations in this paper are connected by a dot-dashed line. The green ellipse demarcates the region of color-color space occupied only by cold TNOs. The top and right inset plots show the kernel density estimation (KDE) of the g-r and r-z distributions respectively of the included sub-populations.

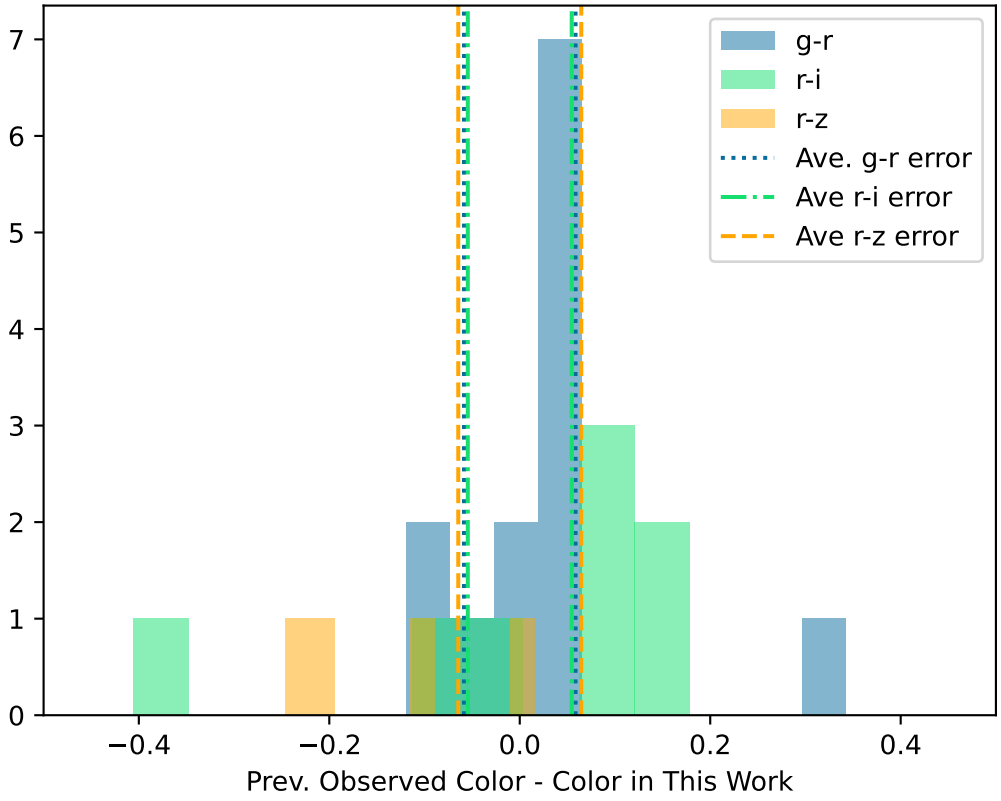

Figure 3.5: The differences in observed color between NTs in this paper and the literature as compared to the average error on our observations. The differences in g-r, r-i, and r-z observations are shown as blue, orange, and green histograms respectively. The average g-r, r-i, and r-z errors are shown as blue dotted, green dot-dashed, and orange dashed lines respectively

low inclinations, this effect must only be evident at wavelengths $\sim$500 μm.

To test the significance of this clustering we calculate the Cluster Index and Pearson Correlation Coefficient of our observations. The Cluster Index from the SigClust evaluation tool is defined as (*Ferland et al.*, 2013):

$$CI = \frac{\sum_{k=1}^{2} \sum_{i \in C_k} \parallel \boldsymbol{x_i} - \bar{\boldsymbol{x}}^{(k)} \parallel^2}{\sum_{i=1}^{n} \parallel \boldsymbol{x_i} - \bar{\boldsymbol{x}} \parallel^2} \tag{3.10}$$

where $\bar{\boldsymbol{x}}^{(k)}$ represents the mean of the kth cluster for k = 1,2 and $\bar{\boldsymbol{x}}$ represents the overall mean. The CI provides a p-value for the significance of the cluster between these two clusters. For our clustering algorithm we used AgglomerativeClustering from *Pedregosa et al.* (2011). The Pearson Correlation Coefficient measures the significance of a correlation in a dataset (*Kirch*, 2008) and is defined as:

$$r = \frac{\sum (x_i - \bar{x})(y_i - \bar{y})}{\sqrt{\sum (x_i - \bar{x})^2 \sum (y_i - \bar{y})^2}} \tag{3.11}$$

where x_i and y_i are your data points and $\bar{x}$ and $\bar{y}$ are the respective means. We calculated each of these values for all of the plots shown in Fig. 3.6. However to determine whether or not these values could be calculated from random noise we generated 1000 sets of points with the same number of objects as our observation within the same region of g-r vs e, i, or H space and ran the same analysis on those sets. These results are shown in the inset histograms in Fig. 3.6. Note, for many of the combinations of orbital elements and colors, the clustering and/or correlation of the data are consistent with random noise. There are however a few which may be significant, including the correlation of e with g-r, the clustering/correlation of H with g-r, the clustering of H with r-i, and the clustering of e with r-z. These results suggest that while there may not be a correlation of color with inclination, there may be a correlation of color with e or H. However, it is clear that observation of more targets in the NT population are needed to confirm these results.

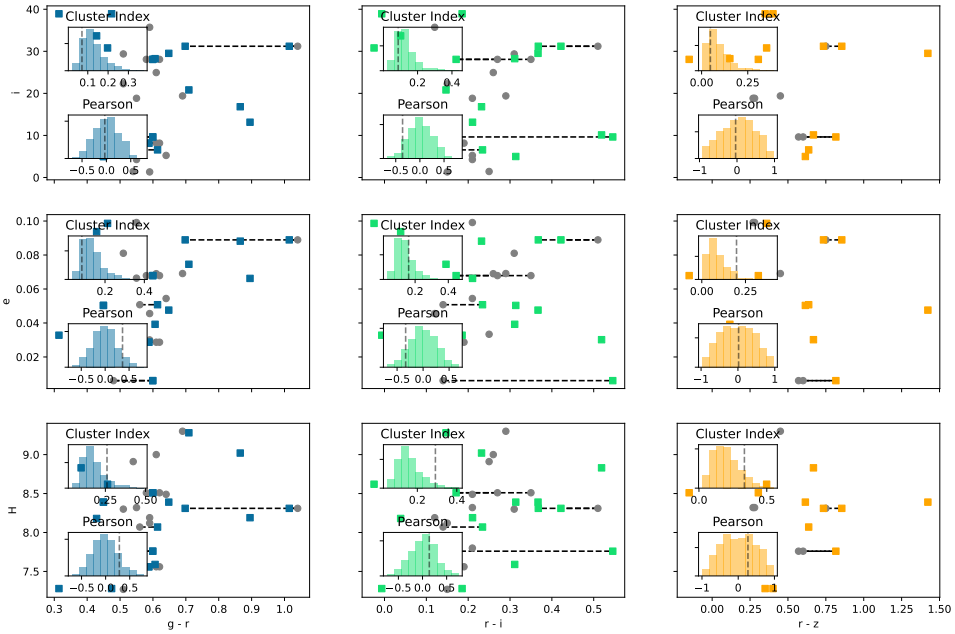

Figure 3.6: NT colors as a function of orbital elements (inclination on the top row, eccentricity on the middle row, and absolute magnitude on the bottom row). Grey points are taken from the literature (*Sheppard and Trujillo*, 2006; *Sheppard*, 2012; *Parker et al.*, 2013; *Jewitt*, 2018; *Lin et al.*, 2019; *Schwamb et al.*, 2019). Colored squares were measured in this paper. Duplicate observations of the same object are connected by dashed lines. The inset plots contain histograms of the Cluster Indices and Pearson Correlation Coefficients of a random distribution colors and orbital elements (see Sec. 3.5.1). Each grey dashed line in the inset plots shows the corresponding value calculated for the observed distribution.

3.5.2 Comparison to Other Populations

The ultimate goal of this work is to determine how similar the NT colors are to other populations in the Solar System. A simple statistical test to measure the likelihood that two distributions are drawn from the same underlying distribution is the Kolmogorov-Smirnov (KS) test (*Darling*, 1957). However, this test operates on 1-d data. Therefore to reduce the dimensions of our data, we performed a Principal Component Analysis (PCA) of our data, using the scikit-learn python package (*Pedregosa et al.*, 2011). Fig. 3.7 demonstrates that the PCA is able to successfully reduce the g-r vs. r-i color-color plot to a 1-d parameter that still distinguishes between the red and ultra-red populations of TNOs and the whole JT population (which is comprised of only red objects). The principal component value which separates these populations is 1.75 (shown as a dotted line in Fig. 3.7). We use this definition to classify our NT targets as red or ultra-red; the corresponding region in g-r vs r-i space is shown in Fig. 3.3 as a yellow shaded region. We then applied this PCA model to other populations in the Solar System, including JTs and previous observations of NTs, the results of which are shown in Fig. 3.8. By eye, the JT is clearly unique in that it is nearly devoid of any ultra-red members (i.e. targets with a principal component value >1.75). Also of note, about 25% of the NT targets presented in this paper occupy a unique region of PC1 <-1. This region corresponds to exceptionally blue objects that are not present in the other Solar System populations (see Sec. 3.5.3 for a more in-depth discussion of these objects).

We then ran a KS test for each combination of of these Solar System populations to determine the likelihood that they came from the same underlying distribution; the results of these tests are recorded in Table 3.2. Only two of these comparisons had statistically significant results (a p-value of 0.05 corresponding to a 95% confidence

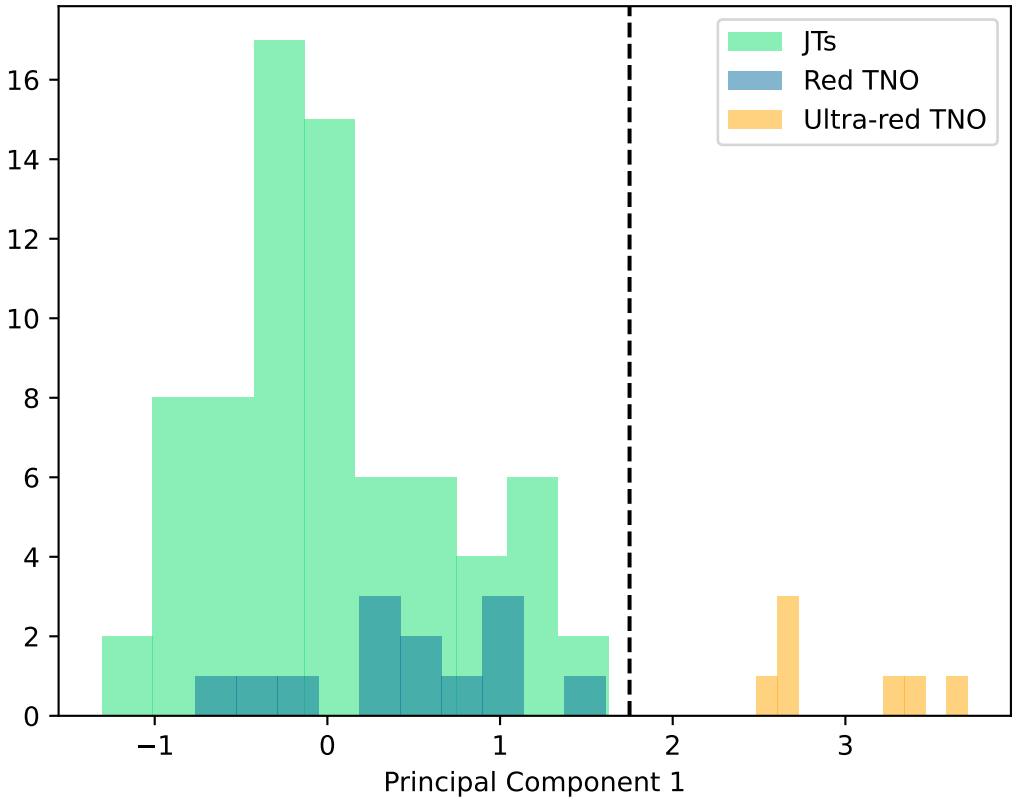

Figure 3.7: The results of running a Principal Component Analysis (PCA) with the g-r and r-i colors of certain Solar System populations. The green histogram corresponds to the JTs (taken from *Hainaut et al.* (2012)). The blue and orange histograms correspond to the red and ultra-red subpopulations of the scattered TNOs, taken from *Hainaut et al.* (2012); the classification of red vs ultra-red was determined by using a clustering algorithm (DBSCAN; *Pedregosa et al.* (2011)) which separated the TNOs into two sub-populations.

KS Test P-value	NTs (This Work)	NTs (Prev.)	TNOs	JTs
NTs (This Work)	1	0.465	0.449	0.032
NTs (Prev.)	0.465	1	0.109	0.180
TNOs	0.465	0.109	1	0.0002
JTs	0.032	0.180	0.0002	1

Table 3.2: The resulting p-values of the KS Test on each combination of subpopulations considered in this work.

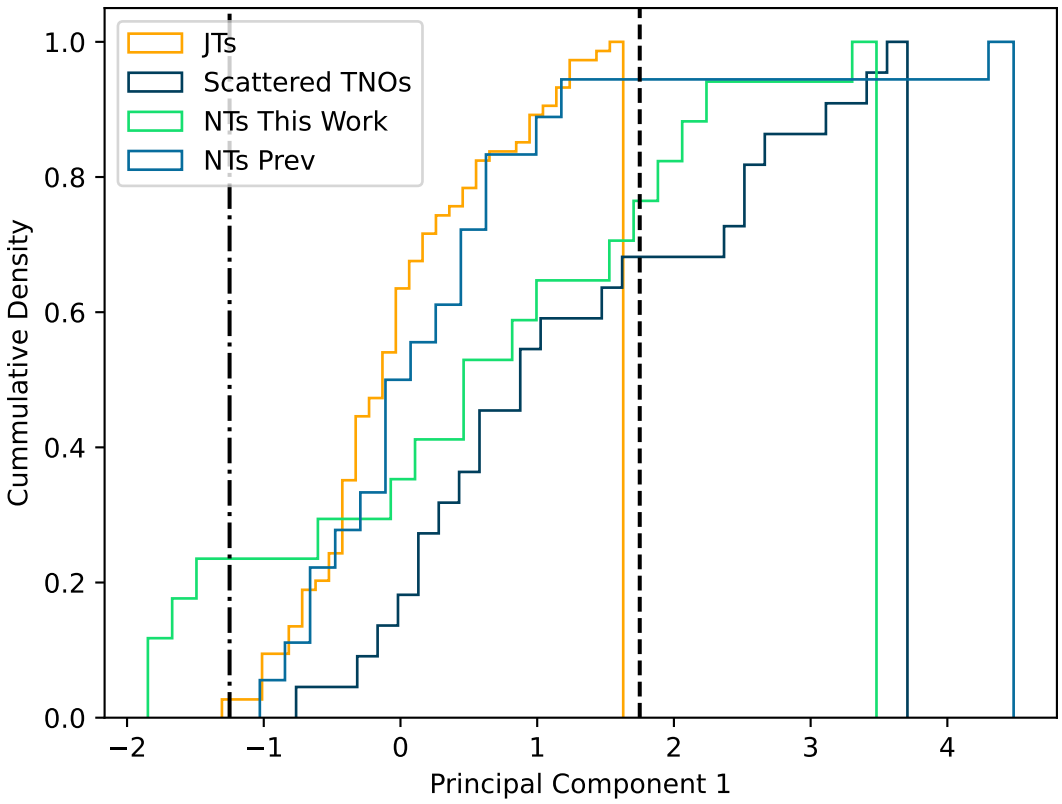

Figure 3.8: Cumulative distributions of the Principal Component (see Sec. 3.5.2) values of populations in the Solar System. The cut-off between red and ultra-red as defined by this PCA is shown as a black dashed line (see Fig. 3.7). The cut-off between red and blue objects is similarly shown as a dot-dashed line. The JT and scattered TNO results are shown as orange and navy histograms respectively. The NTs observations from previous literature are shown as a blue histogram. The NT observations from this work are shown as a green histogram.

level to reject the null hypothesis); we can conclude that the NT color distribution in this work and the TNO color distribution are distinct from that of the JTs. This result is expected since the JT population is devoid of ultra-red members. However, we cannot make any conclusions regarding whether the NTs and TNOs come from the same source population, other than that more photometric data is needed for each population.

3.5.3 Unique Targets

While most of our targets are consistent with previous color measurements, one object, 2011 SO_{277} is classified here as ultra-red while its previous observations place it firmly with in the red zone. Based on our other observations, we consider our results to be roughly consistent with previous literature (see Fig. 3.5), so this result is indeed unexpected. One explanation as to why this object has such different colors in independent observations is that its surface is not homogeneous. To test this hypothesis, a more in depth study of the rotational properties of the surface of this object is necessary, which will be upcoming in our next work on the lightcurves of NTs.

Three of our targets, 2014 SC_{375}, 2014 YB_{92}, and 2015 VU_{207}, are much bluer, nearly solar in color, as compered to the other NTs or KBOs. In fact, these objects are as blue as the bluest known asteroid, Phaetheon (*Tabeshian et al.*, 2019; *Lisse and Steckloff*, 2022). We can convert from UBVRcIc colors to SDSS colors using transformations from *Jester et al.* (2005) and assuming Rc-Ic < 1.15 and U-B < 0, resulting in g-r $= 0.5$ and r-i 0.04. Phaetheon's blue color has been attributed to thermal alteration and sublimative removal of Fe and refractory organics as it passes within 0.165AU from the sun (*Lisse and Steckloff*, 2022). NTs do not have perihelion distances < 25 AU, so the source of the blue material on these objects is not clear. It is possible that these targets originated elsewhere in the Solar System, but their

current orbits are stable for > Gyrs (see Sec. 3.3), implying that it was captured just after Neptune's migration. Future spectral observations would be necessary to reveal any compositional differences this target may have as compared to the rest of the NT population.

3.6 Discussion

3.6.1 Why were the ultra-red NTs rare before this work?

Prior to this work, the ultra-red NTs were very rare; none of the 13 NT samples in *Jewitt* (2018) are ultra-red NTs and pointing to the "Trojan Color Conundrum". Here we propose two possibilities to explain this inconsistency:

1. **Small number statistics:** Small number statistics could generate such a surprising result. If we assume a 4:1 apparent red to ultra-red ratio of NTs, the chance to randomly select 13 objects without picking up any ultra-red one is only about 5%. While it is not impossible, we should also consider alternative explanations.

2. **Selection effect:** Since bigger objects are easier to detect and obtain color measurements for, the 13 objects in *Jewitt* (2018) trend to be large; 10 of 13 have H $\leqslant$ 8. Moreover, many NTs have been discovered by deeper (*Lin et al.*, 2021) or wider (*Bernardinelli et al.*, 2022, 2020; *Lin et al.*, 2019) surveys since 2018, which included many high-inclination objects. Thus the *Jewitt* (2018) sample appears to be biased toward bigger sized and lower inclination objects. In fact, 8 of 13 NTs in the *Jewitt* (2018) sample have orbital inclination $< 10°$; 9 of the 31 currently known NTs have inclination $< 10°$, meaning that 8 of the 9 total low-inclination NTs were included in the *Jewitt* (2018) sample. According to the results of this work, the color distribution of NTs is likely related to their orbital elements (see Figure 3.6), which are also correlated to the size of

objects in the NT population (*Lin et al.*, 2021). Therefore, the likely color-orbit-size correlation in NT population could be at least partially explain why the "Trojan Color Conundrum" was observed, especially when there were some selection biases in that sample.

3.6.2 Possible explanation of the NT's color-orbit-size correlation

The orbit-size correlation in NT population has been proposed in (*Lin et al.*, 2021) to explain to the inconsistency of the orbital distributions of NT population obtained from the PS1 survey (*Lin et al.*, 2016) and the Outer Solar System Origins Survey (*Bannister et al.*, 2018, 2016, OSSOS). While the PS1 survey has well-known wide sky coverage (less biased in orbital inclination) but shallower survey depth, it discovered a large number of low-inclination and low-eccentricity NTs compared to the deeper but more ecliptic plane focused OSSOS, which was strongly biased in inclination and mostly discovered high inclination NTs. A two-component NT model has been proposed, which includes a cold (low-eccentricity, low-inclination) component containing mostly larger NTs ($H \lesssim 8$), and a hot component with high-inclination, high-eccentricity NTs, which does not have any restriction on the minimum object size. Such a model can create the apparent orbit-size correlation in the known NT population and explain the results from both surveys.

While this two component NT model is unusual, *Lin et al.* (2021) argued that it could still be formed from several scenarios. Here we review whether the proposed NT formation/evolution scenarios can be still valid with the newly found color-orbit-size correlation in this work:

1. **Formed as two components:** The currently known NT population could have more than one origin. *Lykawka et al.* (2009) proposed that current NTs were captured from the trans-Neptunian disc and also recaptured from the the pre-formed NT population, which were the objects with dynamically cold or-

bits around Neptune's L4 and L5 Lagrange points before the migration of the planets. In this scenario, the "pre-formed" population were closer to the Sun as Neptune was closer to the Sun before migration. Therefore, the pre-formed population would contain few ultra-red members, since the ultra-red surface could have been destroyed by solar radiation as *Jewitt* (2018) suggested. If the "pre-formed" population has a colder orbital distribution and the bigger size distribution than the trans-Neptunian population, the color-orbit-size correlation of current NT population would also form naturally.

2. **Formed as one component, evolved into two:** As we mention in Section 1.2, the NT-Plutino collision (*Almeida et al.*, 2009) could potentially resurface, as well as change the size distribution of the low-inclination NTs. However, it is not straightforward to explain the correlation between color and orbital eccentricity.

3. **A collisional NT family in low eccentricity/inclination orbital space:** If there is a NT collisional family in low-eccentricity, low-inclination space, the members would share very similar color and orbital elements to create the color-orbit correlation we observed in this work. Moreover, the collisional family may lack the small sized members like Haumea family (*Pike et al.*, 2020), resulting in the color-orbit-size correlation.

4. **There was a boundary between 30 − 40 au:** *Nesvorný et al.* (2020) proposed there is a red/ultra-red colored transition at between 30 to 40 au in trans-Neptunian disk. Such a two-colored disk would explain why most of the NT are red and rarely ultra-red. However, this scenario predicts a higher ultra-red/red ratio in low-inclination space, which is opposite to what we found in Figure 3.6. We note that the intrinsic red/ultra-red ratio is still unknown, since it can obtained from a characterized multi-color survey, such as the Dark Energy

Survey (*Bernardinelli et al.*, 2022, 2020) and the Vera C. Rubin Observatory's Legacy Survey of Space and Time (LSST). We also note that this scenario creates opposite color-orbit correlation and no color-size correlation. If it is valid, the inconsistency between *Jewitt* (2018) and this work (see section 5.1) can only be explained by the effect of small statistics.

Therefore, 3 of 4 above scenarios can create the apparent color-orbit-size correlation in NT population. There are several additional properties could help to constrain the formation/evolution scenarios of NT population. For example, if there is indeed a low eccentricity/inclination collisional NT family creating an ultra-red population exceeding that of the big, cold NTs, the same signature should not appear in the L5 NT population (unless there is another low eccentricity/inclination collisional NT family in L5 cloud).

Beside the symmetric/asymmetric between L4 and L5 clouds, the rotation properties could be another useful signature to further constrain the suggested scenarios, since formation/evolution mechanisms would affect the rotation rate of the minor planets. *Thirouin and Sheppard* (2019) and *Thirouin et al.* (2016) compared the rotation properties of cold-classical objects and Haumea family members to other TNOs, respectively, and found that in general, the Haumea family member rotate faster than the TNOs, and the TNOs rotate faster than the cold-classical objects. Therefore we have also obtained the light curves of seven NTs, the analysis and results of which will be presented in the following paper in this series: *Photometric Survey of Neptune's Trojan Asteroids II: The Rotational Properties.*

3.7 Conclusions

In this paper, we measure the griz colors for 15 of the 24 known NTs, including 10 targets with no previous color observations. We used the IMACS f/4 instrument

on the 6.5m Baade telescope with Sloan g'r'i'z' filters to conduct our photometric survey. We confirm that 2013 VX_{30} is ultra-red in color, and identify three NTs identified as ultra-red for this first time in this study. This result brings the red to ultra-red ratio of NTs to 7.75:1, much more consistent with the corresponding TNO ratio and resolving the "Trojan Color Conundrum". We also find three targets which are bluer than solar in color, the origin of which is unclear; the most likely explanation is that these objects originated from the inner solar system. For the entire NT population, we find that NTs that are ultra-red in $g - r$ have a higher eccentricities and larger sizes, though more observations of this population are needed to confirm this correlation. The explanation behind this correlation, remains an open question that is difficult to address with current data. While our 15 targets make up a nearly a majority of the known NT population, we only observe seven with inclination $< 20°$, eight with eccentricity ≤ 0.05, and five with $H < 8$. Thus, while we do observe a color-orbit-size distribution, specifically low eccentricity and large population missing ultra-red objects, our result is still well within the realm of small number statistics. More discoveries of NTs (especially around L5) are clearly needed. The L5 point has historically been difficult to study due to its overlap with the galactic plane, but the NT L5 region is moving away from this high stellar density region, making now the perfect time to start studying this population. The true degree of asymmetry between the L4 and L5 clouds will be an important to distinguishing different formation scenarios for the NT population. Moreover, our ongoing work to measure the rotational period and specific composition of these small bodies directly will be vital to understanding the true origin of the NT population.

CHAPTER IV

The First Near-IR Spectroscopy Survey of Neptune Trojans with JWST

4.1 Introduction

Trojan asteroids, which librate around a planet's L4 or L5 point, are sometimes referred to as fossils from the early Solar System as they are thought to be remnants of our primordial disk. Specifically, Trojans can have orbits which are stable on order the age of the Solar System due to the strength of the 1:1 resonance with its planet (*Lykawka et al.*, 2011; *Malhotra and Jeongahn*, 2011; *Ćuk et al.*, 2012; *Gomes and Nesvorný*, 2016b). Moreover, this resonance relationship means that Trojans are also tied to the evolution of their planet. This link is particularly important for the giant planets, which may have migrated toward or away from the Sun significantly. If a planet migrates, the Lagrangian regions follow, transforming the original population (*Kortenkamp et al.*, 2004). Thus, current day Trojan properties can also be used to constrain evolutionary models, which should be able to explain and/or recreate them. (*Nesvorný et al.*, 2013; *Parker*, 2015; *Gomes and Nesvorný*, 2016b; *Nesvorný et al.*, 2018). This also means that Trojan asteroids associated with the giant planets are not thought to have formed *in-situ*. Rather, these populations likely grew through capture of planetesimals during the epoch of planetary migration. Such migration

would have occurred in the first several hundred Myr in the history of the Solar System, so they still are remnants of the very early Solar System. Therefore, the physical characteristics of Trojan populations can provide a window to the early Solar System.

If the Neptune Trojan population (NT) did not form *in-situ*, they are likely planetismals captured from elsewhere in the primordial disk, with the most likely source population being the nearby Kuiper Belt. If that were the case, one would expect Kuiper Belt Objects (KBOs) and NTs to be similar in size and color. The bimodality of red ($g - r < 0.75$) vs. ultra-red ($g - r > 0.75$) KBOs has been well established (*Sheppard*, 2010; *Schwarz et al.*, 2011; *Hainaut et al.*, 2012; *Peixinho et al.*, 2012; *Sheppard*, 2012; *Lacerda et al.*, 2014; *Peixinho et al.*, 2015; *Pike et al.*, 2017b; *Wong and Brown*, 2017b; *Schwamb et al.*, 2019). Additionally, the centaur population, small bodies which orbit between Jupiter and Neptune, are thought to be fed by planetesimals escaping the NT region (*Horner and Lykawka*, 2010). These objects are also red/ultra-red in color (*Peixinho et al.*, 2012, 2015). Through 2018, no ultra-red NTs had been found, making their color distribution distinctly different than their expected origins or offshoots (*Jewitt*, 2018). Since then, five ultra-red NTs have been found, and the current red to ultra-red ratio is now in line with the KBO population (*Lin et al.*, 2019; *Markwardt et al.*, submitted). A color-size-orbit correlation has been found, but the origin of the color bimodality in NTs is not clear in that context. The population could have started as two components or evolved from one into two (*Markwardt et al.*, submitted). There may also have been a primordial red/ultra-red boundary at 30 - 40 AU that was mixed during planetary migration into our current day NT and KBO populations (*Nesvorný et al.*, 2020). Finally, the presence of a collisional family in the NT population which skews the color-size-orbit correlation cannot be ruled out (*Markwardt et al.*, submitted).

While it is clear that colors of NTs are tied to the Solar System's formation and

evolution, they are a limited tool for understanding the history and composition of the surfaces of these objects. The limitation is in part due to interplay between independent processes that can all transform the surface of the icy/rocky bodies, including radiation from the solar wind, galactic cosmic rays, charged particles in magnetospheres, ice lines, heating resurfacing events, and collisions (*Bennett et al.*, 2013). In general, we expect that these bodies were originally blue/neutral due to the ices covering their surface, then these surfaces become red in color over time due to irradiation. However, impacts can "re-blue" the surface by bringing fresh icy material beneath the irradiation crust back to the surface (*Luu and Jewitt*, 1996). This model can explain a diversity in observed colors, but there are complications, such as the fact that cosmic rays could penetrate to a deep layer on TNOs requiring collisions to be larger to re-blue the surface (*Gil-Hutton*, 2002). Moreover, even though ices should normally be colorless, even a relatively small amount of carbonaceous minerals mixed with these ices can darken/color theses surfaces (*Cruikshank et al.*, 2019). In short, a variety of processes and compositions can affect the surfaces of planetary bodies, and colors alone are often not sufficient to disentangle the degeneracies between them.

Fortunately, we can get more information to distinguish these scenarios through near-IR spectroscopy. Near-IR bands (3-5 microns) are especially useful for observing planetary surfaces as many broad molecular absorption features occur at these wavelengths. While some compositions may have similar optical/VNIR spectra, they are easily distinguishable with measurements at wavelengths > 3 microns, meaning that it is possible to measure and distinguish volatile species and complex organics on the surfaces of small bodies through reflectance spectroscopy (*Parker et al.*, 2016). Water ice also has multiple distinct absorption bands in the near-IR, the depth and location of which can be used to measure further surface properties such as grain size and ice phase *Clark and Lucey* (1984); *Cruikshank et al.* (2019). Additionally, ice irradiation products have absorption features in the near-IR that have already been identified on

the surfaces of other small bodies through ground based observation (*Brown et al.*, 2015).

Unfortunately, study of the surfaces of KBOs has been limited to the brightest objects that can be observed with ground-based observations (*Dalle Ore et al.*, 2009; *Delsanti et al.*, 2010; *Clark et al.*, 2012; *Brown et al.*, 2015; *Seccull et al.*, 2021; *Merlin et al.*, 2017, & references therein). With V-band magnitudes between $\sim$ 21.5 to 25 (see Table 4.1), NTs are well beyond the cabilites of most ground-based observatories. The only observatory currently powerful enough to target NTs is the recently launched JWST. In this paper we present the first near-IR spectra taken of a subset of the NT population, observed with JWST.

The structure of this paper is as follows: Section 2 describes the design of our spectroscopic survey. Section 3 outlines our data reduction process. Section 4 presents the results of our survey. Section 5 discuss the meaning of our results. Section 6 is conclusions drawn from these results.

4.2 Survey Design

The goal of this project is to measure the near-IR spectra of several NTs to identify surface ice features and compare them based on L4 vs L5, red vs ultra-red, and stability. Our target list is shown in Table 4.1, and includes 2013 VX_{30}, the first ultra-red NT discovered. Our target list also spans both Lagrange points to look for any (a)symmetries between those two populations. We also cover a variety of orbital stabilities (*Lin et al.*, 2021, 2022), to compare objects that were captured just after planetary migration to those that were captured later and must have originated elsewhere in the Solar System. Specific targets were chosen based on total exposure time contraints for this program while still representing all of the described populations.

We chose to use the NIRSpec IFU instrument on JWST to conduct our spectroscopic survey, due to its wavelength coverage, field of view (FOV), and low resolution

capabilites. As stated previously (see Sec. 4.1), the wavelength coverage of NIRSpec (0.5 - 5 microns) is ideal for measuring near-IR absorption bands of common materials on the surfaces of outer Solar System objects. We also chose to use the IFU for these observations rather than the one of the fixed slits due to its larger field of view. With the 3σ pointing uncertainty of JWST (0.3") and the positional uncertainty of our objects (see Table 4.1), it would have been very difficult to accurately place the target within the slits. Therefore, we instead opted for blind pointing in the IFU aperture, which requires the uncertainty only be less than 1.5". We conducted a photometric survey on the Magellan 6.5m Baade Telescope located at Las Campanas Observatory, Chile to constrain the orbits of our targets to an uncertainty within the FOV (for results of photometric survey see Chapter III). Finally, our observations are of broad absorption features so we did not require high resolution to meet our goals; therefore, we utilized the PRSIM mode on the instrument to maximize SNR. We used the *NRSIRS2RAPID* readout mode to improve performance and sensitivity in long exposure IFU observations of our faint targets. We opted for a large (0.5") 4 point dither for our background extraction. The 4 point dither pattern was chosen of a 2 point nod for additional redundancy against detector defects and MSA light leakage that can contaminate the IFU spectrum, as well as to provide improved spatial sampling. We were able to use the large pattern by re-observing our targets to derive smaller positional uncertainties.

4.3 Data Analysis

The JWST NIRSpec instrument is capable of spectroscopy from 0.6 to 5.3 μm through various different apertures, including a micro-shutter array, long-slits, and an integral field unit (IFU). The IFU has been, and will continue to be throughout the lifetime of the mission, the workhorse for observations of solar system minor bodies. The 3" x 3" field of view is primarily used to obtain spatial information of extended

Table 4.1: NT Spectroscopic Survey Targets

Name	L4/L5	Stability	Ave. V-band Mag.	Color Classification	Total Obs. Time
2008 LC_{18}	L5	meta-stable	23.5	red	4.8 hrs
2001 WG_{157}	L4	stable	22.3	red	2.0 hrs
2013 KY_{18}	L5	transient	21.7	red	2.0 hrs
2011 HM_{102}	L5	stable	23.1	red	3.4 hrs
2013 VX_{30}	L4	stable	22.8	ultra-red	2.2 hrs
2006 RJ_{103}	L4	stable	22.5	red	2.0 hrs
2007 VL_{305}	L4	stable	22.8	red	2.4 hrs
2011 SO_{277}	L4	stable	22.6	red	2.4 hrs
2010 TS_{191}	L4	meta-stable	22.9	red	2.9 hrs

targets, but is also useful for minor bodies, which are almost always point sources. Some minor bodies have positional uncertainties large enough to prevent accurate placement in a long-slit with a width of 0.2" or 0.4" without target acquisition; others have satellites that can be observed simultaneously without having to calculate a slit orientation, should the satellite's ephemeris be known to high enough precision.

The IFU operates by slicing the field of view vertically into 30 virtual slitlets, each with a width of 0.1", using an optical element. Each slitlet is dispersed onto one or both of the NIRSpec detectors using either a grating or a prism, producing the equivalent of 30 long-slit spectra. The JWST calibration pipeline takes the resulting 2D image and resamples them spatially and spectrally into a 3D data cube with two spatial dimensions and a spectral dimension.

Extraction of the target spectrum from the 3D data cube is best treated as photometry within each wavelength slice (i.e., within each image of the data cube). Aperture photometry can be used but increases the noise in the resulting spectrum; the better option is to perform PSF-fitting at each wavelength. The latest version of WebbPSF (v1.1.1) includes updates from commissioning, but still does not account for broadening effects produced by the individual instruments. This results in PSFs that are too thin and are therefore unusable as models. Instead, we use empirical PSFs constructed from the data itself in a process referred to as "template PSF fit-

ting" (Ian Wong, personal communication). A moving median is computed using the 5 wavelength slices shortward and longward of the currently considered slice, for a total of 11 slices; this also reduces variations in the background. The PSF "template" is normalized by the sum of the flux within the image. The template is used as the model with two parameters: an additional background offset and a flux scaling factor. The best-fit parameters are determined by minimizing the χ^2 of the residual (data minus model) using a Nelder-Mead downhill simplex algorithm (also known as the amoeba fitting routine; Press et al., 2007). Finally, the median background is subtracted from the template and the flux within an aperture 3 pixels in radius is extracted from the template image multiplied by the best-fit flux scaling factor (with no background included). This process is performed at each wavelength to extract the full 1D spectrum; for slices close to the short- or long-wavelength ends, less than 11 total slices are used to create the template, resulting in slightly higher noise in these regions. The 1D spectra from all dithers are then median-combined and the resulting spectrum is divided by a G-type star to remove the solar contribution.

4.4 Results

Note, data has not been taken for all of our targets, but we still have significant results for the current subset. That subset includes 2007 VL_{305}, 2010 TS_{191}, 2011 SO_{277}, 2011 WG_{157}, and 2013 VX_{30}. Of note, this dataset does not include any L5 NTs, but it does include the first ultra-red NT, 2013 VX_{30}, allowing us to compare the near-IR spectra of red vs. ultra-red NTs. The resulting spectra for each of the red targets is shown in Fig. 4.1. These spectra look relatively similar, each displaying a strong 3.1 peak associated with water ice and a CO_2 absorption feature at 4.25 μm (see Fig. 4.2). One outlier exists amongst this group, 2011 SO_{277}; this object has by far the strongest 3.1 μm water ice feature as well as having the steepest spectral slope from 1 - 2 μm (it also has the steepest spectral slope at optical wavelengths,

see Chapter III). This result may indicate that objects with a steeper slope at optical wavelengths corresponding to more abundant water ice on the surface. However, with only 4 targets we are well within the realm of small-number statistics and observations of additional outer Solar System targets (such as *Stansberry et al.* (2017); *Hines et al.* (2017); *Lunine* (2017)) are needed to see if this correlation holds. All of these spectra also look remarkably similar to that of Iapetus exhibiting a double-peaked feature at 3.1 μm, a broad water ice feature from 3.5 - 5 μm, and a narrow CO_2 absorption feature at 4.25 μm; Iapetus has also been identified to be covered with water and CO_2 ice (*Clark et al.*, 2012). This result demonstrates a consistency in surface composition across the outer Solar System.

Since all of the red NTs have a relatively similar composition we have averaged them together to increase SNR and compare the mean to the ultra-red NT (see Fig. 4.2). Clearly, $2013VX30$ has a spectrum unique from the average red spectrum, with the best fit synthetic spectrum being the one with Tholins. Tholins are expected to be reddening agents on the surfaces of icy bodies, so this seems to explain why $2013VX_{30}$ is ultra-red. However, some ice may still be visible on the surface as there is another very strong CO_2 line. This result may point to inhomogeneities on the red crust, but to confirm this one would need to look for temporal spectral variations as the object rotates, which is beyond the scope of this paper.

4.5 Discussion

The main result of this paper, based on the subset of data which has been taken, is that red and ultra-red surfaces do have distinguishable compositions. In particular, while red NTs are covered in H_2O and CO_2 ice, ultra-red NTs are covered in Tholins. Tholins are a complex organic, black tar-like substance that's formed when cosmogonically abundant molecules or ices, such as CO_2 and H_2O ice, is irradiated, say by the Sun (*Sagan and Khare*, 1979; *Khare et al.*, 1989). There are several explanations

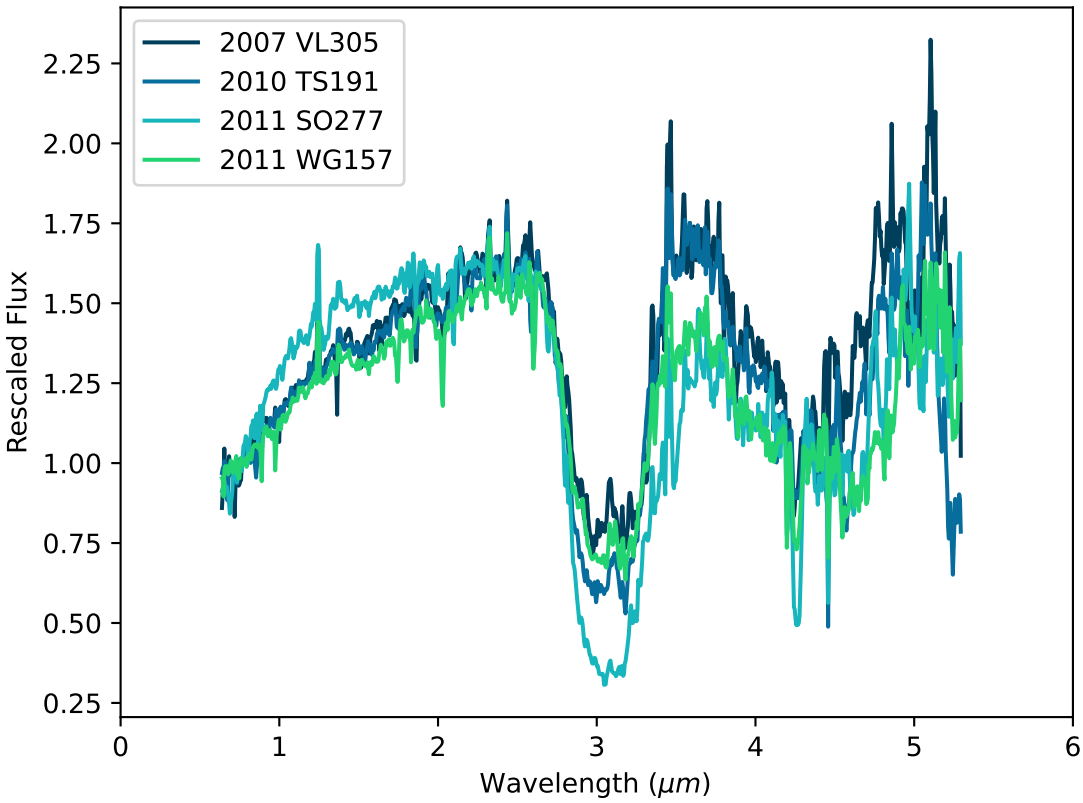

Figure 4.1: NIRSpec spectra of red NT targets. The flux has been renormalized in this plot to be equal to 1 at wavelength = 1 μm. Each target's spectrum is shown as a various shade of blue.

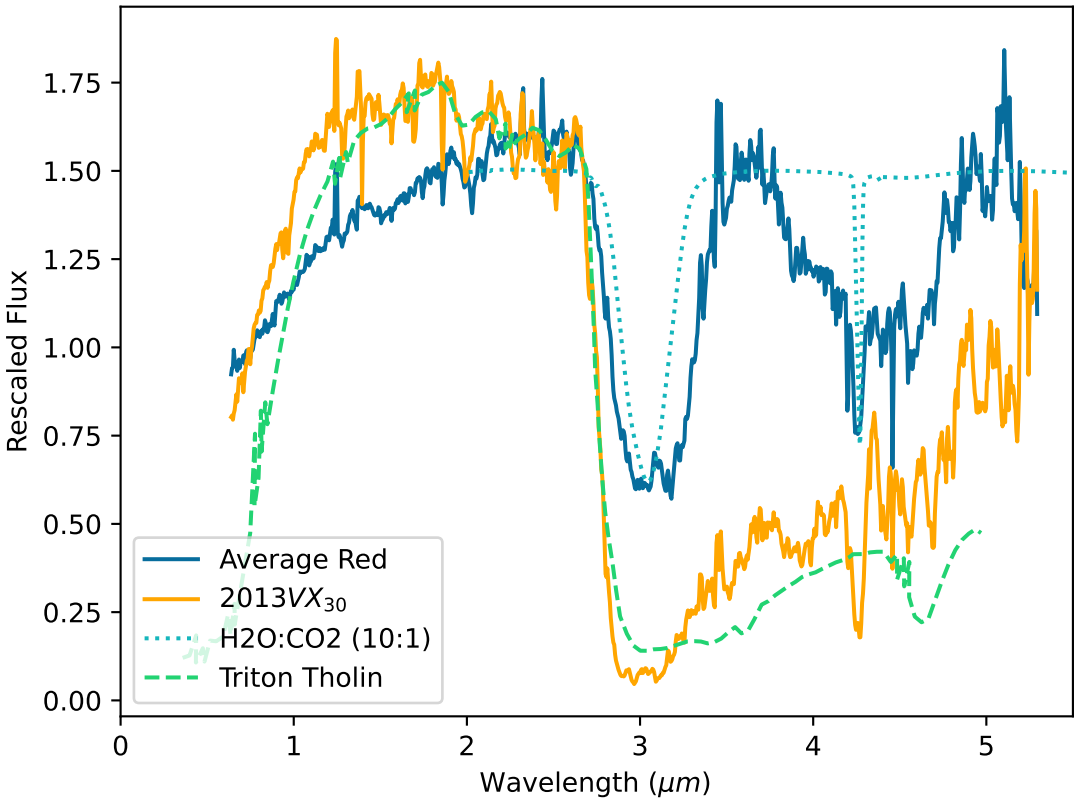

Figure 4.2: NIRSpec spectra of ultra-red NT and all the red NTs averaged together. The flux has been renormalized in this plot to be equal to 1 at wavelength = 1 μm. The H_2O:CO_2 (10:1) spectrum is from the Leiden Ice Database for Astrochemistry (https://icedb.strw.leidenuniv.nl/), meaning we are comparing to an experimental dataset. The tholin spectrum is a synthetic spectrum taken from *Fernández-Valenzuela et al.* (2021).

as to why we observe two compositionally distinct groups of NTs.

- Perhaps the simplest explanation is that these two compositional groups come from two distinct source populations. Each group could have its distinct starting composition and chemical evolution due to forming at different locations in the Solar System. These two populations could have been subsequently mixed during planetary migration. In this way, the differences between the two populations would be primordial. If there is a sharp distinction between the two populations this may also explain the bimodality in color observed.

- Since irradiation of H_2O and CO_2 can create Tholins, red objects may turn into ultra-red over time given enough enough exposure to the Sun. In this case the differences between populations would be due to differences in irradiation. However, with NTs all having the same orbital distance with the same level of solar exposure, it is not clear why some would be more irradiated than others.

- Finally, if these objects are from the same source and experience the same levels of irradiation, their differences could be due to collisions on the surface. *Luu and Jewitt* (1996) have shown that Tholins may only form a thin layer on the surface, and collisions can bring the underlying ice back to the surface. In this way, we can explain the similarity in composition, both have CO_2 ice, and the differences, each object is at a varying stage of irradiation or impacts. This hypotheses may explain why a high-inclination NT is ultra-red as it would be more likely to avoid Plutino collisions that would reblue the surface. However, in this scenario one would expect a smooth transition between optical color where each object is at a unique state, rather than the bimodality we observe. One explanation could be that this transition occurred over a short timescale resulting in a bimodality.

4.6 Conclusions

In this paper, we conducted the first near-IR spectroscopic survey of NTs using NIRSpec on JWST. So far we find that most of our targets are covered in H_2O and CO_2 ice, as has been observed on other small bodies. The one exception is $2013VX_{30}$, whose reflectance spectrum is a more consistent with surface covered in Tholins, organic material created when such ices are subject to irradiation. These results indicate that the bimodality in color for NTs is supported by differing surface compositions. However, there are multiple explanations as to the origin of these two populations. Distinguishing these scenarios would give us insight as to the history of our Solar System, but more information is needed. For example, do all ultra-red NTs look similar, just as with the reds? Now that more ultra-red NTs have been identified (see Chapter III), follow up spectral observations of these targets are needed.

Since we are still waiting for all of our data to be taken, we have not met all of our science goals yet. For example, we are still waiting on our L5 target data which allow us to compare the L4/L5 populations. Comparing the NT results to similar TNO surveys taken with NIRSpec JWST, will also reveal what ties exist between NTs and their presumed source population, but the results from the TNO surveys are not public yet. Thus, this paper should be viewed as a very preliminary pass at the data, and we anticipate doing a more sophisticated spectral fitting method than was shown here. In short, more science is yet to come and we are not finished with this dataset yet.

CHAPTER V

Conclusions

5.1 Science Results

In this thesis, I presented work that addressed the topics of formation and evolution of Trojan asteroids throughout the Solar System. Specifically, there are two main science themes: Earth Trojans (ETs) and their size distribution and the surface composition of Neptune Trojans (NTs). The ET size distribution gives us an idea as to what the primordial ET population might be like with regards to how many and of what size. The surface composition of NTs tells us about the epoch of planetary migration and how objects were scattered throughout the Solar System.

5.1.1 ET Size Distribution

In Chapter II, we found no new ET candidates, but were able to place the most stringent upper limits on the population at the time. We found that no ETs greater than $\sim$1.5km in size exist, or they would have already been discovered. However, our upper limits suggest that there could still be hundreds left at a few hundred m in size. Recent results suggest there should be no primordial ETs (especially small ones), but observational constraints are not sensitive to the smallest targets. Until deeper observations are taken and can rule out the existence of any primordial ETs, which theories are correct remains an open question.

5.1.2 NT Surface composition

The surface composition of a NT can be inferred/measured through photometry/reflectance spectroscopy. In Chapter III, I presented results from a photometric survey of 17 out of 31 NTs. We identified four new ultra-red NTs bringing the red to ultra-red ratio to 6.2:1, resolving the "Trojan Color Conundrum". We also find that there is a color-orbit-size correlation, though the explanation as to why is an open question. We consider a two-component model, in which one is dynamically cold but comprised of physically larger members and the other is dynamically hot with no restrictions on minimum object size. This model could arise if NTs formed as two distinct components, formed as one component but then evolved into two, have a collisonal family with low inclinations and eccentricities, or there was a color boundary between 30 - 40 AU. Determining the true degree of asymmetry between the L4 and L5 points should reveal if there collisonal family dominating one of the populations. Any rotational differences between the two populations should reveal the differences in their collisonal history. However, this preliminary result will be tested as more NTs are discovered and characterized, resolving whether there are real differences or this is a result of small number statistics.

Colors are a important though limited tool for understanding the surface composition of NTs, and I have improved on the photometric survey with a near-IR spectroscopic survey using JWST. Due to the numerous molecular bands of ices in the near-IR, reflectance spectroscopy can be used to measure the specific composition of our targets. We find that red NTs have surfaces consistent with being covered in H_2O and CO_2 ice, while the ultra-red one is consistent with a tholin dominated spectrum. This result shows that there are indeed compositional differences based on optical color. As far as why there are two distinct color/spectral populations, the answer is unclear. Again, these groups may have originated from two distinct populations, or they may come from the same population but each group has a distinct

irradiation/collisonal history. However, if the latter was the case, we would not necessarily expect specifically two bimodal populations. Follow up observations of the other ultra-red NTs will be necessary to understanding this problem.

5.2 Future Work

This thesis has studied Trojans asteroids throughout the Solar System from an astronomical context, but there is still much upcoming work left to do. As mentioned before, this field is about to become inundated with discoveries of small bodies in an LSST era. Depending on the amount of time given to twilight surveys, this could drastically change the census of Trojan asteroids throughout the Solar System. It will be up to the small bodies astronomy community to study these populations in greater detail to identify the most intriguing members that may be candidates for missions. This follow-up will be made easier with the latest astronomical facilities, such as JWST.

With OSIRIS-REx, Hayabusa2, and Lucy, there is a demonstrated interest across the world in studying small bodies through missions, so with the discoveries of new, interesting targets, follow-up missions to study and sample these objects directly may drive more missions to this part of the Solar System. Even with just the current missions, we can anticipate exciting results to come out within the next few years. Hayabusa2 recently successfully completed it sample return and preliminary analysis of those samples has already been done (*Yada et al.*, 2021). OSIRIS-REx was able to successfully obtain a sample from the surface of Bennu and is expected to return to Earth with this sample in 2023. Finally, Lucy, the Jupiter Trojan asteroid mission, recently launched in 2021 and expected to have its first small body flyby in 2025. All of this is to say that the study of small bodies, and Trojan asteroids in particular, will be a rich field for years to come.

However, what can we actually expect to learn in the upcoming years about Trojan

asteroids? It depends on which population you are asking about. In this final section, I will outline some future projects or ideas that relate to each sub-population and outline what more we expect to learn about each.

5.2.1 Earth Trojans

In truth, the study of ETs seems to actually be winding down. Numerous studies have introduced problems regarding the actual stability of this population which explain the lack of ET discoveries (*Zhou et al.*, 2018; *Napier et al.*, 2022). With there being numerous null detections, whether a primordial ET population actually exists remains unclear. Depending on if LSST conducts a portion of their observations during twilight, this survey could easily settle this question.

However, our group still has an extensive dataset to search for any L5 ETs, even temporarily captured objects. This dataset covers 60 sq deg on the sky towards the ET L5 point. This survey also utilizes a shift-and-stack algorithm to reach a depth of H $\sim$ 21.5, as deep as the previous deep pencil-beam survey of the L5 point (*Whiteley and Tholen*, 1998). One non-detection with this survey would be able to rule out any objects $\sim$ 400m in size, which begins to overlap with the limits set by the Yarkovsky effect (*Zhou et al.*, 2018). In short, a non-detection with this survey would rule out all but the smallest of primordial ETs. Analysis of this dataset is currently underway. Understanding the nature of this population will inform our understanding of the dynamical history of the region near Earth.

5.2.2 Neptune Trojans

In this thesis, we present the exciting result that NTs with different optical colors do indeed have different compositions that seem to be tied to the irradiation and collisional history of the population. However, there is still much left to be learned about NTs. As previously mentioned, while we now know that red NTs are all

very similar in composition, we still do not know if all ultra-red NTs are similar in composition. With new ultra-red NTs having been identified (see Chapter III), there are new targets that need follow-up spectral observations. Since these objects are all relatively faint, the most likely tool to do this project would be JWST. This follow-up would be key to our understanding of the meaning of optical colors and the bi-modality observed in them, which would drive our understanding of the composition of our primordial disk and how that can be altered over time.

However, there is still much work to be done even before follow-up. It has been suggested that the NT population may even be larger than the JT population (*Lin et al.*, 2019), yet we have found orders of magnitude fewer NTs that JTs. In short, it is currently unclear what the true population and distribution of NTs is like. Unfortunately, the NT population is more difficult to study than JTs. NTs are further away and thus fainter, and, for Earth-based studies, the L5 point has overlapped with the galactic plane for the past years, meaning the search fields have been incredibly crowded. However, the L5 point is currently leaving the galactic plane making now the perfect time to revisit the population. Our group has over 7 nights using DECam on the Blanco 4m telescope to study this region. We will be using a shift-and-stack algorithm to increase the depth of our survey. Analysis of this dataset is currently underway. We expect to find between 5 and 18 new NTs with this survey which would double to quintuple the known NT population. Color follow-up of these targets will also be vital towards measuring a first approximation of their surface composition.

5.2.3 Mars Trojans

The enigma of MTs is their composition, with most of them being covered in olivine, a substance not common in the Solar System. But are these objects only covered in olivine? The obvious answer to that question is to look with JWST. Many minerals and molecules have clear absorption features that are blocked from

the ground atmospheric absorption. Also, no spectral observation has been taken of these objects beyond $\sim$2.5 μm. JWST observations would be able to confirm the presence of olivine on the surface as well as identify any other significant minerals and molecules on the surface of these objects. Olivine also exhibits a change in spectral slope ("reddening") based on how irradiated it has been (*Loeffler et al.*, 2009). Therefore, such observations could also be used to measure the degree of irradiation of these surfaces to see how fresh they are which would give an indication as to their age. Knowing the age would allow us to pin down the origin of these objects. Are they primordially made of olivine or are these objects remnants of a collision that dredged up mantle material from Mars? Did the Eureka family start as one object that was broken up by the YORP effect? Comparing the compositions of MTs to each other will give us a hint as to their history. Similarly, what is the other MT made of? Does it look like other asteroids in the Solar System? Comparing the olivine to non-olivine MTs will allow us to compare the histories of these objects. In short, reflectance spectroscopy, particularly in the near-IR, is key to understanding the surfaces of these small bodies. MTs seem to look strange based off current observations, and they deserve another look with JWST.

5.2.4 Jupiter Trojans

The future prospects are perhaps brightest for the JTs, as Lucy is currently on its way toward 7 JT targets. Lucy is the first mission to visit any Trojan population, and it will undoubtedly revolutionize our understanding of these small bodies. The goals of Lucy are to measure surface geology, surface composition, interiors and bulk properties, and to look for satellites and rings. All of these mesaurements are key to understanding the formation and evolution of our Solar System. Surface composition will give us a window into the composition *throughout* the primordial disk, as JTs are expected to have been scattered from multiple other regions of the Solar System.

Surface geology and interiors will tell us the age of the surface and history of cratering as well as internal structure of the entire asteroid. Looking for satellites will also give us an idea of how these bodies formed. Taken all together, Lucy will allow us to understand the geology and chemistry of Trojan asteroids to a greater detail than ever before. The first flyby of a JT will happen in 2025, so we can expect this field to explode in the coming years. To go from first discovery of a JT to a flyby mission is an incredible feat in 120 years, and bodes well for the future of this field.

APPENDICES

APPENDIX A

Search for L5 Earth Trojans with DECam: Survey Pointings

Table A.1: First Half of Survey Pointings. Columns: (1) Name of the Field. There were 8 distinct fields in this survey, observed 8 times each; (2) RA of exposure center (hours); (3) Dec of exposure center (degrees); (4) Start time of exposure (UTC). Every exposure was taken on 2018-06-16.

Field	RA	Dec	Time
ET_0	148.2684	13.71537	22:45:35
ET_0	148.2686	13.71430	22:46:18
ET_1	146.8672	12.61325	22:47:02
ET_1	146.8663	12.61278	22:47:45
ET_2	148.6678	11.91204	22:48:28
ET_2	148.6661	11.91206	22:49:11
ET_3	150.0658	13.21204	22:49:54
ET_3	150.0649	13.21155	22:50:36
ET_4	151.8663	12.61203	22:51:19
ET_4	151.8647	12.61239	22:52:03
ET_5	150.4654	11.31283	22:52:46
ET_5	150.4657	11.31343	22:53:29
ET_6	152.2671	10.71340	22:54:12
ET_6	152.2659	10.71455	22:54:56
ET_7	153.6655	12.01450	22:55:38
ET_7	153.6665	12.01432	22:56:20
ET_0	148.2658	13.71357	22:57:16
ET_0	148.2666	13.71279	22:58:00
ET_1	146.8659	12.61219	22:58:46
ET_1	146.8652	12.61255	22:59:29
ET_2	148.6659	11.91192	23:00:11
ET_2	148.6661	11.91251	23:00:53
ET_3	150.0671	13.21225	23:01:40
ET_3	150.0665	13.21313	23:02:23
ET_4	151.8678	12.61350	23:03:06
ET_4	151.8686	12.61258	23:03:50
ET_5	150.4693	11.31235	23:04:32
ET_5	150.4683	11.31208	23:05:15
ET_6	152.2692	10.71229	23:05:57
ET_6	152.2691	10.71294	23:06:40
ET_7	153.6702	12.01269	23:07:22
ET_7	153.6697	12.01314	23:08:04

Table A.2: Second Half of Survey Pointings. Columns: (1) Name of the Field. There were 8 distinct fields in this survey, observed 8 times each; (2) RA of exposure center (hours); (3) Dec of exposure center (degrees); (4) Start time of exposure (UTC). Every exposure was taken on 2018-06-16.

Field	RA	Dec	Time
ET_0	148.2691	13.71246	23:08:59
ET_0	148.2682	13.71292	23:09:41
ET_1	146.8680	12.61210	23:10:24
ET_1	146.8683	12.61332	23:11:07
ET_2	148.6696	11.91296	23:11:49
ET_2	148.6698	11.91222	23:12:33
ET_3	150.0690	13.21317	23:13:16
ET_3	150.0684	13.21276	23:13:58
ET_4	151.8679	12.61339	23:14:41
ET_4	151.8673	12.61308	23:15:23
ET_5	150.4674	11.31342	23:16:05
ET_5	150.4680	11.31393	23:16:47
ET_6	152.2689	10.71375	23:17:29
ET_6	152.2697	10.71322	23:18:12
ET_7	153.6695	12.01254	23:18:53
ET_7	153.6707	12.01305	23:19:37
ET_0	148.2691	13.71227	23:20:34
ET_0	148.2684	13.71222	23:21:17
ET_1	146.8683	12.61170	23:21:59
ET_1	146.8674	12.61258	23:22:43
ET_2	148.6676	11.91242	23:23:25
ET_2	148.6669	11.91336	23:24:08
ET_3	150.0660	13.21263	23:24:52
ET_3	150.0669	13.21335	23:25:35
ET_4	151.8677	12.61336	23:26:17
ET_4	151.8668	12.61394	23:27:01
ET_5	150.4666	11.31324	23:27:43
ET_5	150.4675	11.31401	23:28:26
ET_6	152.2673	10.71314	23:29:09
ET_6	152.2673	10.71354	23:29:51
ET_7	153.6683	12.01315	23:30:34
ET_7	153.6688	12.01308	23:31:16

APPENDIX B

Search for L5 Earth Trojans with DECam: Calculating Upper Limits Under Different Assumptions of the ET Population

B.1 Calculating Upper Limits Under Different Assumptions of the ET Population

In Sec. 2.6.3, we calculated various upper limits on the ET population, which required making several assumption about the population, namely its physical extent and size distribution. Under different assumptions the calculated upper limits could deviate from what was presented here. Therefore, we aim to provide enough information such that the reader could calculate upper limits based on our observations but under their own assumptions.

We calculated upper limits from our recovery rates using Eq. 2.7. This equation depends on our calculated recovery rates and our assumed survey coverage of the L5 cloud. We determined this coverage to be 24% based on our synthetic population (see Sec. 2.6.1). However, these upper limits may be calculated with a different coverage

value but the same measured values of the recovery rates. These values appear in Fig. 2.9, but we include them explicitly here in B.1.

We also assume that the ET H/size distribution follows a power law (Eq. 2.5) in order to calculate even more stringent upper limits on the ET population, particularly for bright/large objects. We performed the extrapolation using the non-cumulative power law distribution normalized to the upper limit we calculated for our point of extrapolation:

$$N(H) = \frac{U(H_e)}{10^{\alpha H_e}} * 10^{\alpha H} \tag{B.1}$$

where H is the absolute magnitude, H_e is the extrapolation point, $U(H_e)$ is the upper limit calculated at that extrapolation point, and α is a slope parameter. In Sec. 2.6.3, we use $H_e = 19.7$, $U(H_e) = 18$, and $\alpha = 0.46$ for H ¡ 20.39 and $\alpha = 0.7$ for H ¿ 20.39. However, this method may still be used for different assumptions of slope values, extrapolation points, or other functional forms of the ET H distribution given our calculated upper limit at the H bin used for extrapolation; these values appear in Fig. 2.10, but we include them explicitly here in B.1.

Table B.1: Values needed to calculate ET upper limits. Columns: (1) H bin; (2) Recovery rate of injected Earth Trojans (see Sec. 2.6.2, 2.6.3) such that 1 = 100% of objects were recovered. If this column contains a dashed line, there were no injected objects in that H bin.; (3) Calculated upper limit without extrapolation for the number of ETs in each H bin (see Sec. 2.6.3). If this column contains a dashed line, there were no injected objects in that H bin, so we could not calculate an upper limit.

H	R(H)	U(H)
15.11	0.40	31.54
15.33	- - -	- - -
15.55	1.00	12.62
15.77	- - -	- - -
15.99	0.33	37.85
16.21	- - -	- - -
16.43	1.00	12.62
16.65	0.50	25.23
16.87	0.67	18.92
17.09	0.83	15.14
17.31	0.89	14.19
17.53	0.67	18.92
17.75	0.80	15.77
17.97	0.90	14.02
18.19	0.94	13.36
18.41	0.75	16.82
18.63	0.91	13.92
18.85	0.77	16.33
19.07	0.84	14.94
19.29	0.62	20.19
19.51	0.76	16.68
19.73	0.71	17.73
19.95	0.53	24.01
20.17	0.31	40.27
20.39	0.13	97.15

BIBLIOGRAPHY

BIBLIOGRAPHY

Alexandersen, M., B. Gladman, S. Greenstreet, J. J. Kavelaars, J.-M. Petit, and S. Gwyn (2013), A Uranian Trojan and the Frequency of Temporary Giant-Planet Co-Orbitals, *Science*, *341*(6149), 994–997, doi:10.1126/science.1238072.

Allen, R. L., G. M. Bernstein, and R. Malhotra (2001), The Edge of the Solar System, *ApJ*, *549*(2), L241–L244, doi:10.1086/319165.

Almeida, A. J. C., N. Peixinho, and A. C. M. Correia (2009), Astrophysics Neptune Trojans and Plutinos: colors, sizes, dynamics, and their possible collisions, *A&A*, *508*, 1021–1030, doi:10.1051/0004-6361/200911943.

Alvarez-Candal, A., et al. (2014), Stellar occultation by (119951) 2002 KX_{14} on April 26, 2012, *A&A*, *571*, A48, doi:10.1051/0004-6361/201424648.

Astropy Collaboration, et al. (2013), Astropy: A community Python package for astronomy, *A&A*, *558*, A33, doi:10.1051/0004-6361/201322068.

Astropy Collaboration, et al. (2018), The Astropy Project: Building an Open-science Project and Status of the v2.0 Core Package, *AJ*, *156*, 123, doi:10.3847/1538-3881/aabc4f.

Bannister, M. T., et al. (2016), The Outer Solar System Origins Survey. I. Design and First-quarter Discoveries, *AJ*, *152*(3), 70, doi:10.3847/0004-6256/152/3/70.

Bannister, M. T., et al. (2018), OSSOS. VII. 800+ Trans-Neptunian Objects—The Complete Data Release, *ApJS*, *236*(1), 18, doi:10.3847/1538-4365/aab77a.

Bendinelli, O., G. Parmeggiani, F. Zavatti, and S. Djorgovski (1990), Seeing Deconvolution of Globular Clusters in M31, *AJ*, *99*, 774, doi:10.1086/115373.

Bennett, C. J., C. Pirim, and T. M. Orlando (2013), Space-Weathering of Solar System Bodies: A Laboratory Perspective, *Chemical Reviews*, *113*(12), 9086–9150, doi:10.1021/cr400153k.

Bernardinelli, P. H., et al. (2020), Trans-Neptunian Objects Found in the First Four Years of the Dark Energy Survey, *ApJS*, *247*(1), 32, doi:10.3847/1538-4365/ab6bd8.

Bernardinelli, P. H., et al. (2022), A Search of the Full Six Years of the Dark Energy Survey for Outer Solar System Objects, *ApJS*, *258*(2), 41, doi:10.3847/1538-4365/ac3914.

Bernstein, G. M., D. E. Trilling, R. L. Allen, M. E. Brown, M. Holman, and R. Malhotra (2004), The Size Distribution of Trans-Neptunian Bodies, *AJ*, *128*(3), 1364–1390, doi:10.1086/422919.

Berthier, J., F. Vachier, W. Thuillot, P. Fernique, F. Ochsenbein, F. Genova, V. Lainey, and J.-E. Arlot (2006), SkyBoT, a new VO service to identify Solar System objects, in *Astronomical Data Analysis Software and Systems XV*, *Astronomical Society of the Pacific Conference Series*, vol. 351, edited by C. Gabriel, C. Arviset, D. Ponz, and S. Enrique, p. 367.

Berthier, J., et al. (2020), Physical characterization of double asteroid (617) Patroclus from 2007/2012 mutual events observations, , *352*, 113990, doi:10.1016/j.icarus.2020.113990.

Bertin, E., and S. Arnouts (1996), SExtractor: Software for source extraction., *A&AS*, *117*, 393–404, doi:10.1051/aas:1996164.

Borisov, G., A. Christou, S. Bagnulo, A. Cellino, T. Kwiatkowski, and A. Dell'Oro (2017), The olivine-dominated composition of the Eureka family of Mars Trojan asteroids, *MNRAS*, *466*(1), 489–495, doi:10.1093/mnras/stw3075.

Borisov, G., A. A. Christou, F. Colas, S. Bagnulo, A. Cellino, and A. Dell'Oro (2018), (121514) 1999 UJ_7: A primitive, slow-rotating Martian Trojan, *A&A*, *618*, A178, doi:10.1051/0004-6361/201732466.

Bottke, W. F., R. Jedicke, M. Alessandro, J.-M. Petit, and B. Gladman (2000), Understanding the distribution of near-earth asteroids, *Science*, *288*(5474), 2190–2194, doi:10.1126/science.288.5474.2190.

Bottke, W. F., D. D. Durda, D. Nesvorný, R. Jedicke, A. Morbidelli, D. Vokrouhlický, and H. Levison (2005), The fossilized size distribution of the main asteroid belt, *Icarus*, *175*(1), 111 – 140, doi:https://doi.org/10.1016/j.icarus.2004.10.026.

Bowell, E., B. Hapke, D. Domingue, K. Lumme, J. Peltoniemi, and A. W. Harris (1989), Application of photometric models to asteroids., in *Asteroids II*, edited by R. P. Binzel, T. Gehrels, and M. S. Matthews, pp. 524–556.

Brown, M. E. (2016), The 3-4 μm Spectra of Jupiter Trojan Asteroids, *AJ*, *152*(6), 159, doi:10.3847/0004-6256/152/6/159.

Brown, M. E., and B. J. Butler (2017), The Density of Mid-sized Kuiper Belt Objects from ALMA Thermal Observations, *AJ*, *154*(1), 19, doi:10.3847/1538-3881/aa6346.

Brown, M. E., and E. L. Schaller (2007), The mass of dwarf planet eris, *Science*, *316*, 1585 – 1585.

Brown, M. E., E. L. Schaller, and G. A. Blake (2015), Irradiation Products On Dwarf Planet Makemake, *AJ*, *149*(3), 105, doi:10.1088/0004-6256/149/3/105.

Brown, M. E., et al. (2021), JWST observations of Lucy mission targets, JWST Proposal. Cycle 1, ID. #2574.

Brown, R., and J. Firth (2016), Analysis of trans-neptunian objects and a proposed theory to explain their origin, *Monthly Notices of the Royal Astronomical Society*, *456*, 1587–1594, doi:10.1093/mnras/stv2818.

Buie, M. W., et al. (2015), Size and Shape from Stellar Occultation Observations of the Double Jupiter Trojan Patroclus and Menoetius, *AJ*, *149*(3), 113, doi:10.1088/0004-6256/149/3/113.

Bus, S. J. (1999), Compositional structure in the asteroid belt: Results of a spectroscopic survey, Ph.D. thesis, Massachusetts Institute of Technology.

Cambioni, S., et al. (2018), AN UPPER LIMIT ON EARTH'S TROJAN ASTEROID POPULATION FROM OSIRIS-REX, in *49th Lunar and Planetary Science Conference*, p. No. 2083.

Cellino, A., V. ZappalÃ, and P. Farinella (1989), Asteroid shapes and lightcurve morphology, *Icarus*, *78*(2), 298–310, doi:https://doi.org/10.1016/0019-1035(89)90178-4.

Christou, A. (2019), Earth's missing Trojans: Lessons from Mars and the role of radiation forces, in *AAS/Division of Dynamical Astronomy Meeting*, *AAS/Division of Dynamical Astronomy Meeting*, vol. 51, p. 100.06.

Christou, A. A. (2013), Orbital clustering of martian Trojans: An asteroid family in the inner Solar System?, , *224*(1), 144–153, doi:10.1016/j.icarus.2013.02.013.

Christou, A. A., G. Borisov, A. Dell'Oro, S. A. Jacobson, A. Cellino, and E. Unda-Sanzana (2020), Population control of Mars Trojans by the Yarkovsky & YORP effects, , *335*, 113370, doi:10.1016/j.icarus.2019.07.004.

Clark, R. N., and P. G. Lucey (1984), Spectral properties of ice-particulate mixtures and implications for remote sensing. 1. Intimate mixtures., *J. Geophys. Res.*, *89*, 6341–6348, doi:10.1029/JB089iB07p06341.

Clark, R. N., et al. (2012), The surface composition of iapetus: Mapping results from cassini vims, *Icarus*, *218*(2), 831–860, doi:https://doi.org/10.1016/j.icarus.2012.01.008.

Connors, M., P. Wiegert, and C. Veillet (2011), Earth-Trojan asteroid, *Nature*, *475*(7357), 481–483, doi:10.1038/nature10233.

Cruikshank, D. P., L. V. Moroz, and R. N. Clark (2019), *Spectroscopy of Ices, Volatiles, and Organics in the Visible and Infrared Regions*, pp. 102–119, doi:10.1017/9781316888872.007.

Ćuk, M., D. P. Hamilton, and M. J. Holman (2012), Long-term stability of horseshoe orbits, *Monthly Notices of the Royal Astronomical Society*, *426*(4), 3051–3056, doi:10.1111/j.1365-2966.2012.21964.x.

Dalle Ore, C. M., et al. (2009), Composition of KBO (50000) Quaoar, *A&A*, *501*(1), 349–357, doi:10.1051/0004-6361/200911752.

Darling, D. A. (1957), The kolmogorov-smirnov, cramer-von mises tests, *The Annals of Mathematical Statistics*, *28*(4), 823–838.

de la Fuente Marcos, C., and R. de la Fuente Marcos (2014), Asteroid 2013 ND15: Trojan companion to Venus, PHA to the Earth, *Monthly Notices of the Royal Astronomical Society*, *439*(3), 2970–2977, doi:10.1093/mnras/stu152.

de la Fuente Marcos, C., and R. de la Fuente Marcos (2017), Asteroid 2014 YX49: a large transient Trojan of Uranus, *Monthly Notices of the Royal Astronomical Society*, *467*(2), 1561–1568, doi:10.1093/mnras/stx197.

Delbo, M., M. Mueller, J. P. Emery, B. Rozitis, and M. T. Capria (2015), Asteroid Thermophysical Modeling, in *Asteroids IV*, pp. 107–128, doi:$10.2458/\mathrm{azu}_{u}apress_{9}780816532131 - ch006$.

DellaGiustina, D. N., et al. (2020), Variations in color and reflectance on the surface of asteroid (101955) Bennu, *Science*, *370*(6517), eabc3660, doi:10.1126/science.abc3660.

Delsanti, A., F. Merlin, A. Guilbert-Lepoutre, J. Bauer, B. Yang, and K. J. Meech (2010), Methane, ammonia, and their irradiation products at the surface of an intermediate-size KBO?. A portrait of Plutino (90482) Orcus, *A&A*, *520*, A40, doi:10.1051/0004-6361/201014296.

DeMeo, F. E., and B. Carry (2014), Solar System evolution from compositional mapping of the asteroid belt, *Nature*, *505*(7485), 629–634, doi:10.1038/nature12908.

DeMeo, F. E., R. P. Binzel, S. M. Slivan, and S. J. Bus (2009), An extension of the Bus asteroid taxonomy into the near-infrared, , *202*(1), 160–180, doi:10.1016/j.icarus.2009.02.005.

DeMeo, F. E., D. Polishook, B. Carry, B. J. Burt, H. H. Hsieh, R. P. Binzel, N. A. Moskovitz, and T. H. Burbine (2019), Olivine-dominated A-type asteroids in the main belt: Distribution, abundance and relation to families, , *322*, 13–30, doi:10.1016/j.icarus.2018.12.016.

DeSouza, S. R., F. Roig, and D. Nesvorný (2021), Can a jumping-Jupiter trigger the Moon's formation impact?, *MNRAS*, *507*(1), 539–547, doi:10.1093/mnras/stab2188.

Di Sisto, R. P., A. Brunini, L. D. Dirani, and R. B. Orellana (2005), Hilda asteroids among Jupiter family comets, , *174*(1), 81–89, doi:10.1016/j.icarus.2004.10.024.

Dvorak, R., C. Lhotka, and L. Zhou (2012), The orbit of 2010 TK7. Possible regions of stability for other Earth Trojan asteroids, *A&A*, *541*, 127, doi:10.1051/0004-6361/201118374.

Emery, J. P., D. M. Burr, and D. P. Cruikshank (2011), Near-infrared Spectroscopy of Trojan Asteroids: Evidence for Two Compositional Groups, *AJ*, *141*(1), 25, doi:10.1088/0004-6256/141/1/25.

Emery, J. P., F. Marzari, A. Morbidelli, L. M. French, and T. Grav (2015), The Complex History of Trojan Asteroids, in *Asteroids IV*, pp. 203–220, doi:$10.2458/\mathrm{azu}_u apress_9 780816532131 - ch011$.

Fenucci, M., and B. Novaković (2021), The Role of the Yarkovsky Effect in the Long-term Dynamics of Asteroid (469219) Kamo'oalewa, *AJ*, *162*(6), 227, doi:10.3847/1538-3881/ac2902.

Ferland, G. J., R. L. Porter, P. A. M. van Hoof, R. J. R. Williams, N. P. Abel, M. L. Lykins, G. Shaw, W. J. Henney, and P. C. Stancil (2013), The 2013 Release of Cloudy, , *49*, 137–163.

Fernández, J. A. (2003), Long-period comets and the oort cloud, in *Cometary Science after Hale-Bopp*, edited by H. Boehnhardt, M. Combi, M. R. Kidger, and R. Schulz, pp. 325–343, Springer Netherlands, Dordrecht.

Fernández, Y. R., S. S. Sheppard, and D. C. Jewitt (2003), The Albedo Distribution of Jovian Trojan Asteroids, *AJ*, *126*(3), 1563–1574, doi:10.1086/377015.

Fernández-Valenzuela, E., et al. (2021), Compositional Study of Trans-Neptunian Objects at λ ¿ 2.2 μm, , *2*(1), 10, doi:10.3847/PSJ/abc34e.

Flaugher, B., et al. (2015), THE DARK ENERGY CAMERA, *The Astronomical Journal*, *150*(5), 150, doi:10.1088/0004-6256/150/5/150.

Fornasier, S., E. Dotto, O. Hainaut, F. Marzari, H. Boehnhardt, F. De Luise, and M. A. Barucci (2007), Visible spectroscopic and photometric survey of Jupiter Trojans: Final results on dynamical families, , *190*(2), 622–642, doi:10.1016/j.icarus.2007.03.033.

Fraser, W. C., M. E. Brown, A. Morbidelli, A. Parker, and K. Batygin (2014), The Absolute Magnitude Distribution of Kuiper Belt Objects, *ApJ*, *782*(2), 100, doi:10.1088/0004-637X/782/2/100.

Gallant, J., B. Gladman, and M. Ćuk (2009), Current bombardment of the Earth-Moon system: Emphasis on cratering asymmetries, *Icarus*, *202*(2), 371–382, doi:10.1016/j.icarus.2009.03.025.

Galushina, T. Y., and O. N. Letner (2020), Influence of the Yarkovsky Effect on Motion of Asteroids with Small Perihelion Distance, *Russian Physics Journal*, *63*(1), 71–78, doi:10.1007/s11182-020-02004-8.

Gaspar, H. S., O. C. Winter, and E. Vieira Neto (2017), The asteroid belt outer region under jumping-Jupiter migration, *MNRAS*, *470*(3), 2680–2686, doi:10.1093/mnras/stx1218.

Gerdes, D. W., et al. (2017), Discovery and Physical Characterization of a Large Scattered Disk Object at 92 au, *ApJ*, *839*(1), L15, doi:10.3847/2041-8213/aa64d8.

Gil-Hutton, R. (2002), Color diversity among Kuiper belt objects: The collisional resurfacing model revisited, *Planet. Space Sci.*, *50*(1), 57–62, doi:10.1016/S0032-0633(01)00073-3.

Gladman, B., and J. J. Kavelaars (1997), Kuiper Belt searches from the Palomar 5-m telescope., *A&A*, *317*, L35–L38.

Gladman, B., et al. (2012), The Resonant Trans-Neptunian Populations, *AJ*, *144*(1), 23, doi:10.1088/0004-6256/144/1/23.

Gomes, R., and D. Nesvorný (2016a), Neptune trojan formation during planetary instability and migration, *A&A*, *592*, A146, doi:10.1051/0004-6361/201527757.

Gomes, R., and D. Nesvorný (2016b), Neptune trojan formation during planetary instability and migration, *A&A*, *592*, A146, doi:10.1051/0004-6361/201527757.

Grav, T., A. K. Mainzer, J. M. Bauer, J. R. Masiero, and C. R. Nugent (2012), WISE/NEOWISE Observations of the Jovian Trojan Population: Taxonomy, *ApJ*, *759*(1), 49, doi:10.1088/0004-637X/759/1/49.

Grav, T., et al. (2011), WISE/NEOWISE Observations of the Jovian Trojans: Preliminary Results, *ApJ*, *742*(1), 40, doi:10.1088/0004-637X/742/1/40.

Greenberg, A. H., and J.-L. Margot (2015), Improved algorithms for radar-based reconstruction of asteroid shapes, *The Astronomical Journal*, *150*(4), 114, doi:10.1088/0004-6256/150/4/114.

Greenstreet, S., B. Gladman, and H. Ngo (2020), Transient Jupiter Co-orbitals from Solar System Sources, *AJ*, *160*(3), 144, doi:10.3847/1538-3881/aba2c9.

Grundy, W., et al. (2019), Mutual orbit orientations of transneptunian binaries, *Icarus*, *334*, 62–78, doi:https://doi.org/10.1016/j.icarus.2019.03.035, the Trans-Neptunian Solar System.

Guilbert-Lepoutre, A., and P. Ferruit (2017), Surface composition of mid-sized TNOs: searching for ammonia, JWST Proposal. Cycle 1, ID. #1231.

Hainaut, O. R., and A. C. Delsanti (2002), Colors of Minor Bodies in the Outer Solar System. A statistical analysis, *A&A*, *389*, 641–664, doi:10.1051/0004-6361:20020431.

Hainaut, O. R., H. Boehnhardt, and S. Protopapa (2012), Colours of minor bodies in the outer solar system. II. A statistical analysis revisited, *A&A*, *546*, A115, doi:10.1051/0004-6361/201219566.

Harris, A. W., and G. D'Abramo (2015), The population of near-earth asteroids, *Icarus*, *257*, 302 – 312, doi:https://doi.org/10.1016/j.icarus.2015.05.004.

Harris, A. W., and A. W. Harris (1997), On the Revision of Radiometric Albedos and Diameters of Asteroids, , *126*(2), 450–454, doi:10.1006/icar.1996.5664.

Hasegawa, S., M. Marsset, F. E. DeMeo, S. J. Bus, J. Geem, M. Ishiguro, M. Im, D. Kuroda, and P. Vernazza (2021), Discovery of Two TNO-like Bodies in the Asteroid Belt, *ApJ*, *916*(1), L6, doi:10.3847/2041-8213/ac0f05.

Heinze, A. N., S. Metchev, and J. Trollo (2015), Digital Tracking Observations Can Discover Asteroids 10 Times Fainter Than Conventional Searches, *AJ*, *150*(4), 125, doi:10.1088/0004-6256/150/4/125.

Hestroffer, D., et al. (2019), Small Solar System Bodies as granular media, *A&A Rev.*, *27*(1), 6, doi:10.1007/s00159-019-0117-5.

Hines, D. C., B. J. Holler, M. M. Mueller, and G. Wright (2017), Kuiper Belt Science with JWST, JWST Proposal. Cycle 1, ID. #1272.

Horner, J., and P. S. Lykawka (2010), The Neptune Trojans - a new source for the Centaurs?, *MNRAS*, *402*(1), 13–20, doi:10.1111/j.1365-2966.2009.15702.x.

Horner, J., and P. S. Lykawka (2012), 2004 KV_{18}: a visitor from the scattered disc to the Neptune Trojan population, *MNRAS*, *426*(1), 159–166, doi:10.1111/j.1365-2966.2012.21717.x.

Horner, J., et al. (2020), Solar system physics for exoplanet research, *Publications of the Astronomical Society of the Pacific*, *132*(1016), 102,001, doi:10.1088/1538-3873/ab8eb9.

Huang, Y., B. Gladman, M. Beaudoin, and K. Zhang (2022), A Rogue Planet Helps to Populate the Distant Kuiper Belt, *ApJ*, *938*(2), L23, doi:10.3847/2041-8213/ac9480.

Hui, M.-T., P. A. Wiegert, D. J. Tholen, and D. Föhring (2021), The Second Earth Trojan 2020 XL_5, *ApJ*, *922*(2), L25, doi:10.3847/2041-8213/ac37bf.

Ito, T., and R. Malhotra (2010), Asymmetric Impacts of Near-Earth Asteroids on the Moon, *Astronomy & Astrophysics*, *519*, A63, doi:10.1051/0004-6361/200912901.

Ivezić, Ž., et al. (2001), Solar system objects observed in the sloan digital sky survey commissioning data, *The Astronomical Journal*, *122*(5), 2749–2784, doi:10.1086/323452.

Jedicke, R., and T. Metcalfe (1998), The orbital and absolute magnitude distributions of main belt asteroids, *Icarus*, *131*(2), 245 – 260, doi:https://doi.org/10.1006/icar.1997.5876.

JeongAhn, Y., and R. Malhotra (2010), Co-orbital Asteroids of Earth as Candidates for Asymmetric Impactors on the Moon, in *American Astronomical Society, DPS meeting #42*, pp. Vol. 42, 1053, Bulletin of the American Astronomical Society.

JeongAhn, Y., and R. Malhotra (2015), The current impact flux on mars and its seasonal variation, *Icarus*, *262*, 140 – 153, doi:https://doi.org/10.1016/j.icarus.2015.08.032.

Jester, S., et al. (2005), The sloan digital sky survey view of the palomar-green bright quasar survey, *The Astronomical Journal*, *130*(3), 873–895, doi:10.1086/432466.

Jewitt, D. (2018), The Trojan Color Conundrum, *AJ*, *155*(2), 56, doi:10.3847/1538-3881/aaa1a4.

Jewitt, D., and K. J. Meech (1986), Cometary Grain Scattering versus Wavelength, or, "What Color Is Comet Dust?", *ApJ*, *310*, 937, doi:10.1086/164745.

Jewitt, D. C. (2002), From Kuiper Belt Object to Cometary Nucleus: The Missing Ultrared Matter, *AJ*, *123*(2), 1039–1049, doi:10.1086/338692.

Johnston, R. (2022).

Jutzi, M., and E. Asphaug (2015), The shape and structure of cometary nuclei as a result of low-velocity accretion, *Science*, *348*(6241), 1355–1358, doi:10.1126/science.aaa4747.

Jutzi, M., and W. Benz (2017), Formation of bi-lobed shapes by sub-catastrophic collisions. A late origin of comet 67P's structure, *A&A*, *597*, A62, doi:10.1051/0004-6361/201628964.

Karlsson, O. (2004), Transitional and temporary objects in the Jupiter Trojan area, *A&A*, *413*, 1153–1161, doi:10.1051/0004-6361:20031543.

Khare, B. N., W. R. Thompson, C. F. Chyba, E. T. Arakawa, and C. Sagan (1989), Organic solids produced from simple C/H/O/N ices by charged particles: Applications to the outer solar system, *Advances in Space Research*, *9*(2), 41–53, doi:10.1016/0273-1177(89)90362-1.

Kirch, W. (Ed.) (2008), *Pearson's Correlation Coefficient*, pp. 1090–1091, Springer Netherlands, Dordrecht, doi:10.1007/978-1-4020-5614-7$_2$569.

Kortenkamp, S. J., R. Malhotra, and T. Michtchenko (2004), Survival of Trojan-type companions of Neptune during primordial planet migration, , *167*(2), 347–359, doi:10.1016/j.icarus.2003.09.021.

Lacerda, P., et al. (2014), The Albedo-Color Diversity of Transneptunian Objects, *ApJ*, *793*(1), L2, doi:10.1088/2041-8205/793/1/L2.

Lawler, S. M., et al. (2019), OSSOS. XIII. Fossilized Resonant Dropouts Tentatively Confirm Neptune's Migration Was Grainy and Slow, *AJ*, *157*(6), 253, doi:10.3847/1538-3881/ab1c4c.

Leiva, R., et al. (2020), Stellar Occultation by the Resonant Trans-Neptunian Object (523764) 2014 WC510 Reveals a Close Binary TNO, , *1*(2), 48, doi: 10.3847/PSJ/abb23d.

Lim, L. F., J. P. Emery, M. Mueller, A. S. Rivkin, D. Trilling, and B. J. Burt (2011), Olivine Composition of the Mars Trojan 5261 Eureka: Spitzer IRS Data, in *EPSC-DPS Joint Meeting 2011*, vol. 2011, p. 1199.

Lin, H.-W., L. Markwardt, K. J. Napier, F. C. Adams, and D. W. Gerdes (2022), Long-term Stability of Six Neptunian Trojans, *Research Notes of the American Astronomical Society*, *6*(4), 79, doi:10.3847/2515-5172/ac6752.

Lin, H. W., et al. (2016), The Pan-STARRS 1 Discoveries of Five New Neptune Trojans, *AJ*, *152*(5), 147, doi:10.3847/0004-6256/152/5/147.

Lin, H. W., et al. (2019), Evidence for color dichotomy in the primordial neptunian trojan population, *Icarus*, *321*, 426 – 435, doi: https://doi.org/10.1016/j.icarus.2018.12.006.

Lin, H. W., et al. (2021), OSSOS: The eccentricity and inclination distributions of the stable Neptunian Trojans, , *361*, 114391, doi:10.1016/j.icarus.2021.114391.

Lisse, C., and J. Steckloff (2022), Thermal alteration and differential sublimation can create phaethon's "rock comet" activity and blue color, *Icarus*, *381*, 114,995, doi: https://doi.org/10.1016/j.icarus.2022.114995.

Loeffler, M. J., C. A. Dukes, and R. A. Baragiola (2009), Irradiation of olivine by 4 keV He^+: Simulation of space weathering by the solar wind, *Journal of Geophysical Research (Planets)*, *114*(E3), E03003, doi:10.1029/2008JE003249.

Lunine, J. I. (2017), Kuiper Belt Science with JWST, JWST Proposal. Cycle 1, ID. #1273.

Luu, J., and D. Jewitt (1996), Color Diversity Among the Centaurs and Kuiper Belt Objects, *AJ*, *112*, 2310, doi:10.1086/118184.

Lykawka, P. S., and J. Horner (2010), The capture of Trojan asteroids by the giant planets during planetary migration, *MNRAS*, *405*(2), 1375–1383, doi:10.1111/j.1365-2966.2010.16538.x.

Lykawka, P. S., J. Horner, B. W. Jones, and T. Mukai (2009), Origin and dynamical evolution of Neptune Trojans - I. Formation and planetary migration, *MNRAS*, *398*(4), 1715–1729, doi:10.1111/j.1365-2966.2009.15243.x.

Lykawka, P. S., J. Horner, B. W. Jones, and T. Mukai (2011), Origin and dynamical evolution of Neptune Trojans - II. Long-term evolution, *MNRAS*, *412*(1), 537–550, doi:10.1111/j.1365-2966.2010.17936.x.

Magnier, E. A., et al. (2013), The Pan-STARRS 1 Photometric Reference Ladder, Release 12.01, *ApJS*, *205*(2), 20, doi:10.1088/0067-0049/205/2/20.

Mainzer, A., et al. (2012), CHARACTERIZING SUBPOPULATIONS WITHIN THE NEAR-EARTH OBJECTS WITHNEOWISE: PRELIMINARY RESULTS, *The Astrophysical Journal*, *752*(2), 110, doi:10.1088/0004-637x/752/2/110.

Malhotra, R. (1993), The origin of Pluto's peculiar orbit, *Nature*, *365*(6449), 819–821, doi:10.1038/365819a0.

Malhotra, R. (1995), The Origin of Pluto's Orbit: Implications for the Solar System Beyond Neptune, *AJ*, *110*, 420, doi:10.1086/117532.

Malhotra, R. (2019), The case for a deep search for Earth's Trojan asteroids, *Nature Astronomy*, *3*, 193–194, doi:10.1038/s41550-019-0697-z.

Malhotra, R. (2019), The case for a deep search for Earth's Trojan asteroids, *Nature Astronomy*, *3*(3), 193–194, doi:10.1038/s41550-019-0697-z.

Malhotra, R., and Y. Jeongahn (2011), Dynamical investigations on the leading/trailing asymmetry of lunar rayed craters, *EPSC-DPS Joint Meeting 2011*, p. 1215.

Markwardt, L., D. W. Gerdes, R. Malhotra, J. C. Becker, S. J. Hamilton, and F. C. Adams (2020), Search for L5 Earth Trojans with DECam, *MNRAS*, *492*(4), 6105–6119, doi:10.1093/mnras/staa232.

Markwardt, L., F. Adams, D. Gerdes, H. W. Lin, R. Malhotra, and K. Napier (2021), The First Near-IR Spectroscopic Survey of Neptune Trojans, JWST Proposal. Cycle 1, ID. #2550.

Markwardt, L., H. W. Lin, D. Gerdes, and F. C. Adams (submitted), Photometric survey of neptune's trojan asteroids i: The color distribution.

Marsset, M., P. Vernazza, F. Gourgeot, C. Dumas, M. Birlan, P. Lamy, and R. P. Binzel (2014), Similar origin for low- and high-albedo Jovian Trojans and Hilda asteroids?, *A&A*, *568*, L7, doi:10.1051/0004-6361/201424105.

Marzari, F., and H. Scholl (2013), Long term stability of Earth Trojans, *Celestial Mechanics and Dynamical Astronomy*, *117*(1), 91–100, doi:10.1007/s10569-013-9478-7.

Merlin, F., T. Hromakina, D. Perna, M. J. Hong, and A. Alvarez-Candal (2017), Taxonomy of trans-Neptunian objects and Centaurs as seen from spectroscopy, *A&A*, *604*, A86, doi:10.1051/0004-6361/201730933.

Michel, P., and D. C. Richardson (2013), Collision and gravitational reaccumulation: Possible formation mechanism of the asteroid Itokawa, *A&A*, *554*, L1, doi:10.1051/0004-6361/201321657.

Mikkola, S., R. Brasser, P. Wiegert, and K. Innanen (2004), Asteroid 2002 VE68, a quasi-satellite of Venus, *MNRAS*, *351*(3), L63–L65, doi:10.1111/j.1365-2966.2004.07994.x.

Moffat, A. F. J. (1969), A Theoretical Investigation of Focal Stellar Images in the Photographic Emulsion and Application to Photographic Photometry, *A&A*, *3*, 455.

Morais, M., and A. Morbidelli (2002), The population of near-earth asteroids in coorbital motion with the earth, *Icarus*, *160*(1), 1 – 9, doi: https://doi.org/10.1006/icar.2002.6937.

Morbidelli, A., H. F. Levison, K. Tsiganis, and R. Gomes (2005), Chaotic capture of Jupiter's Trojan asteroids in the early Solar System, *Nature*, *435*, 462.

Morota, T., and M. Furumoto (2003), Asymmetrical distribution of rayed craters on the moon, *Earth and Planetary Science Letters*, *206*(3), 315 – 323, doi: https://doi.org/10.1016/S0012-821X(02)01111-1.

Mottola, S., S. Hellmich, M. W. Buie, A. M. Zangari, S. Marchi, M. E. Brown, and H. F. Levison (2020), Convex Shape and Rotation Model of Lucy Target (11351) Leucus from Lightcurves and Occultations, , *1*(3), 73, doi:10.3847/PSJ/abb942.

Müller, T. G., et al. (2018), Small Bodies Near and Far (SBNAF): A benchmark study on physical and thermal properties of small bodies in the Solar System, *Advances in Space Research*, *62*(8), 2326–2341, doi:10.1016/j.asr.2017.10.018.

Nakamura, T., et al. (2011), Itokawa Dust Particles: A Direct Link Between S-Type Asteroids and Ordinary Chondrites, *Science*, *333*(6046), 1113, doi: 10.1126/science.1207758.

Napier, K. J., L. Markwardt, F. C. Adams, D. W. Gerdes, and H. Wen Lin (2022), A Collision Mechanism for the Removal of Earth's Trojan Asteroids, *PSJ*, *3*(5), 121, doi:10.3847/PSJ/ac6958.

Navarro-Meza, S., E. Aadland, and D. Trilling (2021), Asteroid lightcurves and detection, shape, and size biases in large-scale surveys, *Research Notes of the AAS*, *5*(5), 111, doi:10.3847/2515-5172/ac0059.

Nesvorný, D. (2011), Young Solar System's Fifth Giant Planet?, *ApJ*, *742*(2), L22, doi:10.1088/2041-8205/742/2/L22.

Nesvorný, D., and A. Morbidelli (2012), Statistical Study of the Early Solar System's Instability with Four, Five, and Six Giant Planets, *AJ*, *144*(4), 117, doi:10.1088/0004-6256/144/4/117.

Nesvorný, D., and D. Vokrouhlický (2009), Chaotic Capture of Neptune Trojans, *AJ*, *137*(6), 5003–5011, doi:10.1088/0004-6256/137/6/5003.

Nesvorný, D., D. Vokrouhlický, and A. Morbidelli (2013), Capture of Trojans by Jumping Jupiter, *ApJ*, *768*(1), 45, doi:10.1088/0004-637X/768/1/45.

Nesvorný, D., D. Vokrouhlický, W. F. Bottke, and H. F. Levison (2018), Evidence for very early migration of the Solar System planets from the Patroclus-Menoetius binary Jupiter Trojan, *Nature Astronomy*, *2*, 878–882, doi:10.1038/s41550-018-0564-3.

Nesvorný, D., et al. (2020), OSSOS XX: The Meaning of Kuiper Belt Colors, *AJ*, *160*(1), 46, doi:10.3847/1538-3881/ab98fb.

Neveu, M., and P. Vernazza (2019), IDP-like Asteroids Formed Later than 5 Myr After Ca-Al-rich Inclusions, *ApJ*, *875*(1), 30, doi:10.3847/1538-4357/ab0d87.

Nicholson, S. B. (1961), The Trojan Asteroids, *Leaflet of the Astronomical Society of the Pacific*, *8*(381), 239.

Olkin, C. B., et al. (2021), Lucy Mission to the Trojan Asteroids: Instrumentation and Encounter Concept of Operations, , *2*(5), 172, doi:10.3847/PSJ/abf83f.

Ostro, S. J., and R. Connelly (1986), Shapes of Asteroids from Radar, in *Lunar and Planetary Science Conference*, Lunar and Planetary Science Conference, pp. 634–635.

Pan, J., et al. (2022), Photometric Properties of Jupiter Trojans Detected by the Dark Energy Survey, , *3*(12), 269, doi:10.3847/PSJ/aca4d1.

Parker, A., et al. (2016), Physical Characterization of TNOs with JWST, *Publ. Astron. Soc. Pacific*, *128*(959), 18,010, doi:10.1088/1538-3873/128/959/018010.

Parker, A. H. (2015), The intrinsic Neptune Trojan orbit distribution: Implications for the primordial disk and planet migration, , *247*, 112–125, doi:10.1016/j.icarus.2014.09.043.

Parker, A. H. (2017), TNOs, JWST Proposal. Cycle 1, ID. #1254.

Parker, A. H., et al. (2013), 2011 HM_{102}: Discovery of a High-inclination L5 Neptune Trojan in the Search for a Post-Pluto New Horizons Target, *AJ*, *145*(4), 96, doi:10.1088/0004-6256/145/4/96.

Pedregosa, F., et al. (2011), Scikit-learn: Machine learning in Python, *Journal of Machine Learning Research*, *12*, 2825–2830.

Peixinho, N., A. Delsanti, A. Guilbert-Lepoutre, R. Gafeira, and P. Lacerda (2012), The bimodal colors of Centaurs and small Kuiper belt objects, *A&A*, *546*, A86, doi:10.1051/0004-6361/201219057.

Peixinho, N., A. Delsanti, and A. Doressoundiram (2015), Reanalyzing the visible colors of Centaurs and KBOs: what is there and what we might be missing, *A&A*, *577*, A35, doi:10.1051/0004-6361/201425436.

Pike, R. E., S. Lawler, R. Brasser, C. J. Shankman, M. Alexandersen, and J. J. Kavelaars (2017a), The Structure of the Distant Kuiper Belt in a Nice Model Scenario, *AJ*, *153*(3), 127, doi:10.3847/1538-3881/aa5be9.

Pike, R. E., et al. (2017b), Col-OSSOS: z-Band Photometry Reveals Three Distinct TNO Surface Types, *AJ*, *154*(3), 101, doi:10.3847/1538-3881/aa83b1.

Pike, R. E., et al. (2020), A dearth of small members in the Haumea family revealed by OSSOS, *Nature Astronomy*, *4*, 89–96, doi:10.1038/s41550-019-0867-z.

Pinilla-Alonso, N., et al. (2021), DiSCo-TNOs: Discovering the composition of the trans-Neptunian objects, icy embryos for planet formation, JWST Proposal. Cycle 1, ID. #2418.

Polishook, D., S. A. Jacobson, A. Morbidelli, and O. Aharonson (2017), A Martian origin for the Mars Trojan asteroids, *Nature Astronomy*, *1*, 0179, doi:10.1038/s41550-017-0179.

Ragozzine, D., and M. E. Brown (2009), Orbits and Masses of the Satellites of the Dwarf Planet Haumea (2003 EL61), *AJ*, *137*(6), 4766–4776, doi:10.1088/0004-6256/137/6/4766.

Rein, H., and S.-F. Liu (2011), REBOUND: An open-source multi-purpose N-body code for collisional dynamics, *Astronomy & Astrophysics*, *537*, A128, doi:10.1051/0004-6361/201118085.

Rice, M., and G. Laughlin (2020), Exploring Trans-Neptunian Space with TESS: A Targeted Shift-stacking Search for Planet Nine and Distant TNOs in the Galactic Plane, , *1*(3), 81, doi:10.3847/PSJ/abc42c.

Rivkin, A. S., R. P. Binzel, E. S. Howell, S. J. Bus, and J. A. Grier (2003), Spectroscopy and photometry of Mars Trojans, , *165*(2), 349–354, doi:10.1016/S0019-1035(03)00211-2.

Rivkin, A. S., D. E. Trilling, C. A. Thomas, F. DeMeo, T. B. Spahr, and R. P. Binzel (2007), Composition of the L5 Mars Trojans: Neighbors, not siblings, , *192*(2), 434–441, doi:10.1016/j.icarus.2007.06.026.

Rivkin, A. S., S. N. Milam, and C. A. Thomas (2017), Large Asteroids and Trojan Asteroids, JWST Proposal. Cycle 1, ID. #1244.

Roig, F., and D. Nesvorný (2015), The Evolution of Asteroids in the Jumping-Jupiter Migration Model, *AJ*, *150*(6), 186, doi:10.1088/0004-6256/150/6/186.

Roig, F., A. O. Ribeiro, and R. Gil-Hutton (2008), Taxonomy of asteroid families among the Jupiter Trojans: comparison between spectroscopic data and the Sloan Digital Sky Survey colors, *A&A*, *483*(3), 911–931, doi:10.1051/0004-6361:20079177.

Roig, F., D. Nesvorný, and S. R. DeSouza (2016), Jumping Jupiter Can Explain Mercury's Orbit, *ApJ*, *820*(2), L30, doi:10.3847/2041-8205/820/2/L30.

Ross, S., W. Koon, M. Lo, and J. Marsden (2011), *Dynamical Systems, the Three-Body Problem, and Space Mission Design*.

Sagan, C., and B. N. Khare (1979), Tholins: organic chemistry of interstellar grains and gas, *Nature*, *277*(5692), 102–107, doi:10.1038/277102a0.

Sanchez, J. A., et al. (2014), Olivine-dominated asteroids: Mineralogy and origin, , *228*, 288–300, doi:10.1016/j.icarus.2013.10.006.

Schindler, K., and W. M. Grundy (2018), *Pluto and Lowell Observatory: a history of discovery at Flagstaff*.

Schindler, K., et al. (2017), Results from a triple chord stellar occultation and far-infrared photometry of the trans-Neptunian object (229762) 2007 UK_{126}, *A&A*, *600*, A12, doi:10.1051/0004-6361/201628620.

Schwamb, M. E., et al. (2019), Col-OSSOS: The Colors of the Outer Solar System Origins Survey, *ApJS*, *243*(1), 12, doi:10.3847/1538-4365/ab2194.

Schwartz, S. R., P. Michel, M. Jutzi, S. Marchi, Y. Zhang, and D. C. Richardson (2018), Catastrophic disruptions as the origin of bilobate comets, *Nature Astronomy*, *2*, 379–382, doi:10.1038/s41550-018-0395-2.

Schwarz, G. J., et al. (2011), Swift X-Ray Observations of Classical Novae. II. The Super Soft Source Sample, *ApJS*, *197*(2), 31, doi:10.1088/0067-0049/197/2/31.

Seargent, D. (2008), *The Greatest Comets in History: Broom Stars and Celestial Scimitars*, Astronomers' Universe, Springer New York.

Seccull, T., W. C. Fraser, and T. H. Puzia (2021), The Reflectance of Cold Classical Trans-Neptunian Objects in the Nearest Infrared, , *2*(2), 57, doi:10.3847/PSJ/abe4d9.

Shankman, C., B. J. Gladman, N. Kaib, J. J. Kavelaars, and J. M. Petit (2013), A Possible Divot in the Size Distribution of the Kuiper Belt's Scattering Objects, *ApJ*, *764*(1), L2, doi:10.1088/2041-8205/764/1/L2.

Shepard, M. K., et al. (2017), Radar observations and shape model of asteroid 16 psyche, *Icarus*, *281*, 388–403, doi:https://doi.org/10.1016/j.icarus.2016.08.011.

Sheppard, S. S. (2010), The Colors of Extreme Outer Solar System Objects, *AJ*, *139*(4), 1394–1405, doi:10.1088/0004-6256/139/4/1394.

Sheppard, S. S. (2012), The Color Differences of Kuiper Belt Objects in Resonance with Neptune, *AJ*, *144*(6), 169, doi:10.1088/0004-6256/144/6/169.

Sheppard, S. S., and C. A. Trujillo (2006), A Thick Cloud of Neptune Trojans and Their Colors, *Science*, *313*(5786), 511–514, doi:10.1126/science.1127173.

Shoemaker, E. M., C. S. Shoemaker, and R. F. Wolfe (1989), Trojan asteroids: populations, dynamical structure and origin of the L4 and L5 swarms., in *Asteroids II*, edited by R. P. Binzel, T. Gehrels, and M. S. Matthews, pp. 487–523.

Simpson, A. M., M. E. Brown, M. J. Schemel, and B. J. Butler (2022), An ALMA Search for High-albedo Objects Among the Midsized Jupiter Trojan Population, *AJ*, *164*(1), 23, doi:10.3847/1538-3881/ac559e.

Stansberry, J. A., B. J. Holler, N. Pinilla-Alonso, and M. J. Rieke (2017), Kuiper Belt Science with JWST, JWST Proposal. Cycle 1, ID. #1191.

Strauss, R. H., et al. (2021), The Sizes and Albedos of Centaurs 2014 YY_{49} and 2013 NL_{24} from Stellar Occultation Measurements by RECON, , *2*(1), 22, doi:10.3847/PSJ/abd62a.

Sugiura, K., H. Kobayashi, and S. Inutsuka (2018), Toward understanding the origin of asteroid geometries. Variety in shapes produced by equal-mass impacts, *A&A*, *620*, A167, doi:10.1051/0004-6361/201833227.

Szabó, G. M., Ž. Ivezić, M. Jurić, and R. Lupton (2007), The properties of Jovian Trojan asteroids listed in SDSS Moving Object Catalogue 3, *MNRAS*, *377*(4), 1393–1406, doi:10.1111/j.1365-2966.2007.11687.x.

Tabachnik, S. A., and N. W. Evans (2003), Asteroids in the inner Solar system - I. Existence, *Monthly Notices of the Royal Astronomical Society*, *319*(1), 63–79, doi:10.1046/j.1365-8711.2000.03760.x.

Tabeshian, M., P. Wiegert, Q. Ye, M.-T. Hui, X. Gao, and H. Tan (2019), Asteroid (3200) phaethon: Colors, phase curve, limits on cometary activity, and fragmentation, *The Astronomical Journal*, *158*(1), 30, doi:10.3847/1538-3881/ab245d.

Thirouin, A., and S. S. Sheppard (2019), Light Curves and Rotational Properties of the Pristine Cold Classical Kuiper Belt Objects, *AJ*, *157*(6), 228, doi:10.3847/1538-3881/ab18a9.

Thirouin, A., S. S. Sheppard, K. S. Noll, N. A. Moskovitz, J. L. Ortiz, and A. Doressoundiram (2016), Rotational Properties of the Haumea Family Members and Candidates: Short-term Variability., *AJ*, *151*(6), 148, doi:10.3847/0004-6256/151/6/148.

Tholen, D. J. (1984), Asteroid Taxonomy from Cluster Analysis of Photometry., Ph.D. thesis, University of Arizona.

Thomas, C. A., and A. S. Rivkin (2017), Near-Earth Objects, JWST Proposal. Cycle 1, ID. #1245.

Tonry, J. L., et al. (2012), The Pan-STARRS1 Photometric System, *ApJ*, *750*(2), 99, doi:10.1088/0004-637X/750/2/99.

Trilling, D. E., A. S. Rivkin, J. A. Stansberry, T. B. Spahr, R. A. Crudo, and J. K. Davies (2007), Albedos and diameters of three Mars Trojan asteroids, , *192*(2), 442–447, doi:10.1016/j.icarus.2007.08.002.

Trilling, D. E., B. J. Holler, M. M. Mueller, A. S. Rivkin, J. A. Stansberry, and C. A. Thomas (2021), A pure parallel survey of water in the asteroid belt, JWST Proposal. Cycle 1, ID. #2211.

Tsiganis, K., R. Gomes, A. Morbidelli, and H. F. Levison (2005), Origin of the orbital architecture of the giant planets of the Solar System, *Nature*, *435*(7041), 459–461, doi:10.1038/nature03539.

Tsirvoulis, G., A. Morbidelli, M. Delbo, and K. Tsiganis (2018), Reconstructing the size distribution of the primordial main belt, *Icarus*, *304*, 14 – 23, doi: https://doi.org/10.1016/j.icarus.2017.05.026, asteroids and Space Debris.

Valdes, F., R. Gruendl, and DES Project (2014), The DECam Community Pipeline, *ASP Conference Series*, *485*(Astronomical Data Analysis Software and Systems XXIII), 379–382.

Ďurech, J., et al. (2018), Shape models of asteroids based on lightcurve observations with BlueEye600 robotic observatory, , *304*, 101–109, doi:10.1016/j.icarus.2017.07.005.

Vernazza, P., and P. Beck (2016), Composition of Solar System Small Bodies, *arXiv e-prints*, arXiv:1611.08731.

Volk, K., et al. (2018), Ossos. ix. two objects in neptune's 9:1 resonance—implications for resonance sticking in the scattering population, *The Astronomical Journal*, *155*(6), 260, doi:10.3847/1538-3881/aac268.

Whidden, P. J., et al. (2019), Fast Algorithms for Slow Moving Asteroids: Constraints on the Distribution of Kuiper Belt Objects, *AJ*, *157*(3), 119, doi:10.3847/1538-3881/aafd2d.

Whiteley, R. J., and D. J. Tholen (1998), A CCD Search for Lagrangian Asteroids of the Earth-Sun System, *Icarus*, *136*(1), 154–167, doi:10.1006/icar.1998.5995.

Wiegert, P. A., K. A. Innanen, and S. Mikkola (1998), The Orbital Evolution of Near-Earth Asteroid 3753, *AJ*, *115*(6), 2604–2613, doi:10.1086/300358.

Wong, I., and M. E. Brown (2015), The Color-Magnitude Distribution of Small Jupiter Trojans, *AJ*, *150*(6), 174, doi:10.1088/0004-6256/150/6/174.

Wong, I., and M. E. Brown (2016), A Hypothesis for the Color Bimodality of Jupiter Trojans, *AJ*, *152*(4), 90, doi:10.3847/0004-6256/152/4/90.

Wong, I., and M. E. Brown (2017a), The Color-Magnitude Distribution of Hilda Asteroids: Comparison with Jupiter Trojans, *AJ*, *153*(2), 69, doi:10.3847/1538-3881/153/2/69.

Wong, I., and M. E. Brown (2017b), The Bimodal Color Distribution of Small Kuiper Belt Objects, *AJ*, *153*(4), 145, doi:10.3847/1538-3881/aa60c3.

Wong, I., M. E. Brown, and J. P. Emery (2014), The Differing Magnitude Distributions of the Two Jupiter Trojan Color Populations, *AJ*, *148*(6), 112, doi:10.1088/0004-6256/148/6/112.

Xu, Y.-B., L.-Y. Zhou, and W.-H. Ip (2020a), Transit of asteroids across the 7/3 Kirkwood gap under the Yarkovsky effect, *A&A*, *637*, A19, doi:10.1051/0004-6361/201937261.

Xu, Y.-B., L.-Y. Zhou, C. Lhotka, and W.-H. Ip (2020b), Asteroid migration due to the Yarkovsky effect and the distribution of the Eos family, *MNRAS*, *493*(1), 1447–1460, doi:10.1093/mnras/staa352.

Yada, T., et al. (2021), Preliminary analysis of the Hayabusa2 samples returned from C-type asteroid Ryugu, *Nature Astronomy*, *6*, 214–220, doi:10.1038/s41550-021-01550-6.

Yeager, T., and N. Golovich (2022), MEGASIM: Lifetimes and Resonances of Earth Trojan Asteroids-The Death of Primordial ETAs?, *ApJ*, *938*(1), 9, doi:10.3847/1538-4357/ac8e63.

Yoshida, F., and T. Terai (2017), Small jupiter trojans survey with the subaru/hyper suprime-cam, *The Astronomical Journal*, *154*(2), 71, doi:10.3847/1538-3881/aa7d03.

Yoshikawa, M., Y. Tsuda, S. Watanabe, S. Tanaka, S. Nakazawa, F. Terui, and T. Saiki (2018), MISSION STATUS OF HAYABUSA2, in *49th Lunar and Planetary Science Conference*, p. No. 1771.

Zhou, L., Y.-B. Xu, L.-Y. Zhou, R. Dvorak, and Jian (2018), Orbital Stability of Earth Trojans, doi:10.1051/0004-6361/201834026.